The geologic setting, kinematics and deformation mechanisms of the Eagle River gold deposit, Northern Ontario

Ryan J. Barkley

Thesis submitted in partial fulfillment of the requirements for the degree of

Master of Science in Geology

Lakehead University

Abstract

The Neoarchean Eagle River orogenic gold deposit in the Mishibishu greenstone belt of northern Ontario, Canada, was investigated through a multidisciplinary approach integrating field mapping, lithogeochemistry, isotope analysis, EBSD mapping, CVA analysis and geothermometry techniques. Near mine host rocks comprise two distinct suites: tholeiitic and calc-alkaline volcanic rocks. When normalized to primitive mantle values, the tholeiitic basalts and gabbros have negative Nb and Ti anomalies, near flat LREE (La/Sm_{pm} = 0.94-1.25) to weakly fractionated HREE patterns (Gd/Yb_{pm} = 0.88-1.62) and $\varepsilon Nd_{T(2700)}$ values of +1.93 to +2.50, indicating little crustal contamination and formation within a primitive intra-oceanic plateau setting analogous to the Phanerozoic Ontong Java plateaus. The second suite (calc-alkaline) comprises intermediate and felsic samples, including diorites, andesites, granodiorites, and granites. The intermediate samples exhibit negative Nb and Ti anomalies, with moderate LREE patterns (La/Sm_{pm} = 1.29-5.82) and HREE fractionation (Gd/Yb_{pm} = 0.70-4.28). The felsic samples have moderate LREE enrichment (La/Sm_{pm} = 1.29-5.82), HREE fractionation (Gd/Yb_{pm} = 0.70-4.28), and $\varepsilon Nd_{(2700\ Ma)}$ values of +1.53 to +2.56, suggesting evolution in a closed system through subduction-driven fractional crystallization, similar to the modern-day western Canadian Cordillera orogeny.

The Eagle River deformation zone is a ~4 km-long, curvilinear, along-strike brittle–ductile shear zone characterized by oblique dip-slip deformation. It records two dominant kinematic regimes: a pure shear–dominated component associated with oblique crustal shortening, and a simple shear component reflecting dextral reverse transpression. Sheared quartz veins have been fully recrystallized and exhibit non-coaxial deformation with triclinic flow geometry. Gold mineralization preferentially occurs at vein selvages where fractured

plagioclase networks provide a brittle contrast with dynamically recrystallized quartz veins and veinlets. Sheared quartz grains show evidence of grain boundary migration within the dislocation creep regime, with gold grains, sulphides, and other impurities concentrating at the quartz vein selvage. These findings support a tectonic model in which subduction-related, calc-alkaline rocks were emplaced on primitive oceanic plateau crust in an intra-oceanic island arc environment and underwent ductile deformation, with gold concentration facilitated by crystal plastic deformation, creating favorable structural traps and fluid pathway arrays. This research enhances our understanding of the formation and tectonic framework of this high-grade gold deposit, providing insights into exploration prospectivity within similar geological settings.

Acknowledgments

I want to thank Dr. Pete Hollings for providing this opportunity and for his patience throughout the project, as well as Dr. Noah Phillips for his invaluable guidance on the kinematics and deformation sections. I would also like to express my gratitude to Mike Michaud (now President, RPX Gold), Nathan Forslund, and Wesdome Gold's exploration department for their support and funding of this excellent opportunity to advance our understanding of orogenic gold deposits in Canada's Superior Craton.

Additionally, I would like to thank Dr. Howard Poulsen (Canada) and Dr. Brett Davis (Australia) for teaching exceptional short courses in gold exploration and structural geology during my time at Lakehead. Both courses were directly relevant to my research and provided such practical, hands-on knowledge that they ignited a genuine enthusiasm for field exploration and science-driven gold discovery.

Table of Contents

Table of Figures

Chapter 2: Geological Setting

Chapter 4: Results

Chapter 5: Discussion

List of Tables

Chapter 1: Introduction

The Neoarchean Superior Craton preserves one of the world's most important records of early crustal evolution, deformation, magmatism, and mineralization. Within the craton, granite-greenstone belts are especially significant because they contain abundant evidence of Archean tectonic processes and host many economically important orogenic gold deposits. These belts, therefore, provide an important framework for examining the relationships between crustal growth, deformation, hydrothermal activity, and precious metal endowment. In the southern Superior Province, east-west-trending granite-greenstone terranes and associated sedimentary basins record a long and complex history of magmatism, deformation, metamorphism, and terrane amalgamation that created favorable conditions for widespread gold mineralization (Card, 1990).

The Mishibishu greenstone belt, located within the Wawa-Abitibi terrane of the Superior Craton, is one such Archean belt in which these processes can be examined at the deposit scale. It hosts the Eagle River gold deposit, an orogenic gold system currently mined by Wesdome Gold. Eagle River occurs within a regionally significant gold camp that also includes major deposits elsewhere in the broader Wawa and Hemlo areas, highlighting the exceptional metallogenic fertility of this part of the southern Superior Craton (Wawrzonkowski, 2024). Like many orogenic gold deposits in Archean granite-greenstone belts, Eagle River is spatially associated with high-strain zones, intrusive rocks, and structurally focused quartz-vein systems (Goldfarb et al., 1998). However, although orogenic gold systems across the Superior Province share broad first-order similarities, individual deposits vary considerably in host rock lithology, rheology, structural architecture, alteration style, and the timing and mechanisms of

mineralization (Groves et al., 2018). These local differences are critical because they govern how strain is partitioned, how fluids are focused, and ultimately where mineralization is deposited.

At Eagle River, mineralization is associated with the Eagle River deformation zone, a network of curved, east-west-striking, steeply dipping shear zones developed within a dioritic intrusion and adjacent volcanic rocks (Wawrzonkowski, 2024). Such relationships raise broader questions about the tectonic and structural evolution of the deposit and about the extent to which magmatism, deformation, and fluid circulation were genetically linked during ore formation.

Despite the economic and geological significance of Eagle River, several important aspects of its evolution remain insufficiently resolved. In particular, the relative timing of host-rock pluton emplacement, shear zone development, veining, gold mineralization, and later fault reactivation is not fully constrained. It also remains unclear how the geochemical character of the near-mine intrusions relates to their tectono-magmatic setting and whether these intrusions were simply passive hosts to deformation and mineralization or played a more active role in strain localization and fluid focusing. More broadly, the pressure-temperature conditions, deformation mechanisms, and kinematic evolution of the shear zones associated with mineralization require better definition in order to understand how the structural framework of the deposit evolved through time. These uncertainties limit our ability to place Eagle River within the wider tectonic evolution of the Mishibishu greenstone belt and to evaluate the processes that controlled the formation of the ore system.

This thesis addresses these gaps by testing the idea that the Eagle River deposit formed through a progressive interaction among magmatism, deformation, and hydrothermal fluid flow during multiple tectonic events. The central premise of this study is that the emplacement and

rheological properties of near-mine plutonic bodies influenced the localization of high-strain zones, which in turn focused fluid flow and promoted quartz-vein development and gold deposition.

To investigate these questions, this study integrated field-based, petrographic, geochemical, and microstructural methods. Detailed structural mapping conducted during the 2022 and 2023 field seasons was used to characterize the geometry, orientation, and relative timing of major shear zones, faults, and veins across the mine area. Re-logging of exploration drill core provided additional three-dimensional control on lithological contacts, alteration patterns, vein relationships, and structural overprints at depth. Whole-rock trace element geochemistry and isotope analyses were used to constrain the Eagle River Mine host rocks. Oriented thin sections and SEM-supported petrography were used to examine mineral assemblages, microstructures, and fluid-related alteration textures, while EBSD mapping and crystallographic vorticity axis analysis of gold-bearing sheared quartz veins in near-mine shear zones 8 and 2 were applied to constrain deformation mechanisms, kinematics, and strain conditions during vein development. In addition, XRD analysis of fault gouge was used to assess the mineralogical character of late brittle faulting and to better define the nature of post-mineralization deformation.

The overall objective of this thesis was to reconstruct the tectonic evolution of the Eagle River mine area and determine how that evolution contributed to the formation of the Eagle River Au deposit. Specifically, the study aimed to constrain the timing and geochemical character of near-mine plutons, define the structural architecture and kinematic history of the principal shear zones, characterize the deformation mechanisms recorded in gold-bearing quartz veins, and evaluate the significance of later faulting events in overprinting the deposit.

Chapter 2: Geological Setting

2.1 Superior Province

The Superior Province is the world's largest and most well-preserved Archean craton. It is located primarily in Canada, spanning Manitoba, Ontario, and Quebec. It extends into the northern regions of Minnesota and Michigan in the USA (Fig. 2.1). The Superior craton is the core of the North American continent, home to almost 25% of all exposed Archean crust in the world (along with some of the oldest dated rocks on Earth) and covers an area of 1,572 000 km² (Goodwin, 1991; Fig. 2.1).

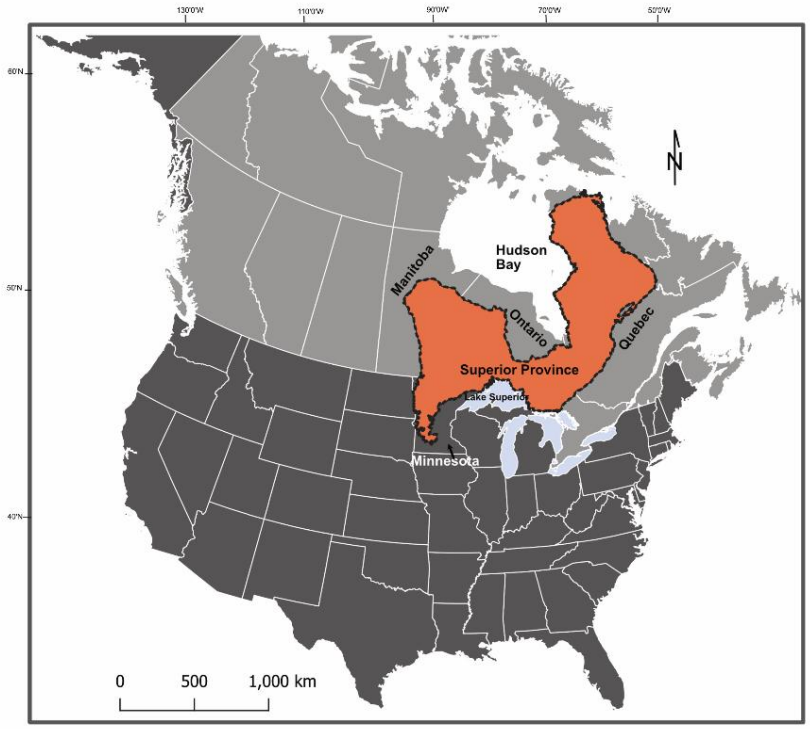

Fig. 2.1: A simplified map of North America with the location and extent of the Superior Province indicated in orange (modified from Montsion et al., 2018).

The Superior Province comprises belt-like subprovinces, divided on the basis of contrasts in lithology, structure, metamorphic grade, and geophysical signatures. Approximately 35

greenstone belts and 127 tectonic assemblages occur in the Superior craton (Stott et al., 2010; Card & Ciesielski, 1986). Subprovinces are subdivided into four types. The first is the volcano-plutonic subprovinces, consisting of long linear regions dominated by volcanic-rich supracrustal rocks known as greenstone belts. They are generally deposited on the sialic crust and/or oceanic to transitional crust dominated by ancient island arc-like sequences formed in multiple tectonic environments (Card, 1990; Stott & Corfu, 1991). Supracrustal belts in the Superior Province have been shown to have undergone early, sub-horizontal translation and thin-skinned shortening, followed by upright folding (Percival et al., 2006). The second type, metasedimentary subprovinces, comprises long, linear regions of mostly greywacke and their magmatic derivatives, including migmatite and peraluminous granite batholiths (Stott et al., 2010). The third type, plutonic subprovinces, is formed through partial melting of the mantle and lower crustal rocks. The fourth and final subdivision, high-grade gneissic subprovinces, is characterized by the presence of high-grade metamorphic rocks that have undergone extensive recrystallization processes, such as the Winnipeg River subprovince, an older, more felsic-dominated crustal block (Percival & McGrath, 1986; Fig. 2.2).

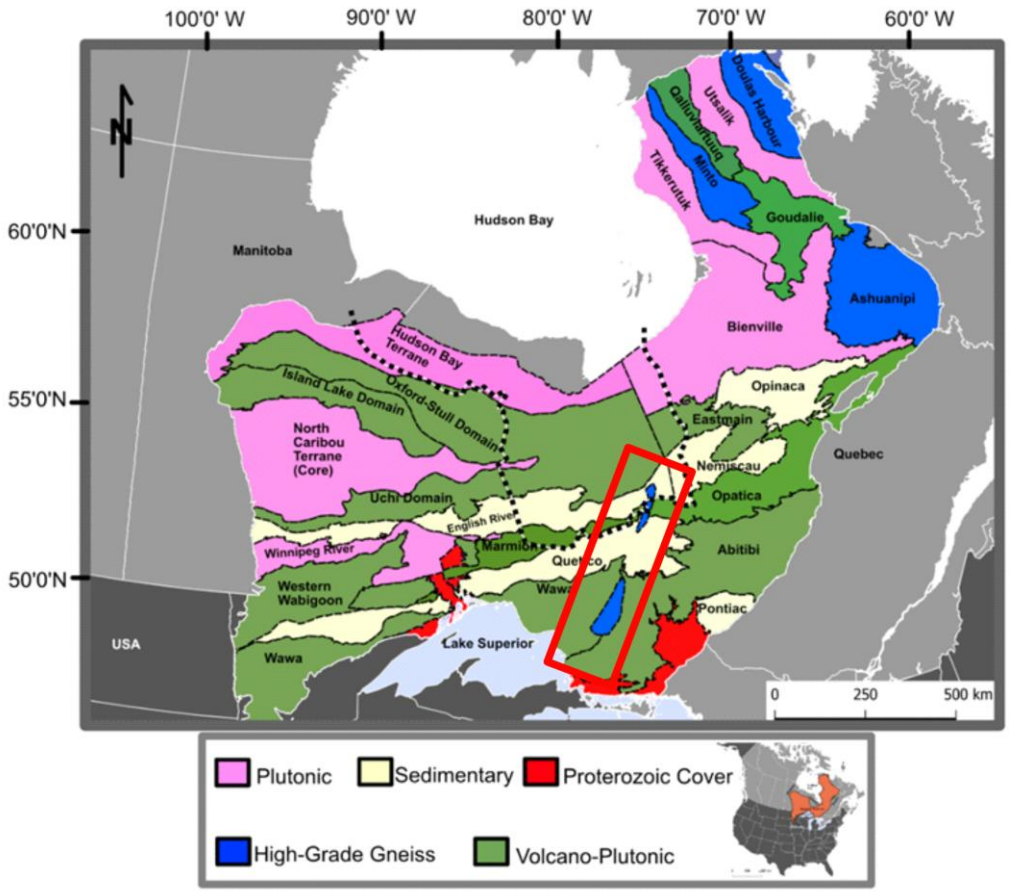

Fig. 2.2: Map of the Superior Craton with its subdivisions and the Kapuskasing structural zone indicated in blue and outlined in a red rectangle, separating the Wawa and Abitibi subprovinces (modified shape files from Metal Earth, 2018).

The Superior Province was formed by volcanic and intrusive events from 3.25 Ga to 2.6 Ga (Card, 1990; Percival et al., 2006). Five discrete accretionary events of individual oceanic and continental crust segments have been recognized between 2.60 and 3.25 Ga. Each exhibits a similar series of events at approximately ten million-year intervals: cessation of arc magmatism, early deformation, synorogenic sedimentation, sanukitoid magmatism, regional metamorphism, bulk shortening, late transpressional kinematics, various orogenic gold mineralization events, emplacement of granitoid plutons and post-orogenic cooling (Percival et al., 2006; Goldfarb et al., 2005).

The nucleus of the Superior Craton is interpreted to be the North Caribou terrane (NCT), resulting in the subsequent convergence of individual superterranes of the central belts towards the continental margin along the southern flank of the Uchi-Sachigo-Goudalie (USG) superterrane (Percival et al., 2006a). Compelling evidence for this successive convergence includes mid-crustal, accretional, southward verging reflectors and imbricate thrust stacking, evident in the reflection seismic transects across the Opatica-Abitibi-Pontiac subprovinces (Ludden et al., 1993). Further evidence is apparent with the formation of sedimentary-basin deposits, most common off the southern margins of the USG and Wabigoon superterranes. The location and composition of these sedimentary deposits underlie oceanic crust and form linear, thickened metasedimentary wedges, the byproduct of successive collisions of the volcanic-plutonic superterranes (Card, 1990). These successions are interpreted as progressing from an earlier 2.71 Ga Uchian collisional phase along the southern USG boundary to a later 2.69 Ga Shebandowan phase across the Wawa-Quetico boundary (Percival et al., 2006). This convergence was oblique to the superterrane boundaries, resulting in crustal thickening of each superterrane (Stott et al., 2010).

The Wawa subprovince comprises later successions of juxtaposed Mesoarchean and Neoarchean domains, characterized by distinct geochemical and structural features within the amalgamated Superior craton. It is in the southern region of Ontario and extends to Minnesota in the south. (Stott et al., 2010; Fig. 2.3).

2.2 Wawa Subprovince

The granite-greenstone Wawa subprovince extends from the Vermillion district of Minnesota in the west to the Kapuskasing structural zone (KSZ) to the east (Williams et al., 1991; Fig. 2.2). The northeast-trending Kapuskasing zone intersects the east-west belts of the central Superior cross cutting over a distance of 500 km (Percival & McGrath, 1986). The KSZ is interpreted by Percival and Card (1985) to be an oblique crustal cross-section through an Archean Greenstone belt. All segments of the KSZ event can be related to an early compressional uplift stage and a later tensional event, possibly resulting from decreased lithospheric strength (Percival & McGrath, 1986).

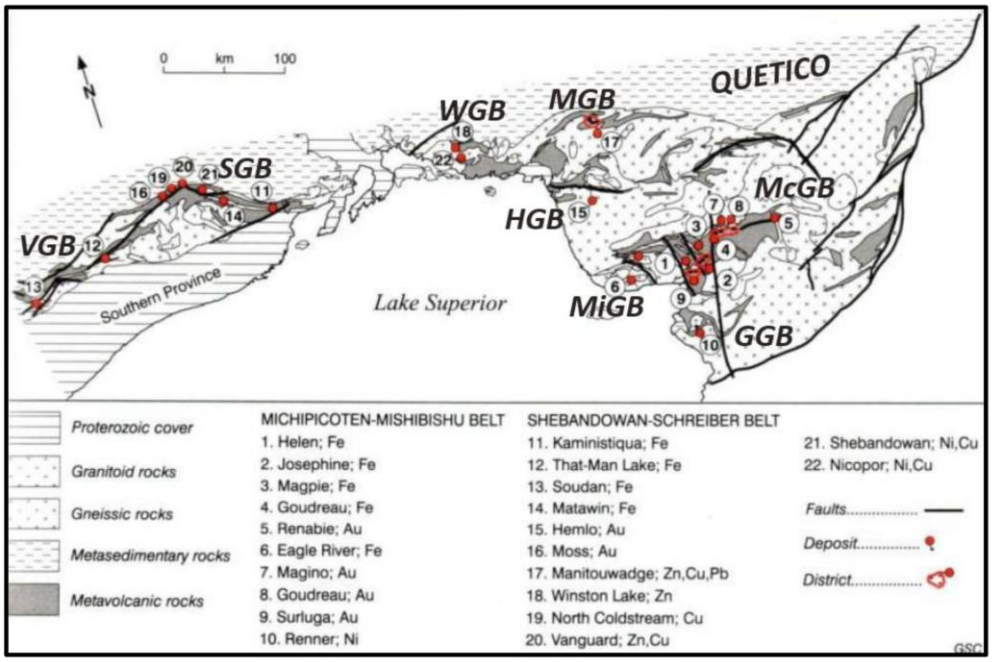

Fig. 2.3: Location of various greenstone belts and mines within the Wawa terrane. MGB – Manitouwadge greenstone belt; SGB – Shebandowan greenstone belt; VGB – Vermillion greenstone belt; WGB Winston Lake greenstone belt; McGB – Michipicoten Greenstone belt; MiGB – Mishibishu Lake greenstone belt; HGB – Hemlo greenstone belt; GGB – Gamitagamma greenstone belt. Modified from Card and Poulsen (1998).

The northern boundary of the Wawa subprovince is a tectonic contact hosted in metasedimentary rocks related to the Quetico Subprovince (Fig. 2.3). The 1.86 to 1.80 Ga, Paleoproterozoic, Trans Hudson Orogeny intersects the western border in response to the subduction of the Superior Craton plate below the Saskatchewan Craton (David, 1996). The Great Lakes tectonic zone (GLTZ) separates the Wawa subprovince from the Marquette greenstone belt and the Minnesota Valley gneiss terrane to the south (Williams et al., 1991). The GLTZ was a zone of active compression during the late Archean (Sims et al., 1980).

The Wawa subprovince hosts several mineralized greenstone belts situated in two zones of linear concentrations. Along its northern border with the Quetico subprovince are the Shebandowan, Schreiber-Hemlo, Manitouwadge-Hornepayne, White River, Dayohessarah and Kabinakagami belts, whereas in the south-central part of the Subprovince are found the Mishibishu, Michipicoten, and Gamitagama belts (Fig. 2.3). These greenstone belts are composed dominantly of mafic volcanic rocks, with smaller amounts of ultramafic, intermediate, and felsic flows. Sedimentary rocks are predominantly siliciclastic turbiditic wackes and shales, with minor amounts of conglomerates, iron formations and carbonates. Domains of tonalite-trondhjemite-granodioritic plutonic rocks generally separate these belts. The belts of the Wawa subprovince appear to have been tectonically assembled prior to the coalescence of the subprovinces to the Superior Province (Williams et al., 1991).

The Wawa and Abitibi terranes are interpreted to be tectonically correlated and are divided on the eastern boundary of the Wawa subprovince by the Kapuskasing uplift structure (Percival et al., 2006b; Fig. 2.4). Both terranes, historically and currently, host extensive world-class orogenic gold deposits (Poulsen et al., 2000).

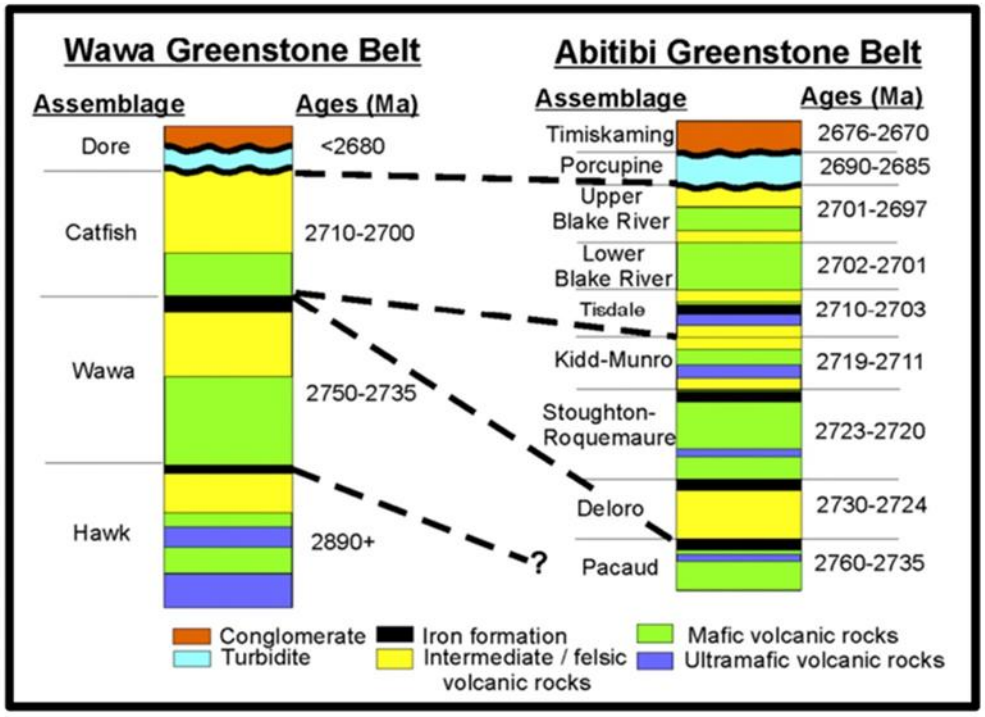

Fig. 2.4: Stratigraphy of Wawa and Abitibi subprovinces (modified from Ayer et al., 2010).

Within the Wawa terrane, volcanism appears to have begun with the 2.89-2.88 Ga Hawk assemblage followed by the bimodal Neoarchean Wawa assemblage in an oceanic environment, later forming what is interpreted as an arc-back-arc system characterized by multiple massive sulphide deposits found in the Shebandowan, Winston Lake and Manitouwadge greenstone belts (Turek et al.,1992; Corfu and Stott, 1998). In the Western portion of the Wawa subprovince, the Schreiber-Hemlo belt comprises a variety of oceanic-type magmas and is interpreted to be a tectonic mélange with later-stage volcanism at 2.689 Ga taking place during a D_1 thrusting event, subsequently 2.6 Ga calc-alkaline to alkalic magmatism and associated coarse Timiskaming type sedimentation, followed by sanukitoid magmatism (2.685-2.680 Ga) and dextral transpressive D_2 deformation (Davis & Lin, 2003; Polat et al., 1998)

2.3 Mishibishu Greenstone Belt

The Mishibishu belt (MGB) is an Archean, plutonic–volcanic greenstone belt in the Wawa subprovince, 40 km west of Wawa, Ontario. The MGB formed over at least 22 m.y. between 2.721 and 2.699 Ga. The belt trends east-west with an approximate area of 30 km by 60 km (Fig. 2.5). Based on Bennet and Thurston (1977), the Precambrian lithological units of the Mishibishu greenstone belt comprise, from youngest to oldest, mafic intrusive rocks, diabase dikes and gabbro to felsic intrusive rocks, the Mishibishu Lake stock, porphyritic monzonite, quartz monzonite and batholithic granitic rocks such as quartz monzonite, trondhjemite, granite, aplite, hornblende diorite-gneiss, and biotite granite-gneiss. The sedimentary rocks include greywacke, arkose, siltstone, argillite, conglomerate, and iron formation, whereas the volcanics include felsic to intermediate dacite to rhyolite flows, felsic to intermediate tuff, volcanic breccia, and quartz-feldspar porphyry. The oldest rocks in the belt are mafic to intermediate metavolcanic and related intrusive rocks: basalt, pillow basalt, porphyritic basalt, andesite, gabbro, and porphyritic gabbro (Keller, 1989).

An exhalative event appears to have capped this volcanic cycle, with metal-rich hydrothermal fluids forming an iron formation composed of alternating beds of chert, red jasper and magnetite or hematite. Four facies of the Michipicoten-type iron formation have been identified in the Mishibishu area. Mafic metavolcanic rock forms a cover over the iron formation, with a sharp contact between the mafic metavolcanic and the underlying banded chert-magnetite iron formation, and a sharp alternating contact between the chert magnetite member and the underlying pyrite. The pyrite member grades downward into a siderite member, and the siderite member grades downward into a felsic volcanic unit, which forms the footwall of the overall iron formation (Keller, 1989).

The clastic metasedimentary rocks in the MGB belt are likely derived from volcanic and granitoid rocks from the region. Conglomerates are common throughout, with varying clast sizes, set in an arkose wacke matrix. Previous research by Bass (1961) concluded that the conglomerates in the MGB are alluvial fan deposits, the granitic boulders likely were derived from subvolcanic intrusions, and there did not need to be a pre-existing granitic terrain. Mafic intrusive events consist of various coarse-grained, small gabbroic plugs near Loon Lake in the western region of the belt and a few plutons in the southern part of the belt (Keller, 1989). The rocks of the MGB have been metamorphosed to greenschist facies, and in some local instances, amphibolite facies have been observed. The supracrustal rocks are folded into steeply dipping isoclinal synformal structures that generally plunge to the northwest (Keller, 1989). A regional overturned syncline extends west, starting at the Mishibishu Lake Deformation Zone (MLDF) and going through to the northern boundary of the belt. A central shear zone, the MLDF trends subparallel to the strike of the metavolcanic-metasedimentary sequences, extending about 35 km from the southeast boundary of the belt to the northeast Mishibishu Lake, parallel to the northern contact of the Northern Batholithic complex (Keller, 1989). South of the MLDF is the Dorset and Rook deformation zones, and continuing to the south lies the east-west striking Eagle River deformation zone and associated No Name Lake deformation zone. The belt is bounded on the north side by the Pukaskwa deformation zone, which is oriented generally north-east (Bennet & Thurston, 1977).

2.4 The Eagle River Deposit

The Eagle River mine (Fig. 2.6), owned and operated by Wesdome Gold, is 50 km west of Wawa, Ontario, and has produced 1,050,000 ounces of gold from 3.6 million tons, averaging 9.1 g/pt Au (Michaud, 2019). The deposit is a Neoarchean orogenic gold deposit hosted in the southern limb of the Mishibishu Greenstone Belt. The deposit is within the Eagle River deformation zone, south of the Mishibishu Lake deformation zone. Mineral reserve estimates of total ore, as of December 31, 2021, were 116 kt at 11.3 g/t for a contained Au of 42,000 Koz. Probable reserves are 1,066 kt at 15.3 g/t with contained Au of 524,000 Koz (SRK, 2022).

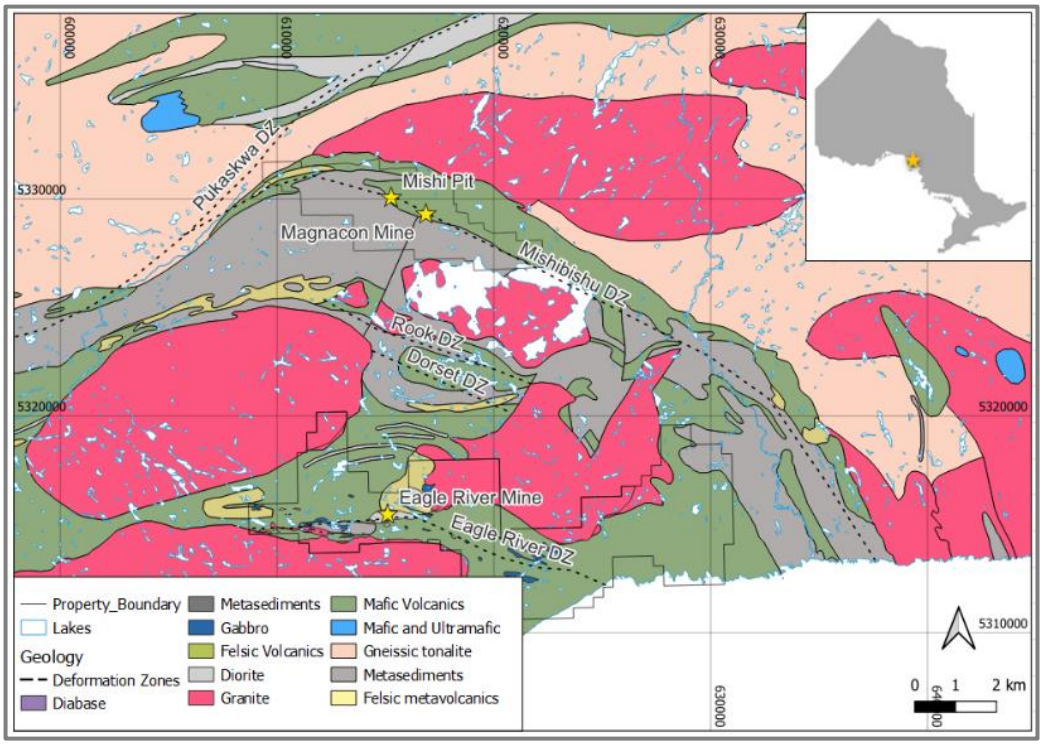

Fig. 2.6: Geological map of Eagle River mine, Mishi Pit and the Pukaskwa, Mishibishi, Rook, Dorset and Eagle River deformation zones. Map modified from Wesdome Gold's exploration department.

The Eagle River mine is comprised of tightly folded, isoclinal gold-bearing quartz veins hosted primarily in sub-vertical to steeply north-dipping, east-west striking, ductile, shear zone

networks. The host rock for the mine is a quartz diorite stock that intrudes steeply dipping north-facing mafic to intermediate volcanic flows, tuffs, and interflow volcaniclastic rocks. There are several mineralized zones within the Eagle River deformation corridor. Zones 6, 7 and 8 are hosted within the quartz diorite pluton. Zone 2, east of the mine, extends from the diorite into mafic volcanics; the Falcon zone is the latest discovery by Wesdome Gold's exploration department (Wawrzonkowski, 2024). It is primarily hosted in intermediate volcaniclastic rocks and is thought to extend to the west of the 7 Zone. The 9 Zone, an active area of interest, is hosted in mafic volcanic rocks northwest of the mine. To the southwest of the mine, gold-bearing, east-west striking, felsic volcaniclastic rocks, and mafic volcanic rocks are present in shear zones at or near lithological contacts.

Gold mineralization at the Eagle River mine and area is concentrated in highly strained, lenticular quartz-carbonate veins, white to grey in colour, with accessory sulphide minerals comprising pyrite, pyrrhotite, galena, sphalerite, and chalcopyrite. Gold tends to be preferentially associated with sphalerite and galena (SRK, 2022). Most gold occurs along quartz-carbonate-sericite-chlorite grain boundaries, and smaller amounts are directly associated with sulphide minerals. Recent U-Pb geochronology results for the Eagle River mine and nearby area lithologies were presented by Wawrzonkowski (2023; Fig. 2.7). Geochronology studies in the area have yielded ages of 2721.2 ± 4.1 Ma for the Eagle River mine diorite and 2658.35 ± 0.41 for the nearby Bowman Lake batholith (Turek et al., 1984; Keller, 1986).

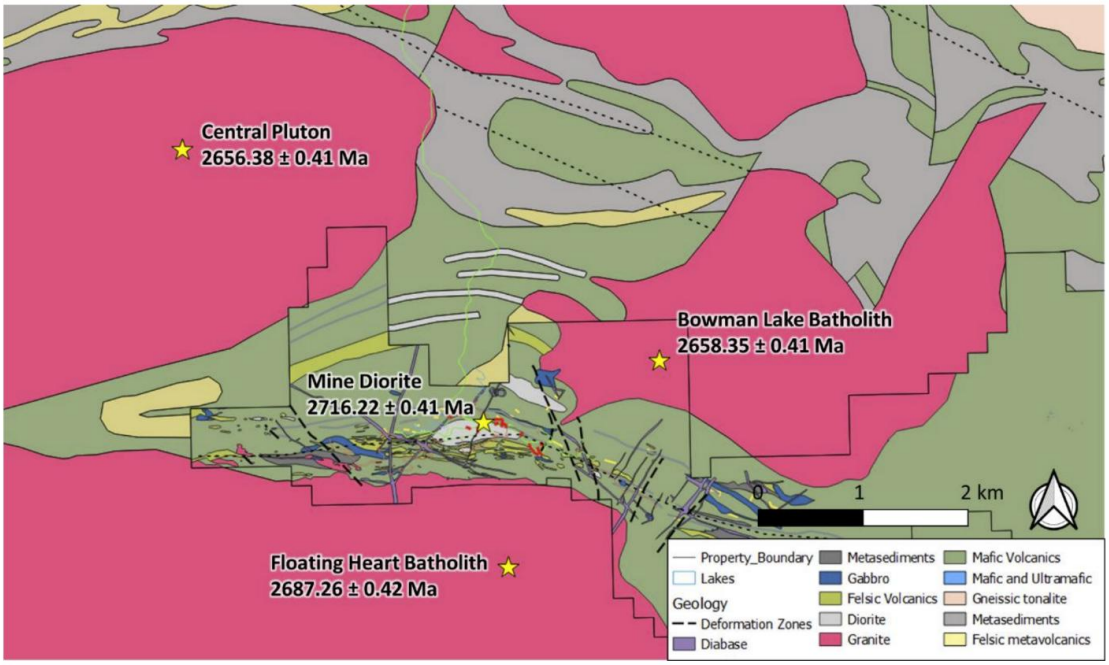

Fig. 2.7 - Geological map with recent geochronology results from the Eagle River and nearby areas (Modified from Wesdome Gold exploration department; Turek et al., 1984; Keller, 1986; Wawrzonkowski, 2023).

Chapter 3: Methodology

3.1 Materials and Methods

A series of techniques have been used to investigate the geological setting, kinematics, and geochemical footprint of alteration at the Eagle River deposit; these include detailed structural field mapping, petrography, whole-rock geochemistry, Sm-Nd isotope analysis, macro and microstructural analysis of shear zones and faults, U-Pb geochronology, EBSD mapping of quartz grains, crystallographic vorticity analysis, TitaniQ and chlorite geothermometry.

3.2 Field Study

A detailed kinematic field study was conducted northeast of the Eagle River mine using a tablet with Strabo Spot software for structural measurements and data collection. The focus was on kinematic analysis of an NW striking property-wide fault that crosscuts the Eagle River deformation zone, mapping the extent of the northern diorite unit, Birch Vein area and the Eagle River mine shear zones. Field samples were collected from notable structures to prepare oriented thin sections, and whole-rock geochemistry grab samples were selected based on alteration and lithology. Shear zones 2 and 8 were channel sampled for thin-section analysis. The channel was cut and prepared perpendicular to the veins and shear fabric (E-W) from N to S.

3.3 SEM-supported petrography

A total of 50 polished thin sections were created for this project. Reflected and transmitted light petrographic reports can be found in Appendix A. The Hitachi SU-70 Schottky Field Emission SEM equipped with an Oxford Aztec 80 mm/124 EV electron dispersive X-ray

spectrometer (EDX) was used at Lakehead University to conduct quantitative analyses of minerals while using a 15 mm working distance and an accelerating voltage of 20 kV.

3.4 Macrostructural Analysis

Structural measurements were collected while mapping in the summers of 2022 and 2023 and were plotted using software programs Stereonet v. 11 (Allmendinger et al., 2012) and Seequent's Leapfrog geological modelling software.

3.5 Microstructural Analysis

Fifteen oriented, polished, thin sections were prepared for microstructural analyses from structures of interest in the field and shear zones 2 and 8 channel samples. Samples were cut perpendicular to foliation and parallel to lineation. Kinematic-bearing microstructures were then analyzed and chosen for representative photomicrographs. Quartz microstructures were analyzed for evidence of dynamic recrystallization.

3.6 Lithogeochemistry

A total of 41 field samples were collected to investigate the geochemical footprint of the Eagle River mine and area. Samples were prepared at ALS Labs in Thunder Bay, Ontario. The first stage involved fine crushing 70% at < 2 mm, then pulverizing up to 250 g of 85% <75 µm and splitting with the riffle splitter. Analytical procedures included inductively coupled plasma mass spectrometry (ICP-MS) of up to 34 elements per sample with atomic mass ranges of 7 to 250 (Li to U). Loss of ignition (LOI) was performed at 1000°C to estimate the amount of water, carbon dioxide and organic matter. The whole rock package uses an inductively coupled plasma-atomic emission spectrometer with total carbon and sulphur IR spectroscopy for trace element

analysis. Lithium borate fusion sample preparation was completed before inductively coupled plasma mass spectrometry for rare earth elements (raw data are presented in Appendix B).

3.7 Electron Microprobe Analysis of Chlorite and Ti-in-Quartz

Electron microprobe microanalysis (EMPA) was conducted at the University of Toronto. Chlorite-rich areas of the fault gouge in samples A and B from drill hole ER-026 were selected and sent to the University of Toronto for carbon coating and EMPA analyses. Compositional analyses were acquired on a JEOL 8230/8530 (TCP/IP Socket and EIKS) electron microprobe equipped with five tunable wavelength dispersive spectrometers. Analyses were collected using a take-off angle of 40°, an accelerating voltage of 15 keV, a beam current of 20 nA, and a beam diameter of 10 microns. Standards were run before and after the chlorite analyses.

Titanium concentrations in quartz from the Eagle River mine shear zones were analyzed to determine the recrystallization temperatures of deformation zones. Four thin sections were selected due to the presence of rutile and the microstructural characterization of quartz grains. This thermometry technique is based on Wark & Watson (2006). Over 140 spot analyses were retrieved. Secondary silica standards for Ti (100 ppm, 500 ppm, 1000 ppm) were used from the University of Edinburgh (https://www.ed.ac.uk/research-innovation).

3.8 EBSD Mapping

Four Eagle River shear zone samples were selected for EBSD analysis. Each sample was polished with a colloidal silica polish for 1 hour before analysis. EBSD patterns were collected using a Symmetry 2 detector on a Tescan TIMA SEM (University of California) with a tilt angle of 65°, an accelerating voltage of 20 kV, a working distance of 27 mm and a step size of 10 μm and collected in low vacuum mode. Random orientation analyses was used to test if the samples are consistent with a random distribution or show a preferred orientation. If the orientations are random, the material has little or no texture. If orientations cluster, the sample has a preferred orientation, which may reflect deformation, recrystallization, growth, or phase transformation processes. Energy dispersive X-ray spectrums (EDS) were collected synchronously during the data acquisition of EBSD patterns. MTEX, a Matlab toolbox for analyzing and modelling crystallographic textures by means of EBSD or pole figure data, was used for post-processing raw data (Bachmann et al., 2010, 2011).

3.9 Crystallographic Vorticity Axis Analysis (CVA)

The four samples that underwent EBSD analysis were selected for further crystallographic research. CVA analysis is a new technique for grain-scale vorticity analysis. It evaluates vorticity at the individual grain scale. Grain-scale dispersion axes can be evaluated in quartz aggregate to determine the position of a specimen-scale (i.e., bulk) vorticity axis. CVA analysis assumes the record of crystal plastic deformation is recorded by individual deformed grains and leverages rotational statistics to calculate a single grain-scale dispersion axis from the rotational distribution of all crystallographic orientations within a particular grain, providing

insights into the region's bulk strain. This technique provides another layer in helping us better understand shear zone kinematics (Michels et al., 2015).

3.10 Radiogenic Isotopes (Sm-Nd)

The Eagle River samples were analyzed at the Earth Resources Research and Analysis Facility at Memorial University, St. John's, Newfoundland. Whole rock powders were dissolved in Savilex © Teflon capsules using a mixture of HF and HNO_3. Prior to acid digestion, a mixed $^{150}Nd/^{149}Sm$ spike was added to each sample. After digestion, the samples were dried and taken back up in various mixtures of HCl. Samples were then loaded into a column containing cation exchange resin, where Sr fractionation can be isolated, followed by the collection of bulk rare earth elements (REES). This bulk sample was then dried, taken up in HCl and loaded on a second column containing Eichrom © Ln resin to isolate Sm and Nd separately from the other REES. Sm and Nd concentrations were determined using a multi-collector Finnigan Mat 262 mass spectrometer (TIMS) in dynamic mode for isotopic composition determination. Instrumental mass fractionation of Sm and Nd were corrected using a Raleigh law relative to $^{146}Nd/^{144}Nd = 0.7219$ and $^{152}Sm/^{147}Sm = 1.783$. The reported $^{143}Nd/^{144}Nd$ ratios were corrected for the deviation from repeated duplicates of the standard JNdi-1 ($^{143}Nd/^{144}Nd = 0.512115$; Tanaka et al., 2000). Replicates of the standards give a 6-month mean value of $^{143}Nd/^{144}Nd = 0.512102 \pm 14$ (2SD, n=18) for JNdi-1. Analyses of the USGS standard BCR-2 were included in each batch using a separate dissolution and thus provide the best estimate of the reproducibility of an individual whole rock analysis.

3.12 U-Pb Geochronology

One Northern Diorite sample was delivered for geochronology analysis to the Pacific Center for Isotopic and Geochemical Research of the University of British Columbia (PCIGR, 2023). The methodology applied was that of Mattinson (2005), which was adapted for the Pacific Centre for Isotopic and Geochemical Research (PCIGR) at the University of British Columbia (PCIGR, 2023).

For zircon extraction, the zircons were separated using a Wilfley wet vibrating table with a precision-machined Plexiglas surface (PCIGR, 2023). Sequentially, conventional magnetic and heavy liquid separation techniques were implemented using a Frantz magnetic separator, after which the zircon particles were meticulously selected by visual inspection with a binocular microscope (PCIGR, 2023). Hydrofluoric acid (HF) and nitric acid were introduced in a ratio of 10:1 into the liner, which was subsequently positioned within the jacket (Scoates and Scoates, 2013), sealed, and subjected to a temperature of 240°C for a duration of 40 hours to achieve complete dissolution. The resultant solutions were then evaporated on a hot plate maintained at 130°C. The fluorides were subsequently solubilized in 3.1 N hydrochloric acid (HCl) within a high-pressure apparatus for a period of 12 hours at 210°C (Scoates and Scoates, 2013). The methodologies for the separation and purification of lead (Pb) and uranium (U) utilized ion exchange column techniques that were slightly modified from the procedures delineated by Parrish et al. (1987), wherein Pb and U were eluted sequentially into a singular receptacle (Scoates and Scoates, 2013)

Zircons were analyzed using chemical abrasion thermal ionization mass spectrometry using a VG354S or VG54R thermal ionization mass spectrometer (TIMS) instrument, which employs an EARTHTIME ET535 tracer or a UBC ^{205}Pb-$^{233\text{-}235}$U isotope tracer (PCIGR, 2023).

Chapter 4: Results

4.1 Field Results

Detailed field mapping of the Eagle River mine and nearby parts of the Mishibishu greenstone belt was completed in the summers of 2022 and 2023. Field mapping focused on regions northeast and west of the mine (Fig. 4.1)

The lithologies observed have been metamorphosed to greenschist facies with some occurrences of localized lower amphibolite facies. The prefix ‘meta’ should be taken as implicit in the remainder of this thesis. Basaltic andesite, tholeiitic basalt, alkaline basalt, gabbro, diorite, granodiorite, andesite, and felsic volcanic rocks. Alteration assemblages were chlorite + actinolite + albite +/- epidote & clinozoisite. Albite, epidote, and clinozoisite are widely distributed throughout the rock units, increasing in areas of hydrothermal alteration. The following is a summary of rock-type observations collected during fieldwork. Petrographic descriptions are available under the petrographic analysis section.

Basaltic andesite is the dominant extrusive rock unit observed in the mapped area. The unit is green and fine-grained, with little to no quartz present. Plagioclase occurs in the fine-grained groundmass and forms porphyroblasts 0.5-1mm in size; in some instances, the unit appears porphyritic. Minor amounts of biotite, pyroxene and amphibole were observed. The unit is pervasively altered with chlorite, epidote, and clinozoisite and strongly foliated. Pillow structures were observed east and west of the Eagle River mine, implying a sub-aqueous environment (Fig. 4.2); the way-up direction was not conclusive. Tholeiitic basalt was observed in multiple areas near the Eagle River mine. The unit is dark green to nearly black in colour, very

fine-grained and strongly foliated. Biotite, pyroxenes and olivine occur in minor amounts; plagioclase is very fine-grained and was rarely observed as porphyroblasts. The eastern extent of the 2-Zone sheared quartz veins is hosted in iron-rich, tholeiitic basalt along with multiple E-W brittle faults on the Eagle River property (Fig. 4.2b).

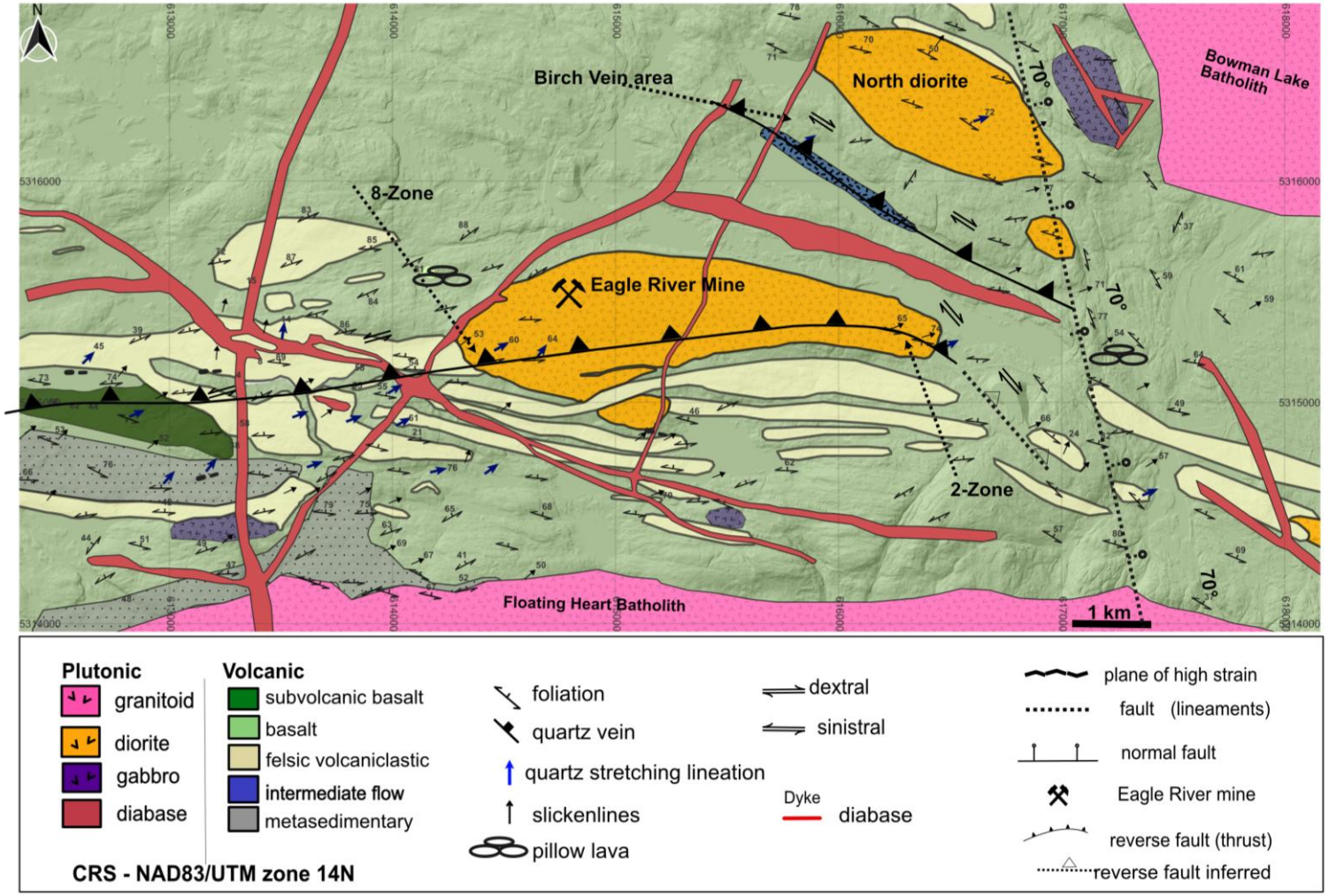

Fig. 4.1: Geological map of Eagle River mine and area

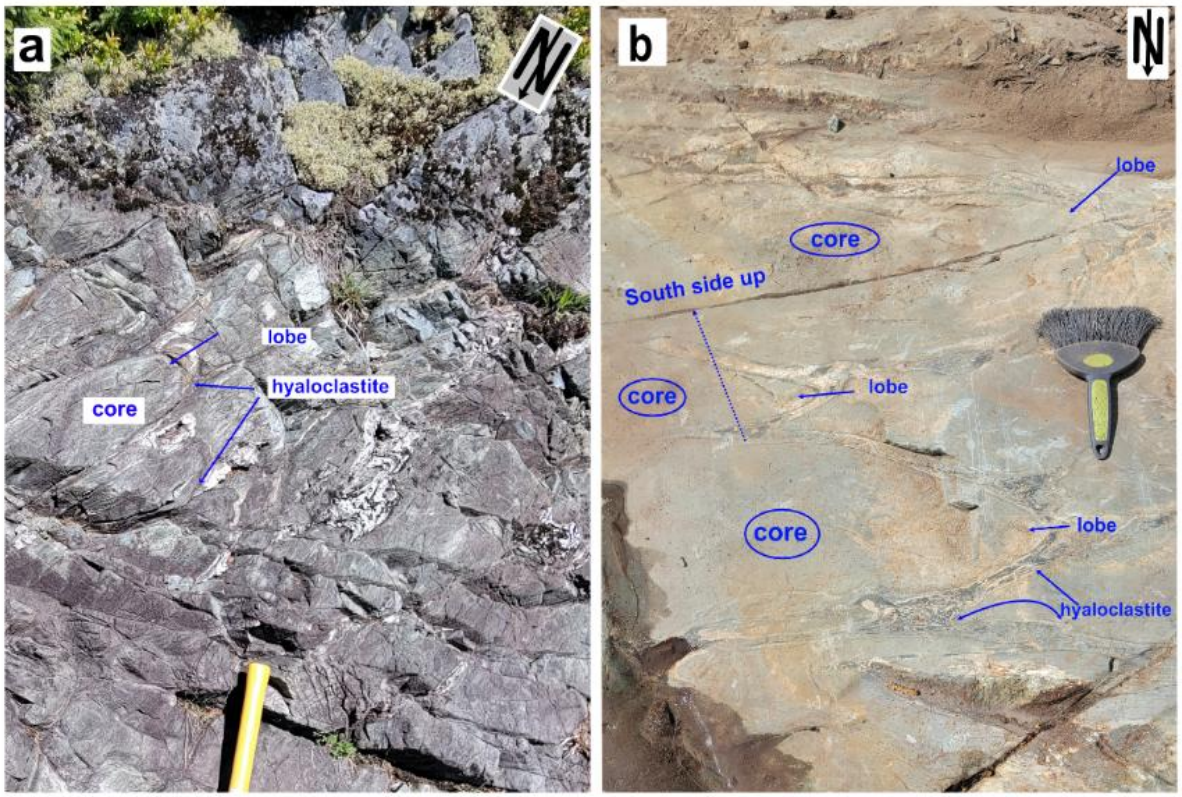

Fig. 4.2: Field images of two pillow structure outcrops; a: located east of the mine, pillows that have undergone deformation and altered at margins with calcite; b: less deformed pillows located 500 meters west of the mine with strongly developed chill margins of hyaloclastite and tabular lobes on either side of each pillow structure. The pillow locations are indicated in Figure 4.1.

Intermediate volcanic rock, also known as meta-andesite, is commonly found in long, narrow strips near or connected to diorite plutons, or associated with other volcanic units (Fig. 4.1). It is grey in colour, with a porphyritic, highly siliceous, and sugary texture. Plagioclase is the dominant mineral with a grain size of up to 3 mm and lesser amounts of hornblende up to 1 mm in size. Very fine-grained quartz and phyllosilicates, including biotite and muscovite, were observed. Alteration minerals observed are chlorite, epidote, and clinozoisite. An andesitic volcaniclastic flow unit occurs south of Birch Vein on the shore of Lake Wesdome (Fig. 4.1). Clasts are andesitic and observed to be symmetrical, up to 15 cm long, and margins have been

infilled with epidote. E-W striking flow banding is prevalent throughout the unit; this is discussed further under the Birch Vein section.

Felsic volcaniclastic rocks are common in the Eagle River mine and area, with the unweathered surface being beige to white in colour (Fig. 4.3). Mineralogy is characterized by fine-grained quartz, oligoclase, porphyritic andesine, hornblende, biotite and muscovite. The unit is highly silicious, and a fresh surface is characterized by lightly stained, green to grey, chlorite-epidote-clinozoisite alteration mineralogy (Fig. 4.3d). In some instances, the unit is interpreted as a felsic tuff with angular lithic clasts and consolidated volcanic ash (Fig. 4.3c).

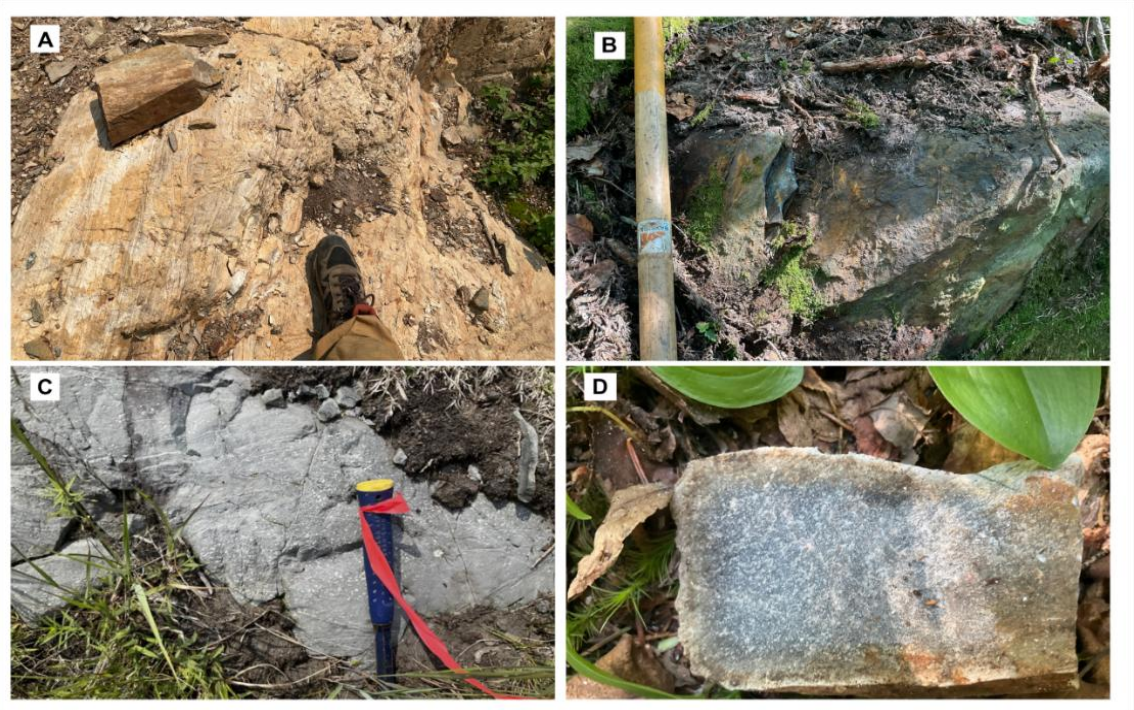

Fig.4.3: Representative volcanic rock types at Eagle River mine and area. A: Felsic volcanic rock on a weathered surface. B: Iron-rich tholeiitic basalt. C: Meta-andesite with up to 3 mm plagioclase porphyroblasts. D: The fresh surface of a highly siliceous felsic volcanic rock with 2 mm orthoclase grains (light pink).

A sedimentary unit runs south of the Floating Heart Batholith, southwest of the Eagle River mine (Fig. 4.1). The sediments comprise of fine-grained dark green/grey clastic mafic detritus and weathered grains from nearby plutons composed of silt-sized quartz, plagioclase,

biotite and muscovite grains with granite-tonalite pebbles and cobbles included within the depositional fabric (Fig. 4.4).

Fig. 4.4 – Field photos of meta-sedimentary and volcaniclastic lithologies at the Eagle River mine and nearby area; A: Conglomerate unit with very fine-grained meta-sediments with granitic clasts that are up to cobble in size, north of the Floating Heart Batholith. B: Sheared, very fine-grained, homogeneous meta-sediments west of the mine. C: Foliated felsic volcaniclastic rock.

Diorite is host to the Eagle River mine's gold-rich shear zones. Generally, the mine diorite intrusion is massive but with localized E-W shearing and quartz veins in multiple zones throughout the unit. However, with an in-depth investigation, weak foliation and relic folding can be found in the mine diorite. Plagioclase is the dominant mineral, with grain sizes ranging up to 3 mm, and hornblende up to 2 mm, accompanied by smaller amounts of albite and orthoclase. Quartz content varies but is generally less than 15%. Phyllosilicates include biotite and muscovite. The alteration mineralogy is consistent with other rock units at Eagle River, including calcite, siderite, epidote, albite, clinozoisite, and chlorite. A smaller diorite pluton is located at

the property's northern margin (northern diorite), along with several other smaller magmatic pulses of diorite that occur in the Eagle River deformation corridor to the east and west of the mine (Fig. 4.5). Blue quartz grains up to 3 mm in size are present throughout the diorite plutons (Fig. 4.5b).

Granitoid plutons are located in the northern Bowman Lake and southern Floating Heart batholith. Both batholiths comprise a number of intrusive phases including K-feldspar granite, granodiorite and tonalite. Textures are massive and porphyritic, with quartz being the most abundant mineral, occurring in grains of up to 4 mm, and plagioclase and hornblende in grains of up to 3 mm. Biotite, muscovite and minor amounts of chlorite were observed. The pluton is weakly foliated, unaltered, and has undergone extensive brittle deformation (Fig. 4 .5c, d, e, f).

Gabbro is found to the north and east of the mine in small plutons (Fig. 4.1) and has a porphyritic texture consisting of coarse-grained plagioclase and amphiboles (hornblende & actinolite) of up to 4 mm across. Fine-grained pyroxenes, biotite and olivine make up the groundmass of the rock along with alteration minerals epidote, clinozoisite, chlorite and calcite. Gabbroic plutons at Eagle River are generally less deformed compared to volcanic units (Fig. 4.1; 4.5a).

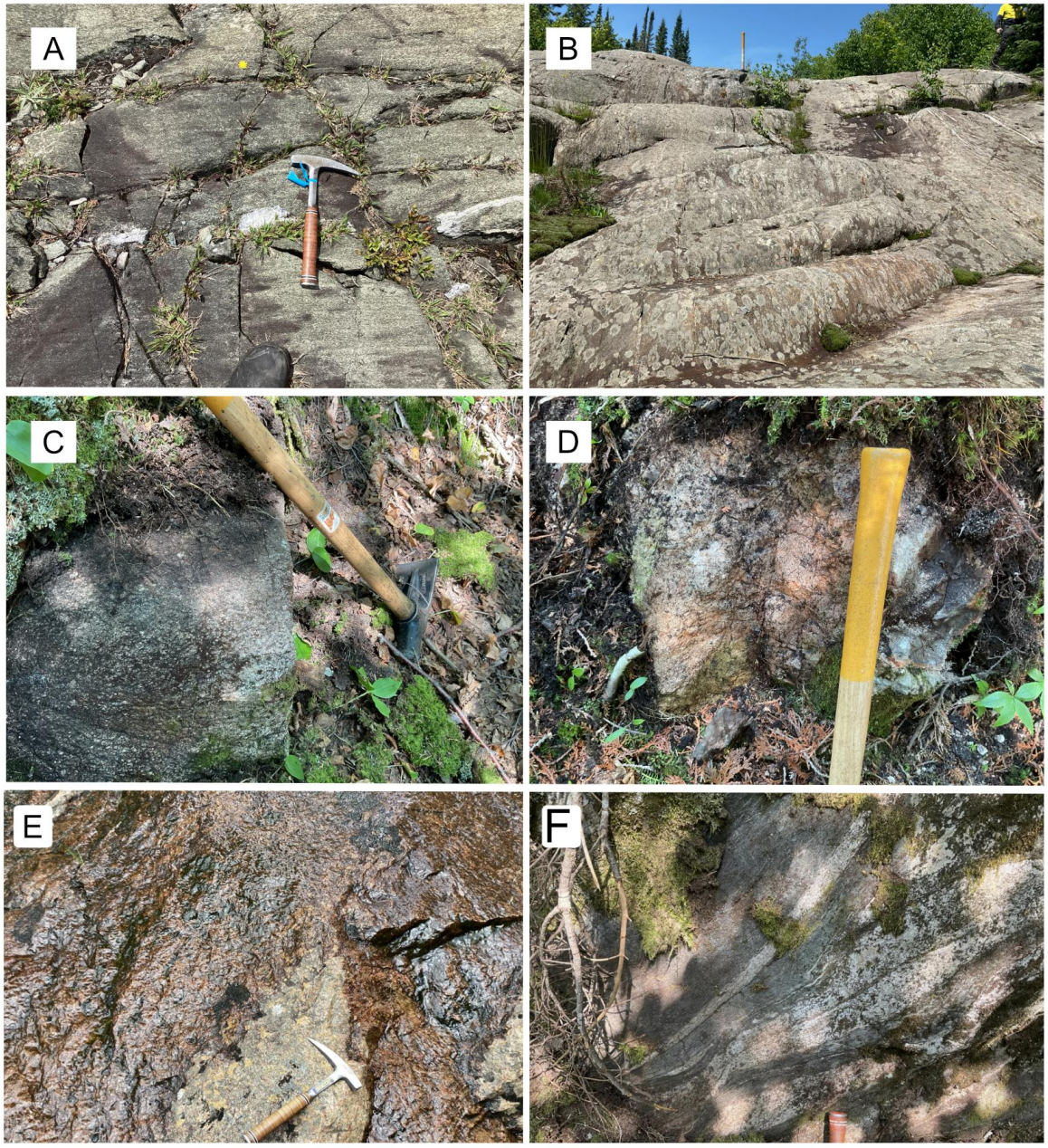

Fig. 4.5: Representative intrusive rock types at the Eagle River mine and area. A: Felsic volcanic rock on a weathered surface. B: iron-rich tholeiitic basalt. C: meta-andesite with up to 3 mm plagioclase porphyroblasts. D: The fresh surface of a highly siliceous felsic volcanic rock with 2 mm orthoclase grains (light pink). E: Bowman Lake Batholith. F: Tonalite tongues near Bowman Lake/basalt contact. The inset images represent a fresh surface of the lithology.

The mean foliation orientation north and east of the mine is 298°/72°NE, whereas to the west, it is more E-W with a mean strike and dip of 265°/70°NE (Fig. 4.6). Stretching lineations in quartz veins plunge down dip to the northeast throughout the property. Fault-associated, chlorite-defined slicken lines are vertical to sub-vertical, with the rare occurrence of one horizontal lineation instance being recorded.

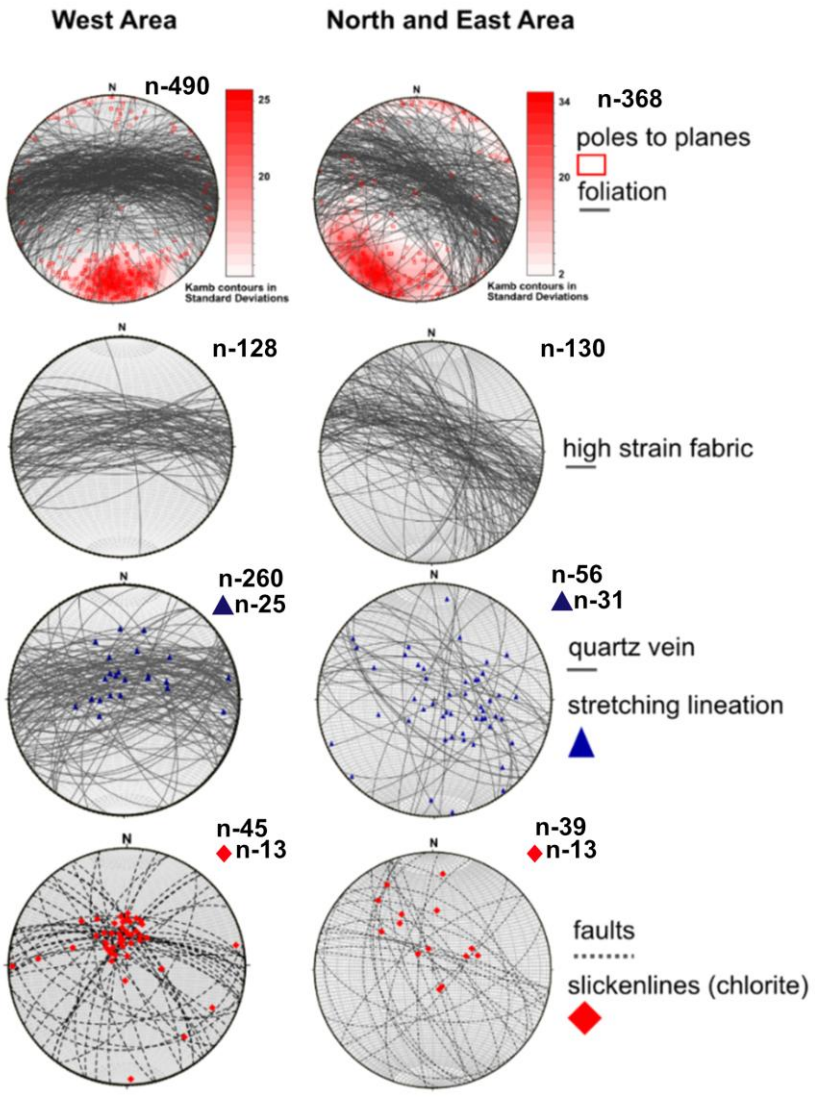

Fig. 4.6: Compilation of equal area stereonet projections of field structures west and north/east of the Eagle River mine.

Structure such as small-scale z and s folds, boudinaged quartz veins, asymmetrical, recumbent and isoclinally folded quartz veins, were observed along with strain partitioning-related structures observed at the outcrop scale in areas that underwent extensive ductile deformation (Fig. 4.7).

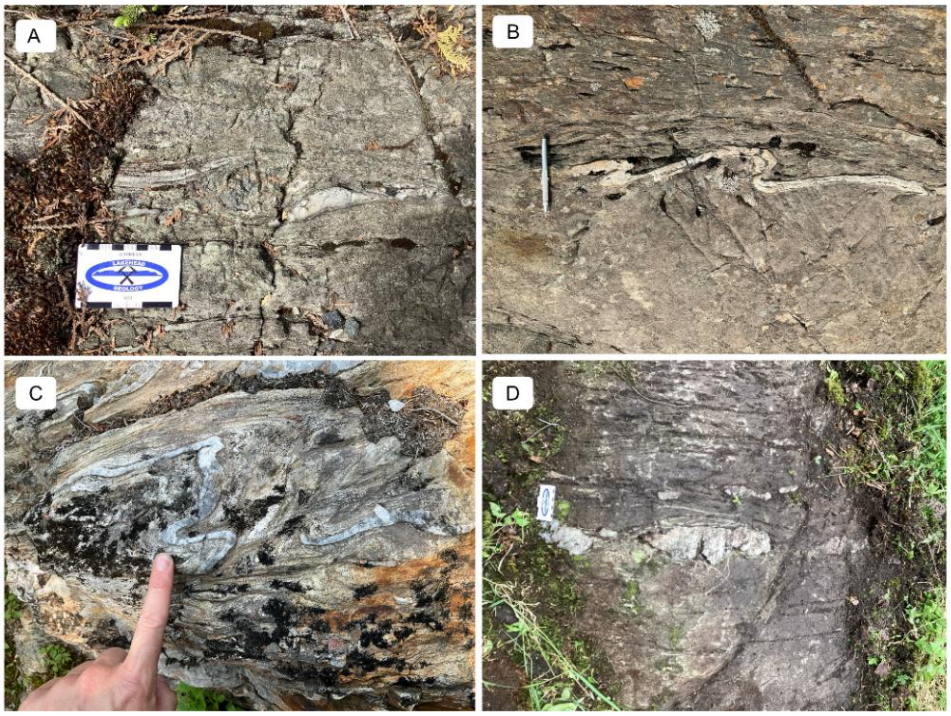

Fig. 4.7: Ductile structures located near the Eagle River Mine; A: clast with asymmetrical tails on a dextral surface with quartz infill along margins near 2-Zone; B: asymmetrically folded quartz vein; C: recumbent fold (quartz) southwest of the mine; D: boudinaged quartz veins located at 2-Zone extension.

For this project, priority was given to the area northeast of the mine, where structural data was measured and lithologies observed and recorded. This area was mapped to investigate if there were any correlations or interactions with the Eagle River mine deformation zone. The northern diorite pluton, the Birch Vein area and the E-W fault to the south, a property scale NW striking, normal fault, and gold-bearing shear zones 2 & 8 were selected for further detailed research to obtain essential data on how these high-grade shear zones formed and to better

understand the kinematics and deformation mechanisms to apply these conditions for assessing other shear zones on the property.

4.1.1 Northern Diorite

The Northern Diorite intrusion is an ellipsoid-shaped pluton that is approximately 600 meters wide by 1300 meters long (Fig. 4.1). A late property-wide-brittle fault crosscuts the eastern tip of the northern diorite. The diorite was observed and confirmed with geochemical analysis on the east side (hanging wall) and the west side of the fault (footwall). The center of the pluton is massive, medium-grained, and equigranular, with little to no alteration observed (Fig. 4.8a). Areas of higher strain characterize the north diorite's northern extent and include gold-bearing structures where the pluton is observed to be more weathered and deformed than any other area of the northern diorite. Narrow strips of siliceous andesite interbedded with mafic volcanic rocks were observed at the northern contact. The southern extent of the pluton was observed to have undergone a higher degree of alteration in contrast to other areas of the pluton.

The northern extent of the northern diorite shows a strong NW foliation. The pluton, on average, is weakly foliated; however, localized shear zones were observed (Fig. 4.9).

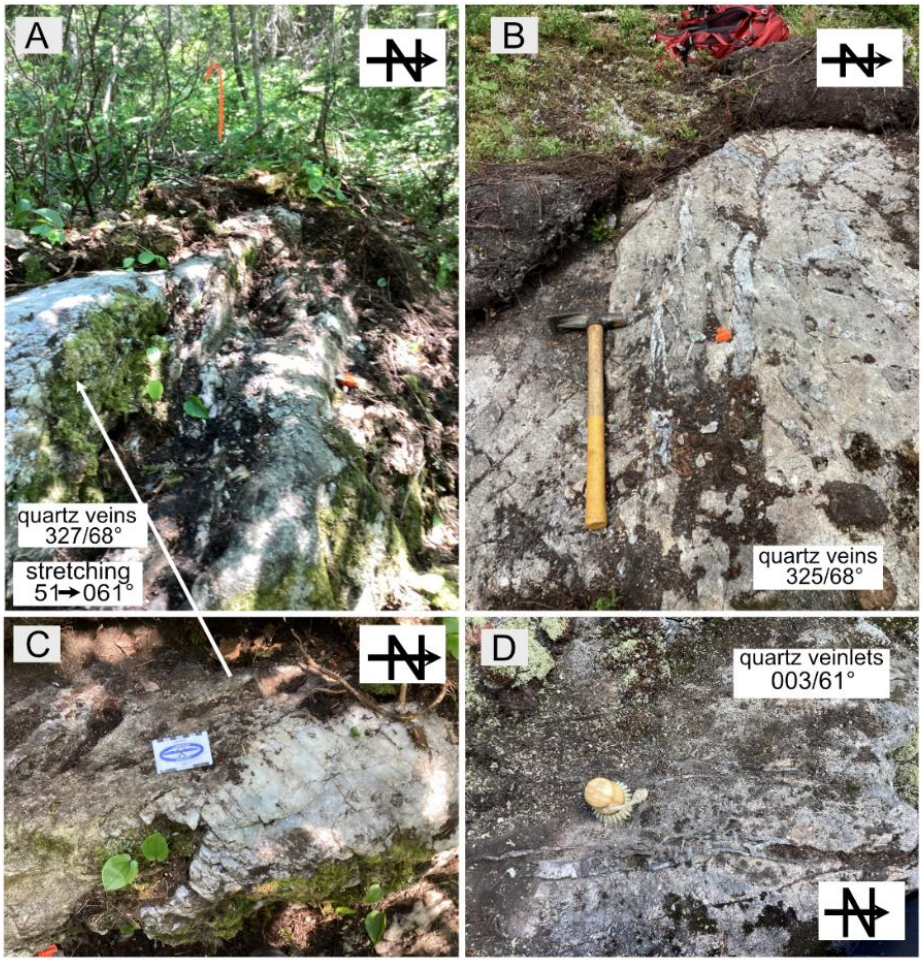

Fig. 4.8: Structure in the North Diorite. A: Localized shearing and associated quartz veins up to 40 cm wide in the northern diorite; B: quartz veins and veinlets up to 20 cm; C: Zoomed in 20 cm wide quartz vein; D: North striking shear zone with quartz veins up to 20cm.

All field structures measured in the northern diorite were plotted on equal-area stereonet projections in Figure 4.9; poles to S3 foliation planes suggest that the dominant foliation is NW, dipping steeply to the NE.

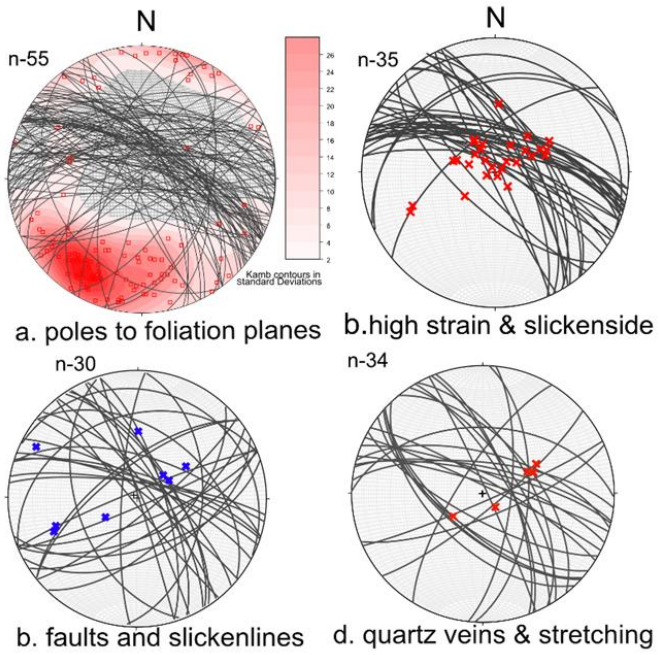

Fig. 4.9: Field structural measurements from the northern diorite pluton; poles to S3 foliations, areas of high strain, brittle faults, slicken lines, quartz veins, and stretching lineations.

Figure 4.10 is a digitized, detailed map focused on the Northern Diorite intrusion, showing areas that have been subject to ductile deformation. The pluton is cross-cut on the west margin by an NW-striking normal fault that was chosen for further research in this study.

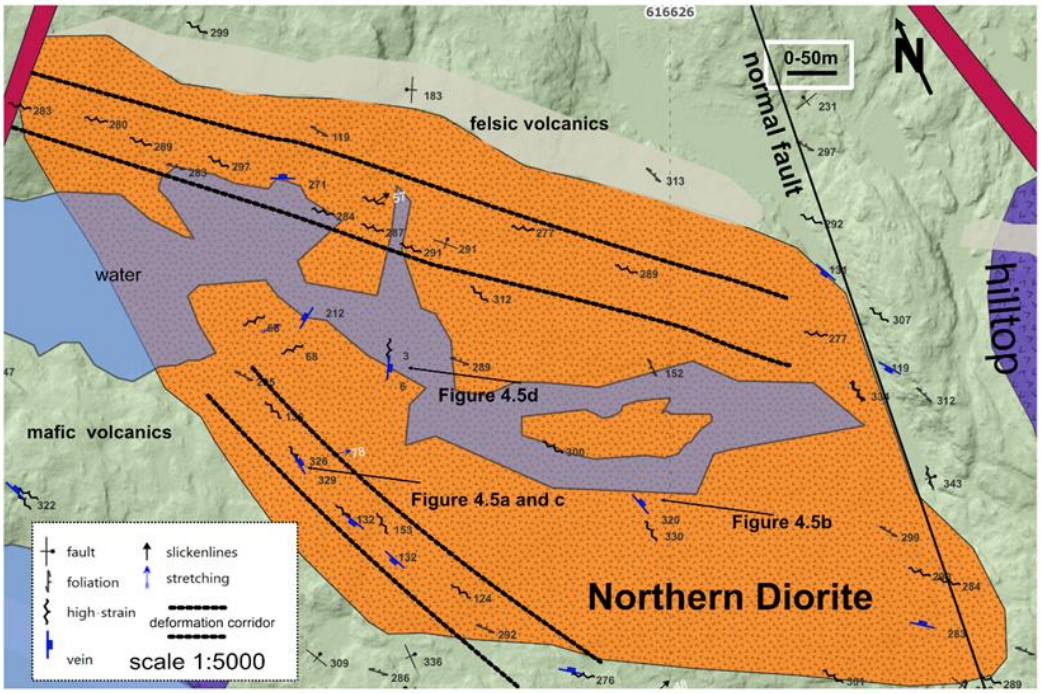

Fig. 4.10: A geological map of the Northern Diorite with symbology and structure indicated.

4.1.2 Birch Vein Complex

South of the Northern Diorite is the area historically known as the Birch Vein (Fig. 4.1). The vein complex sits on a magnetic high, on a hillside near the Northern Diorite contact. Grey to white quartz veins up to one meter wide, with small amounts of pyrite and chalcopyrite, make up the exposed outcrop. Outcrops are limited by the abundance of overburden; however, some smaller outcrops exhibit parasitic folding of quartz veinlets, indicating ductile deformation (Fig. 4.11).

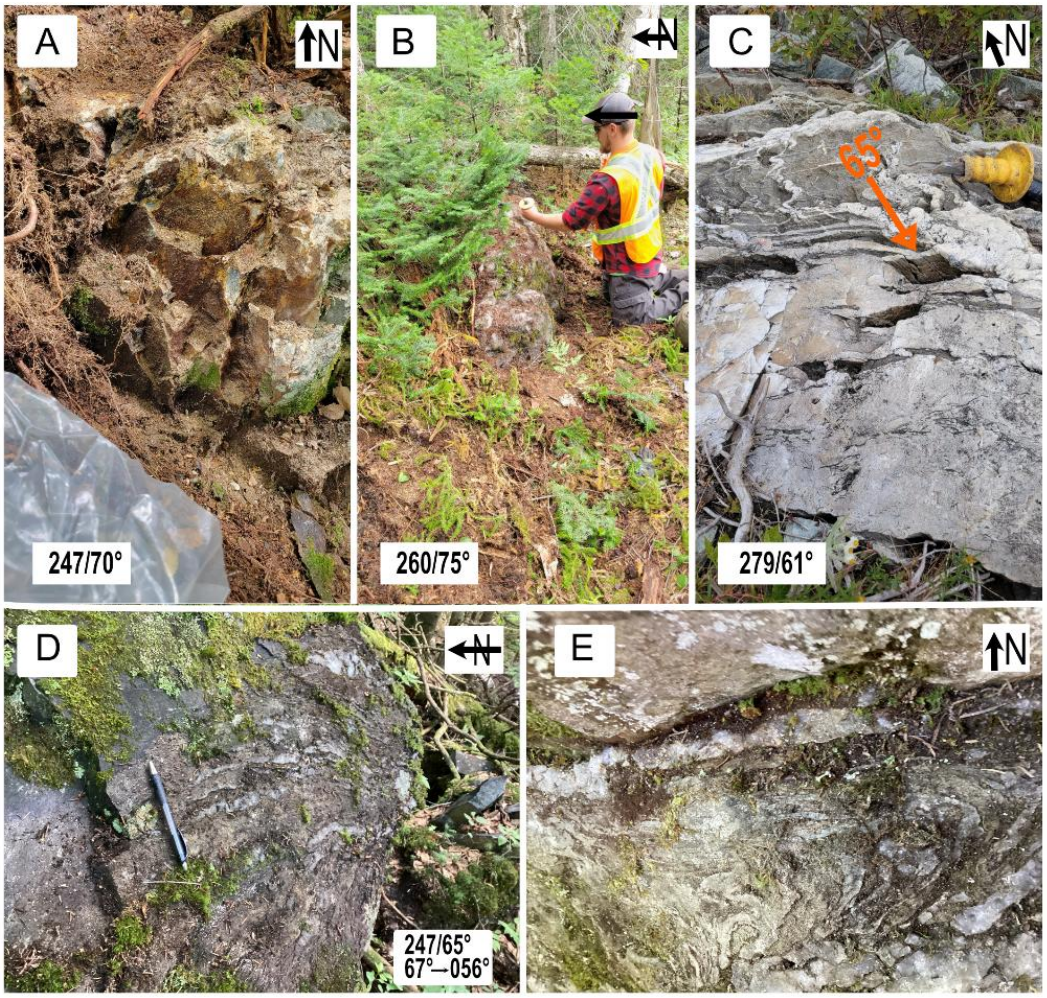

Fig. 4.11: Field images of the Birch Vein area. A: Au-bearing quartz vein and highly sulphidized host rock, the vein appears to have been blasted and historically ran up to 200 g/t Au. B: Large meter-wide quartz vein hosted in basalt. C: gold-bearing sheared quartz veining hosted in mylonite (andesite) localized at a competency contrast, which appears to be a grey material, with a stretching lineation of 65°. D: second-order deformed quartz veinlets. E: symmetrical, second-order parasitic folded quartz veinlets verging to the west.

The dominant lithology in the Birch Vein area is mafic volcanic rock, gabbro, andesite, and metasedimentary rocks. The shear fabric is parallel with the N-S shortening foliation of the area; quartz veins are parallel with the shear fabric and stretching lineations are vertical to sub-vertical relative to the shear fabric plane (Fig. 4.12).

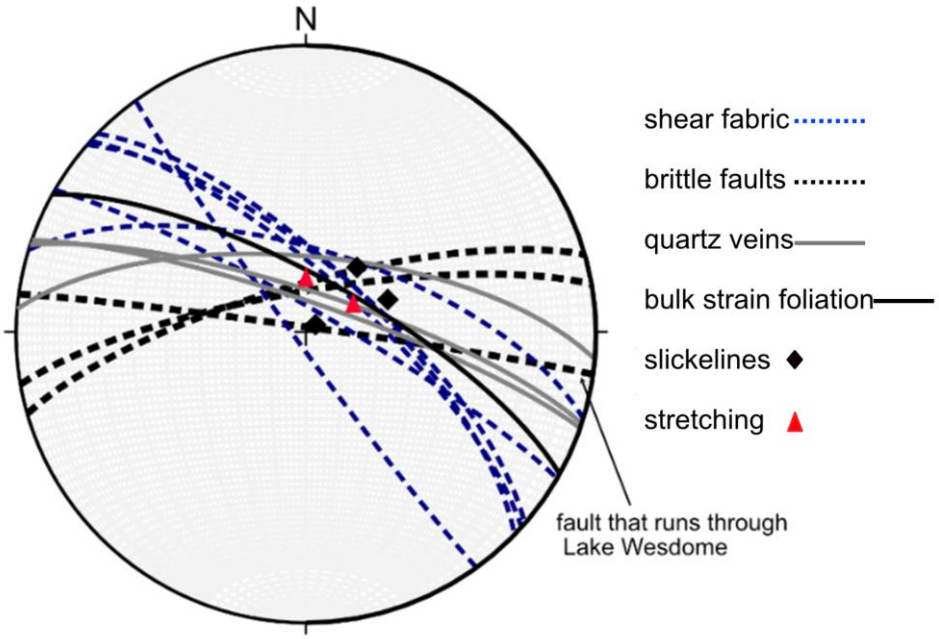

Fig. 4.12: Birch Vein and area measurements plotted on an equal area stereonet.

The east-west structure south of the Birch Vein complex that runs on and through Lake Wesdome is interpreted as a brittle fault that runs eight hundred meters east and terminates at the NW property-wide fault that was selected for further research for this study (Fig. 4.1). The structure has multiple instances of gold-bearing ductile deformed quartz veins at its northern extent (Fig. 4 .11c). On the north shore of Lake Wesdome is a 50cm wide aplite dike that was observed to be folded, with both limbs verging to the west and diabase dikes running parallel with the structure on the north side (Fig. 4.13).

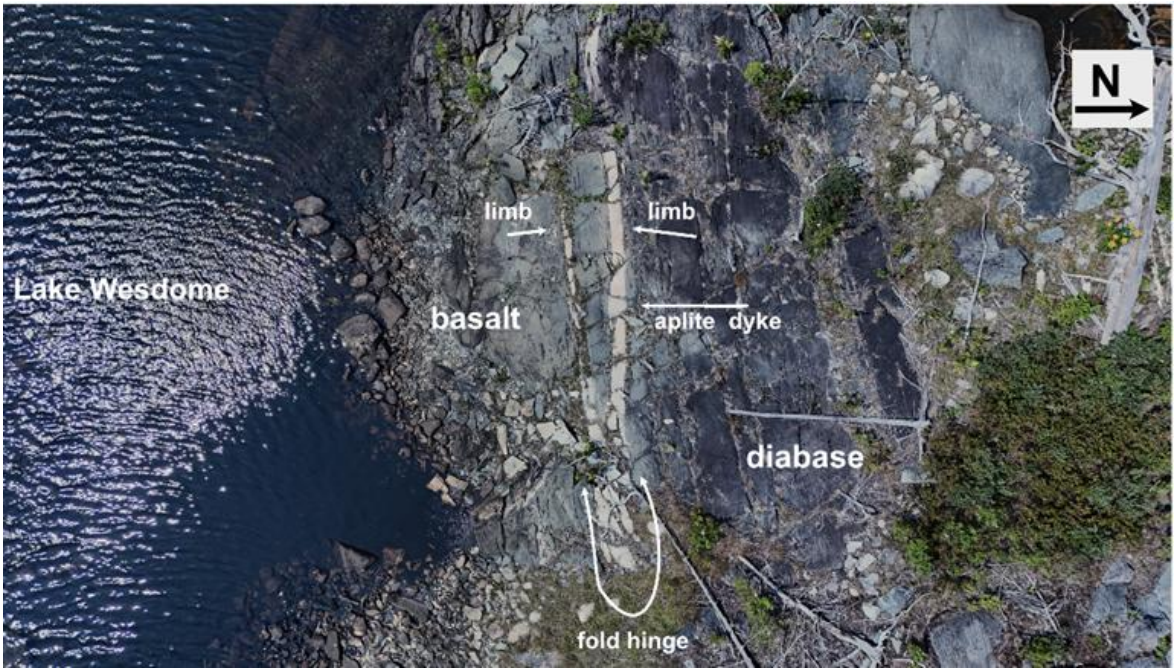

Fig. 4.13: Drone image, taken at a 25 m altitude of a folded aplite dyke with both limbs verging west with diabase to the north and basalt to the south.

The lakeshore of Lake Wesdome (East-West) comprises an andesitic flow unit with andesite clasts bearing symmetrical tails and some larger epidote-stained volcanic bombs of up to 20cm (Fig. 4.14).

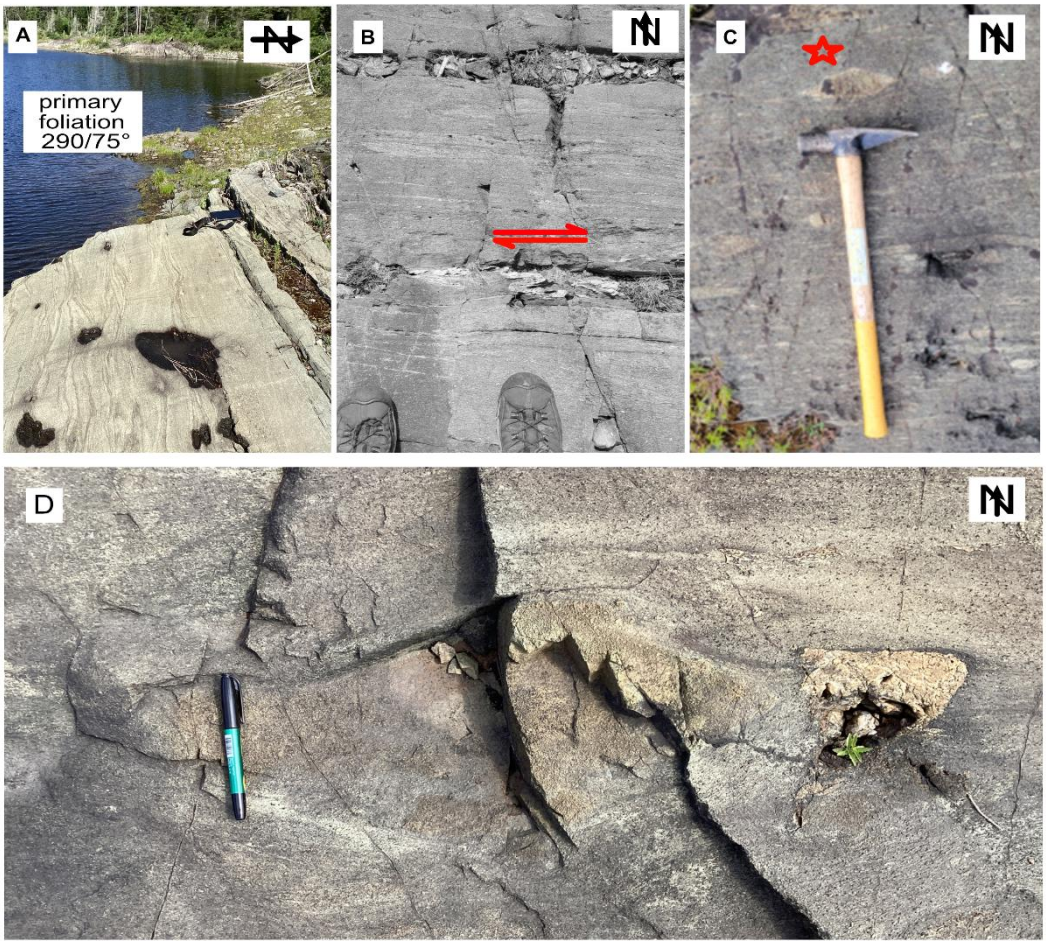

Fig. 4.14: Field images of south of Birch Vein complex. A: an andesitic flow unit with E-W flow banding. B: Andesite with andesitic clasts with symmetrical tails. C: Gold-bearing sheared quartz veining hosted in (andesite) localized at a competency contrast. D: Volcanic bomb comprised of epidote-stained andesite hosted in an andesitic flow with up to 2mm amphibole porphyroblasts (hornblende).

Field observations and stereonet projections suggest that the structure south of the Birch Vein is a poly-phase, high-angle, north-over-south reverse shear zone with a dextral lateral component that overprints gold-bearing quartz veins that have been subject to ductile deformation (Fig. 4.14). The Birch Vein complex, which is 30 meters north, is likely associated with the structure at and near Lake Wesdome. The most weathered and altered rocks on the property are in this area.

4.1.3 NW fault

A fault that strikes NW and dips 70° to the NE crosscuts the extent of the Eagle River property and was selected for further research to investigate its kinematics and formation conditions to help assess whether it has offset the Eagle River deformation zone and associated mineralization (Fig. 4.1). The fault crosscuts granite in the south, mafic volcanic rocks, the Northern Diorite, and felsic volcanic and then continues north of the Eagle River Property (Fig. 4.15).

Fig. 4.15: Photos of the NW striking late brittle fault. The footwall is to the west, and the hanging wall is to the east.

Structural measurements of the fault plane and chlorite-defined slicken lines were gathered and plotted on stereonet projections (Fig. 4.16). The fault damage zone has been weathered away at the surface; however, drill hole ER-22-026 intersected the fault at depth and was utilized for the related fault gouge and damage zone lithologies. Slickenlines occur downdip on the fault plane, and no ductile characteristics were observed. Chlorite-defined slickenlines indicate normal movement on the fault.

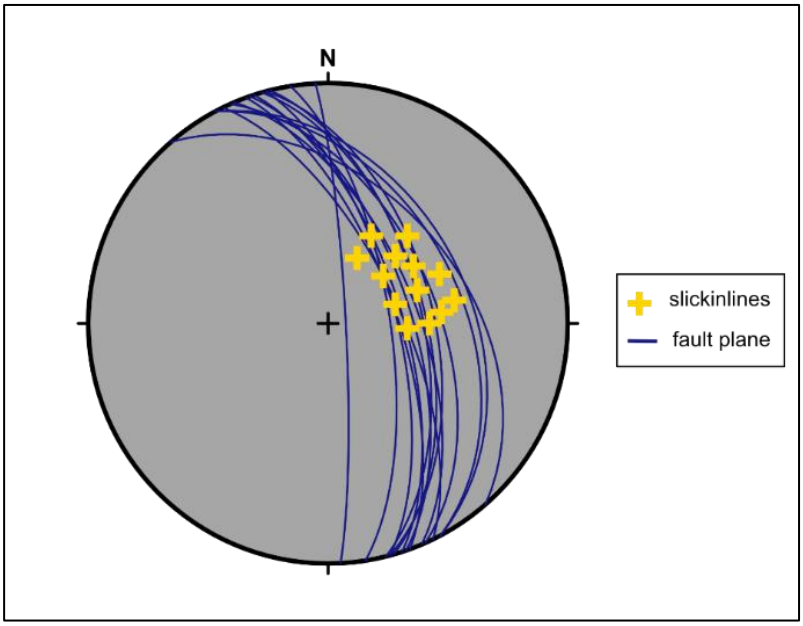

Fig. 4.16: Fault planes and chlorite-defined lineation: slickenlines plotted on an equal area stereonet projection.

4.1.4 Auriferous Shear Zones at Eagle River Mine

Gold-bearing shear zones 2 and 8 were selected to better understand formation conditions, kinematics, and deformation conditions and how they relate to mineralization (Fig. 4.1). The localized shear zones are hosted in a diorite intrusion. Gold mineralization is predominantly hosted in locally sheared quartz veins in sub-vertical to steeply north-dipping, east-west striking, lenticular, sheared and isoclinal folded quartz veins.

2-Zone Sheared Quartz Vein

The 2-Zone surface expression is characterized by a 20-metre-wide by 300-metre-long ductile deformation zone that has undergone extensive shearing, extending 300 meters west into the mine diorite and 10 meters into and along a tholeiitic basalt unit to the NE (Fig. 4.1). Sheared rock fabric that directly hosts quartz veining is observed to have undergone considerably higher temperature and pressure deformation, with grain size reduction apparent in contrast to the rigid dioritic wall rock with a very sharp contact and is interpreted as fine-grained dioritic mylonite with fractured plagioclase porphyroblasts. Grey to milky white, sugary, sheared quartz veins are prevalent, ranging from mm scale to fifty meters long and 40 cm wide. Veins have undergone intense syn-deformational isoclinal folding (Fig. 4.17).

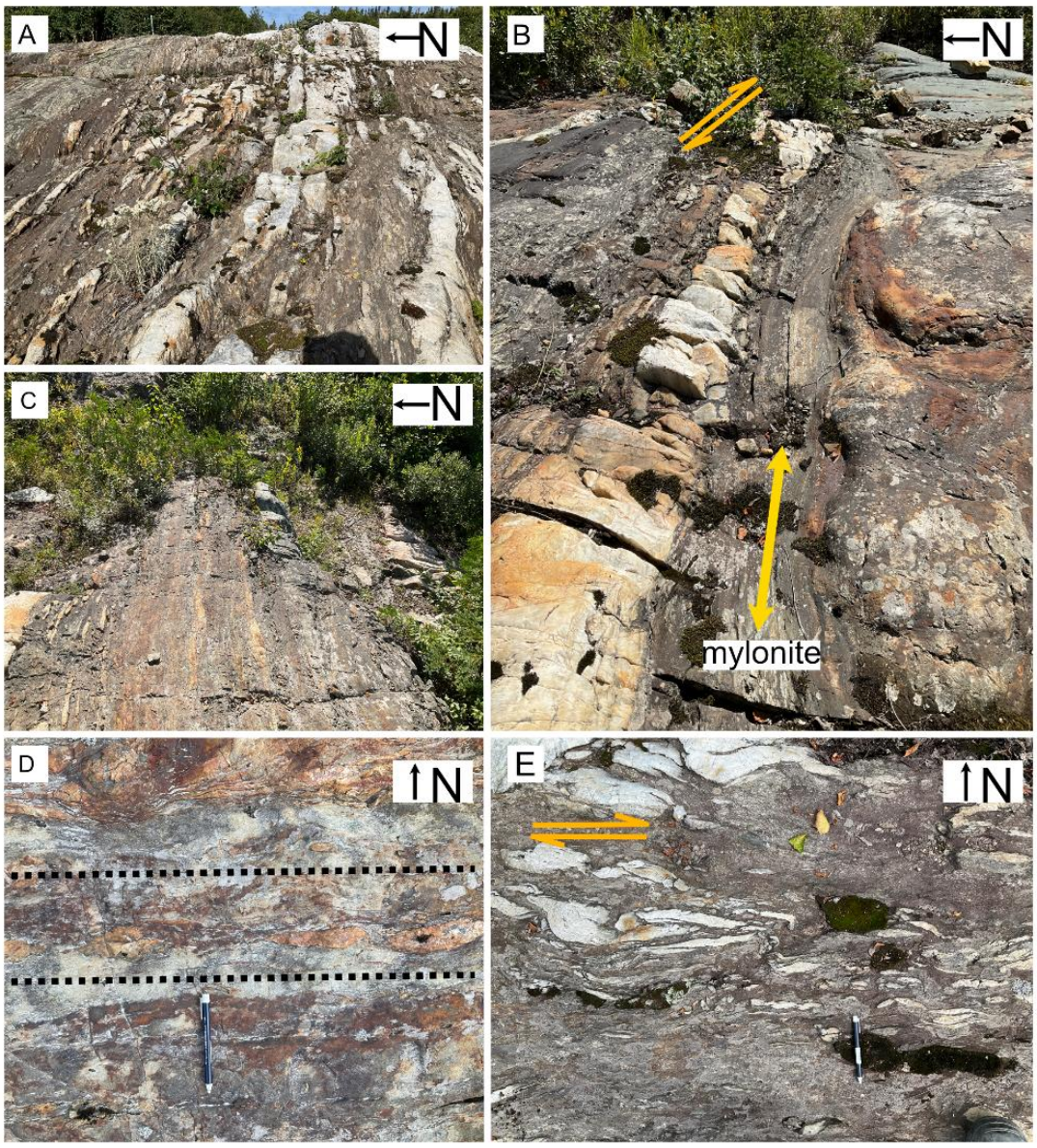

Fig. 4.17: Various domains of quartz veining at the 2-Zone. A: 10-metre-wide shear zone with multiple quartz veins and veinlets. B: 40 cm quartz vein with mylonite at both margins. C: 2-Zone Shear. D: Boudinaged quartz veins. E: Quartz veinlets showing dextral shear sense.

Sulphide content increases towards the tholeiitic basalt contact, with up to 4% sulphides in some thin sections, including pyrite, pyrrhotite, sphalerite, galena, magnetite, and hematite. Chlorite, epidote, clinozoisite, zoisite, albite, and carbonate minerals, such as siderite and calcite, characterize the alteration of the shear zone. Fine-grained, chloritic, mafic dykes run parallel to

the shear zone boundary. Shear sense indicators of the 2-Zone are dominantly dextral with north over south kinematics (Fig. 4.18).

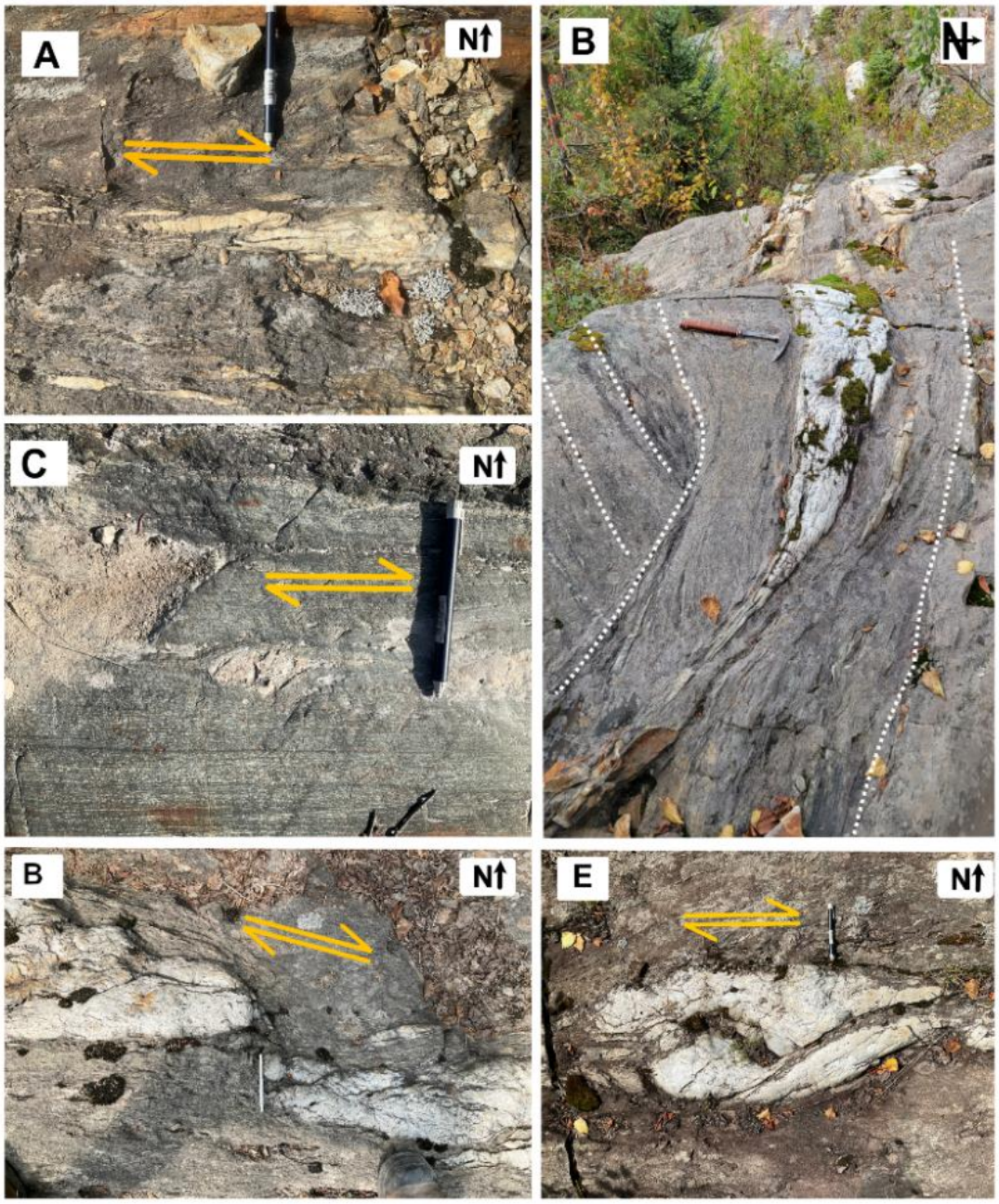

Fig.4.18: North side up (dextral) kinematics of the 2-Zone outcrop. A.: Z fold; B. Quartz vein with dextral shear sense. C. σ-b-type porphyroclast of quartz. D. Dextrally offset quartz vein (ductile) E. Quartz pod, with S-C fabrics.

The mean orientation of the 2-Zone outcrop is 280°/75°NE with a well-pronounced stretching lineation plunging 75° (down dip). The outcrop is observed to have undergone N-S shortening and is anastomosing with heterogeneous strain partitioning networks and well-pronounced S and C fabrics. The dominant movement of the 2-Zone is interpreted to be vertical, with a dextral horizontal component.

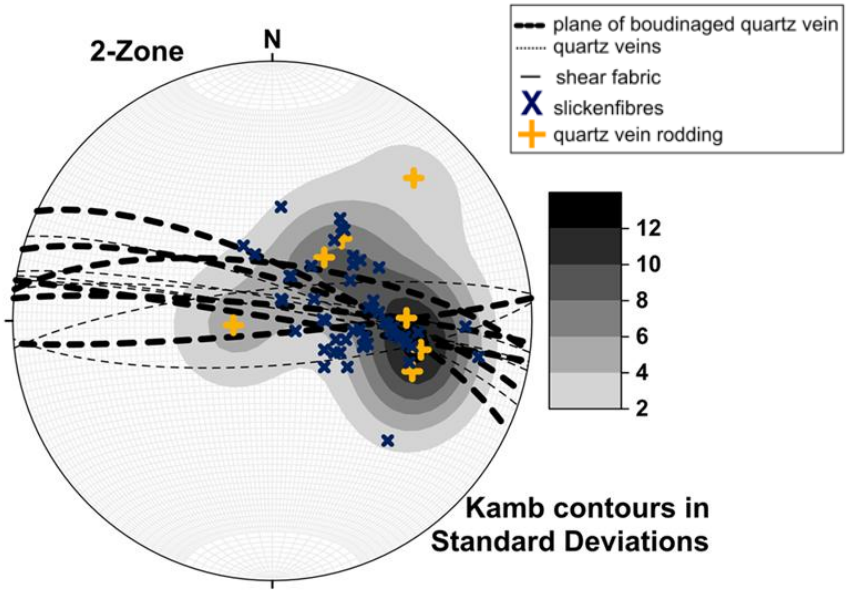

Fig. 4.19: 2-Zone measurements plotted on an equal area stereonet projection of various domains of structurally significant planes and lineations.

Both dextral and sinistral kinematics are observed at the surface; however, dextral appears to be the dominant shear sense (Fig. 4.19). The 2-Zone is an anastomosing shear zone with evidence of rheologically heterogeneous rocks exemplified at or near the contact between the mine diorite and basalt (Fig. 4.20).

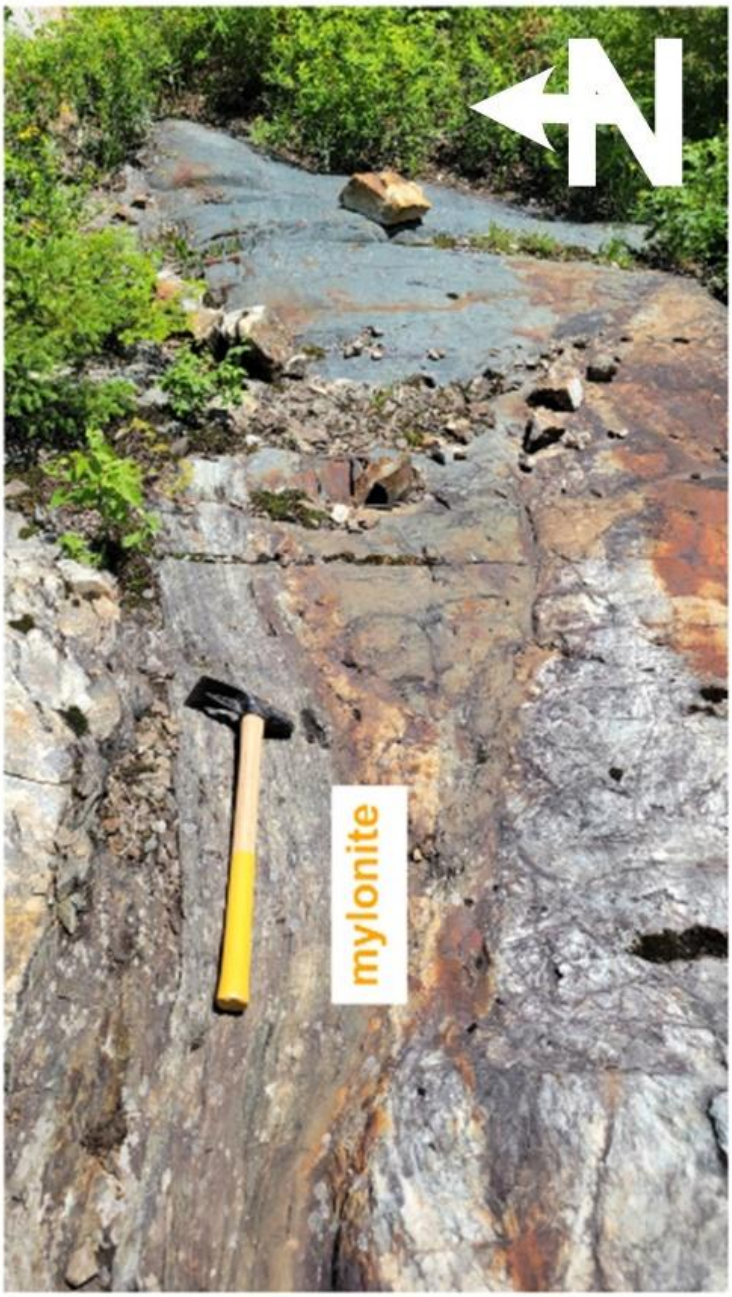

Fig. 4.20: Field image of the anastomosing 2-Zone contact with mylonite at margins, between tholeiitic basalt and Mine diorite.

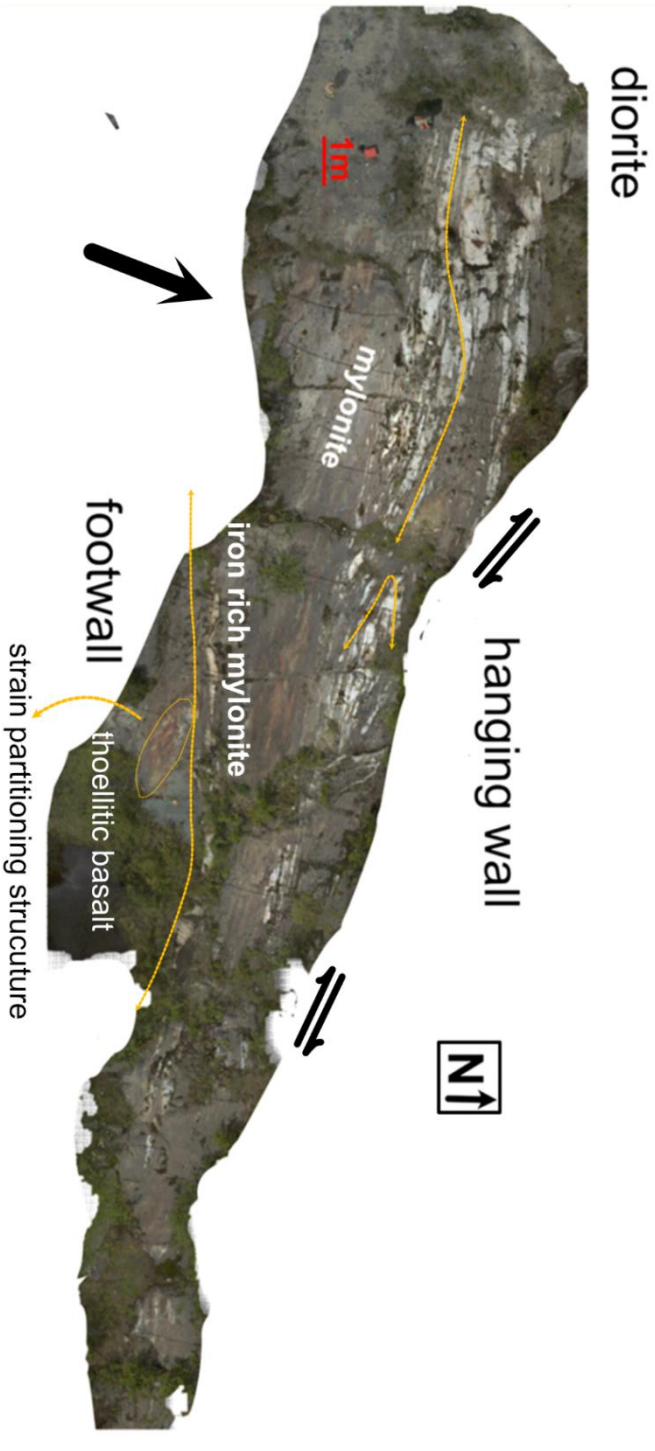

Fig. 4.21: Drone image of gold-bearing 2-Zone at 30m altitude.

8-Zone Sheared Quartz Veins

The 8-Zone is located on the western side of the mine diorite pluton, near but not on a felsic volcanic rock contact (Fig. 4.1). The surface exposure measures 100 meters in length by 10 meters in width, and the host rock is quartz diorite. The shear zone fabric is interpreted to be medium-grade mylonite. The outcrop has iron-rich mafic dykes running parallel to the southern shear zone boundary (Fig. 4.22). Historically, the 8-Zone quartz veins have averaged 10 g/t and have been mined extensively in the subsurface (SRK report, 2022). Quartz veins range from veinlets to thirty centimeters by fifty meters long. Most veins include pyrite, pyrrhotite and chalcopyrite at vein margins. Chlorite, epidote and clinozoisite define the vein selvage. Veins in the 8 Zone have been isoclinally folded, with limbs parallel to foliation.

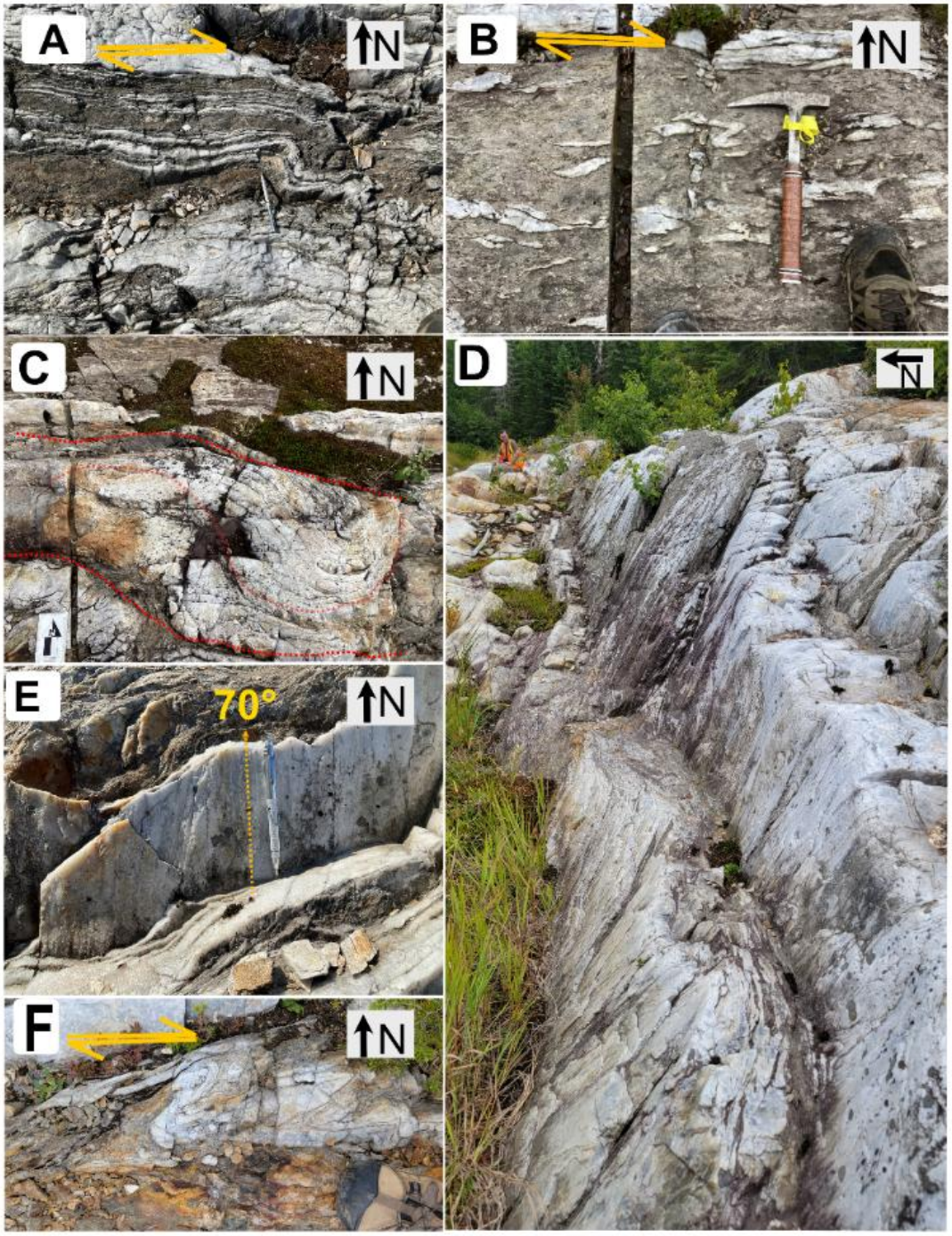

Fig. 4.22: Quartz veins and structures from the 8-Zone outcrop; A: Z folds with quartz veinlets; B: Z fold occurrence in boudinaged veinlet. C: S fold in large 1-meter folded quartz veins. D: primary structure quartz veining in the 8 Zone. E: well-defined quartz rodding; F: well-pronounced Z fold, nearly a recumbent fold.

Crenulation cleavage was observed throughout the outcrop, along with boudinaged, pinch and swell quartz vein textures and Z-folds (in veinlets and foliations) between each large quartz vein occurrence as a secondary structure (Fig. 4.23). The mean orientation of the 8-Zone is 270°/70°NE with a plunge and trend of 68°→350° (Fig. 4.24). A strongly pronounced stretching lineation, oblique to the shear axis plane, is prevalent throughout the outcrop, expressed in quartz veins (Fig. 4.23).

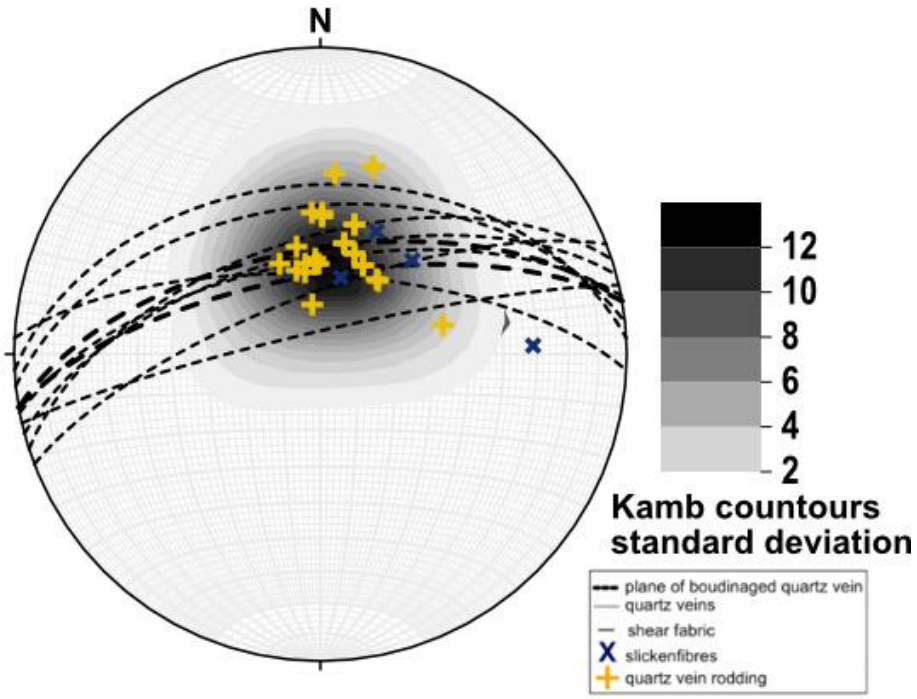

Fig. 4.23: An equal area stereonet projection of planes and lineations from the 8 Zone outcrop.

Stereonet analysis and field observation show that the 8-Zone dominant shear sense is a high-angle north-over-south reverse shear, accompanied by a very minor dextral component. The 8-Zone outcrop has less horizontal movement when compared to the 2-Zone outcrop, and no strain partitioning structure was observed.

Fig. 4.23 – Drone image of 8-Zone outcrop taken at an elevation of 30 meters.

4.2 Lithogeochemistry

4.2.1 Overview

Fifty-two Eagle River mine and area field samples were collected for geochemical analysis. The sample suite includes mafic rocks (n=16) consisting of basalt, basaltic andesite, gabbro and sub-alkaline basalt. Intermediate rocks (n=19) consist of andesite, gabbroic diorite, granodiorite, and a felsic suite (n=4) comprising granite and three intermediate granodiorite samples. Sm/Nd isotope analysis was performed on twelve samples to investigate the influence of crustal contamination and help us better understand the Eagle River's tectonic setting. All Sm/Nd and lithogeochemistry data can be found in Appendix A.

4.2.2 Major & Trace Element Geochemistry

Conventional major element plots can be problematic, particularly when dealing with Archean rocks that have undergone extensive alteration, metasomatism, metamorphism, and multiple localized or regional deformation events (Pearce, 1996). However, primary element analysis can be helpful. TiO_2 is considered relatively immobile during mantle melting and fractional crystallization of primary magmas (Hoare et al., 2020). Titanium is compatible during fractional crystallization of intermediate to felsic magma due to partitioning into early forming minerals, such as ilmenite and magnetite, with depleted titanium in residual melts. The behavior of TiO_2 is shown for each rock type in variation diagrams to evaluate the elemental mobility of major element oxides in felsic, intermediate, and mafic samples of the Eagle River mine and area field samples in Figure 4.24.

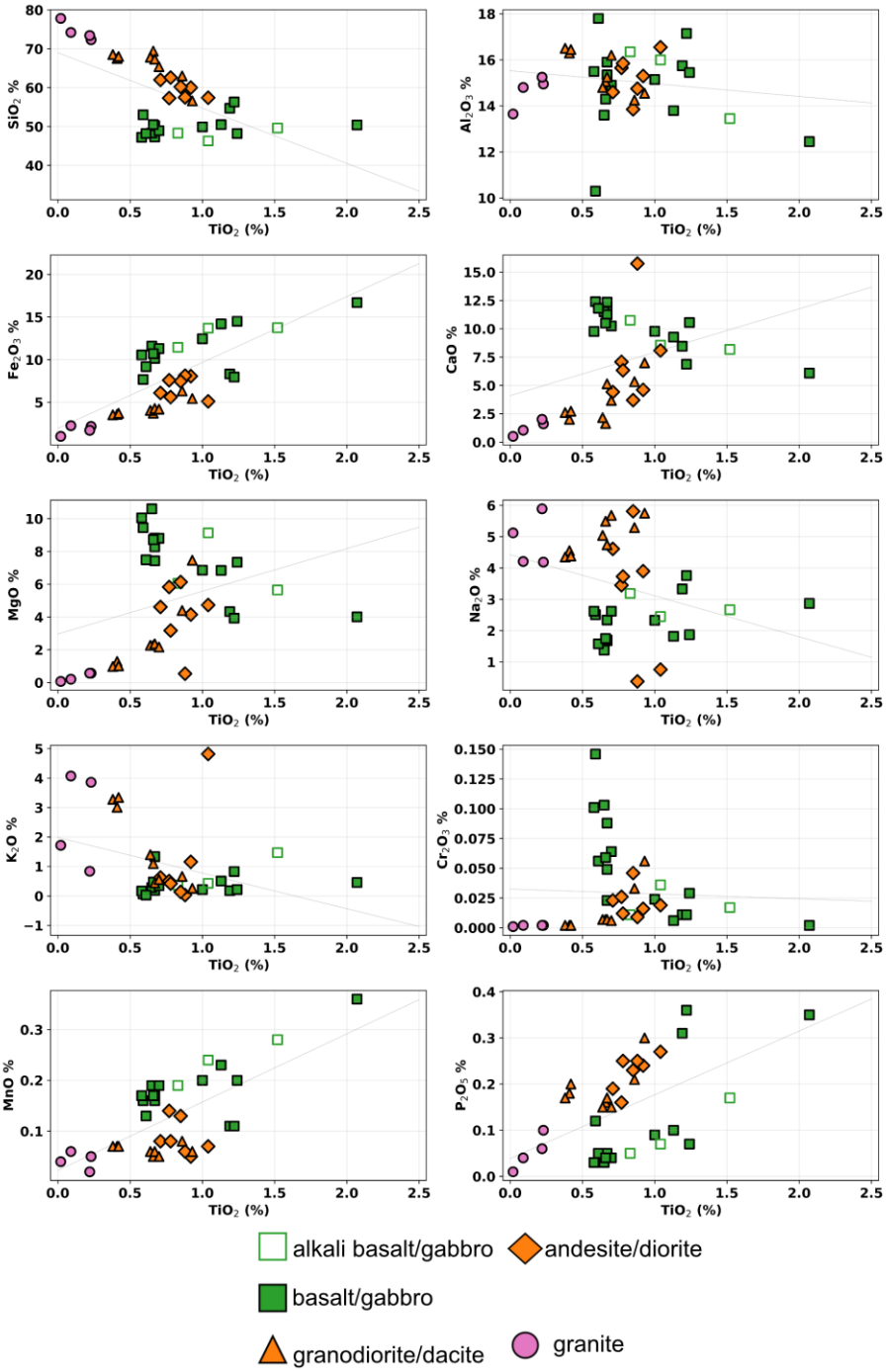

Figure 4.24: XY plots, with oxide (%) vs TiO_2 showing various trends in felsic, intermediate, and mafic rock samples.

The Eagle River TiO_2 centered XY plots show a clear magmatic differentiation trend from Ti-Fe-Mg-Ca rich mafic sample suite to a Si-K rich felsic samples. SiO_2 declines systematically as TiO_2 increases with the granites having the highest SiO_2 and very low TiO_2

content whereas the mafic rocks carry the highest TiO_2 and lowest SiO_2, reflecting a greater proportion of mafic minerals (pyroxene/amphiboles). Cr_2O_3 is elevated in most mafic samples consistent with its compatibility in early mafic phases and P_2O_5 content rises in the intermediate compositions before scattering, consistent with apatite control.

Trace element discrimination plots are helpful when deciphering the protolith of a highly altered or metamorphosed rock (Winchester & Floyd, 1977). A plot for distinguishing the original lithology, post-metamorphism and alteration is Winchester and Floyd (1977) using REE ratios Zr/TiO_2 vs Nb/Y (Fig. 4.25).

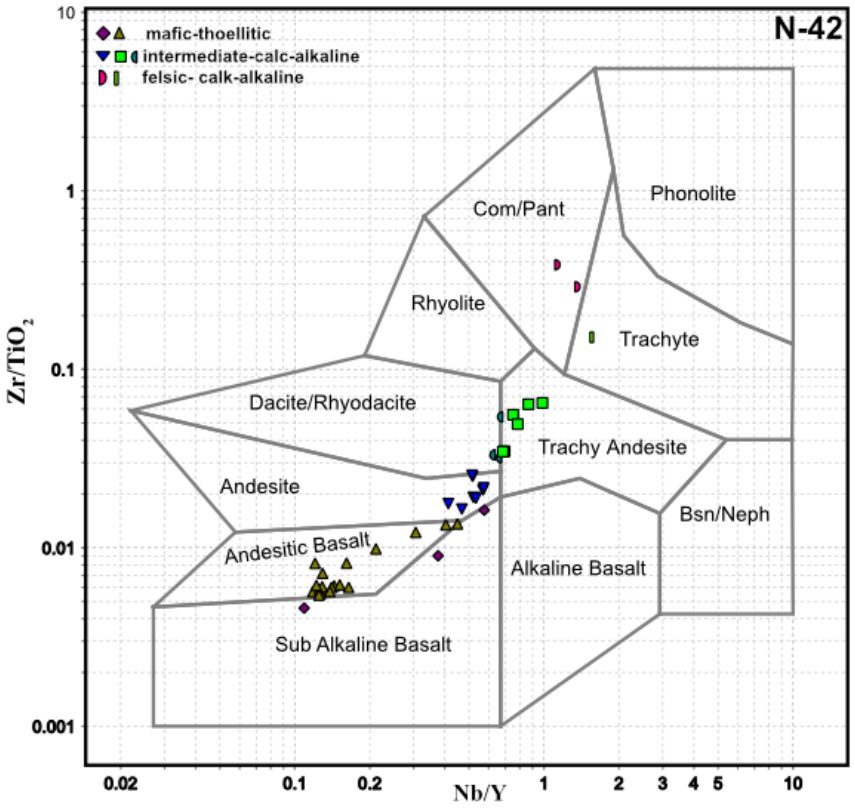

Figure 4.25: Plots modified from Winchester & Floyd (1977), highlighting the original magma series at the Eagle River Mine and nearby area.

Figure 4.25 shows the range of magmas at Eagle River. Mafic samples comprise basaltic andesite, sub-alkaline basalt, and intrusive equivalent gabbro. Intermediate samples plot as andesite, and the intrusive equivalent is diorite and/or diorite granodiorite. Felsic samples are the intrusive equivalents of trachyandesite, granite and or granodiorites. Calc-alkaline and tholeiitic magmas have distinct characteristics and are helpful for understanding an area's tectonic environment. Based on the work of Ross and Bedard (2014), using REE ratios Th/Y vs Zr/Y, we characterized each field sample's magmatic affinity (Fig 4.26).

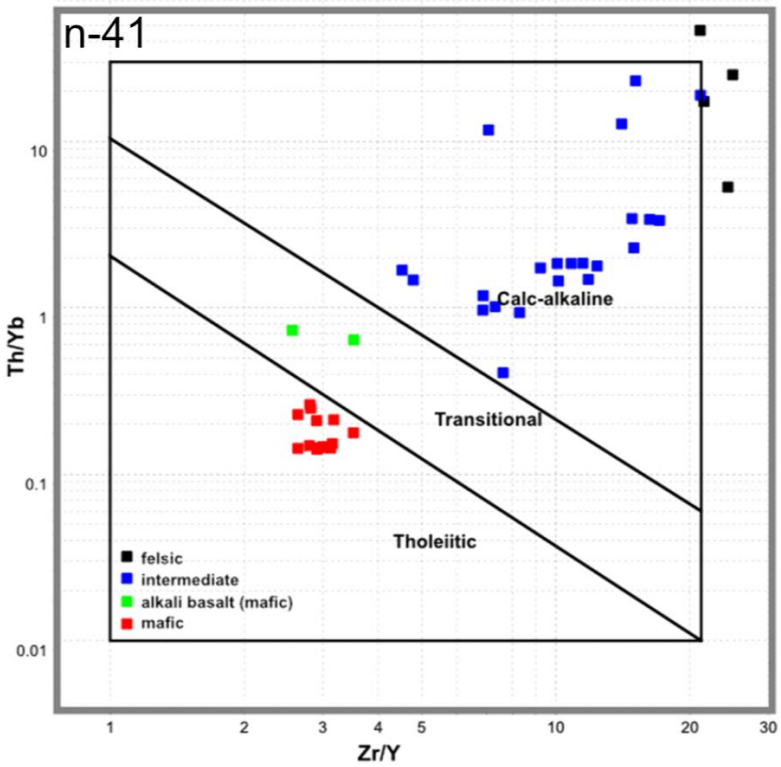

Fig. 4.26: A modified plot based on the work of Ross and Bedard (2014), highlighting the Eagle River rock samples' magmatic affinity.

Figure 4.27 shows the magmatic affinity of each lithology at and nearby the Eagle River mine.

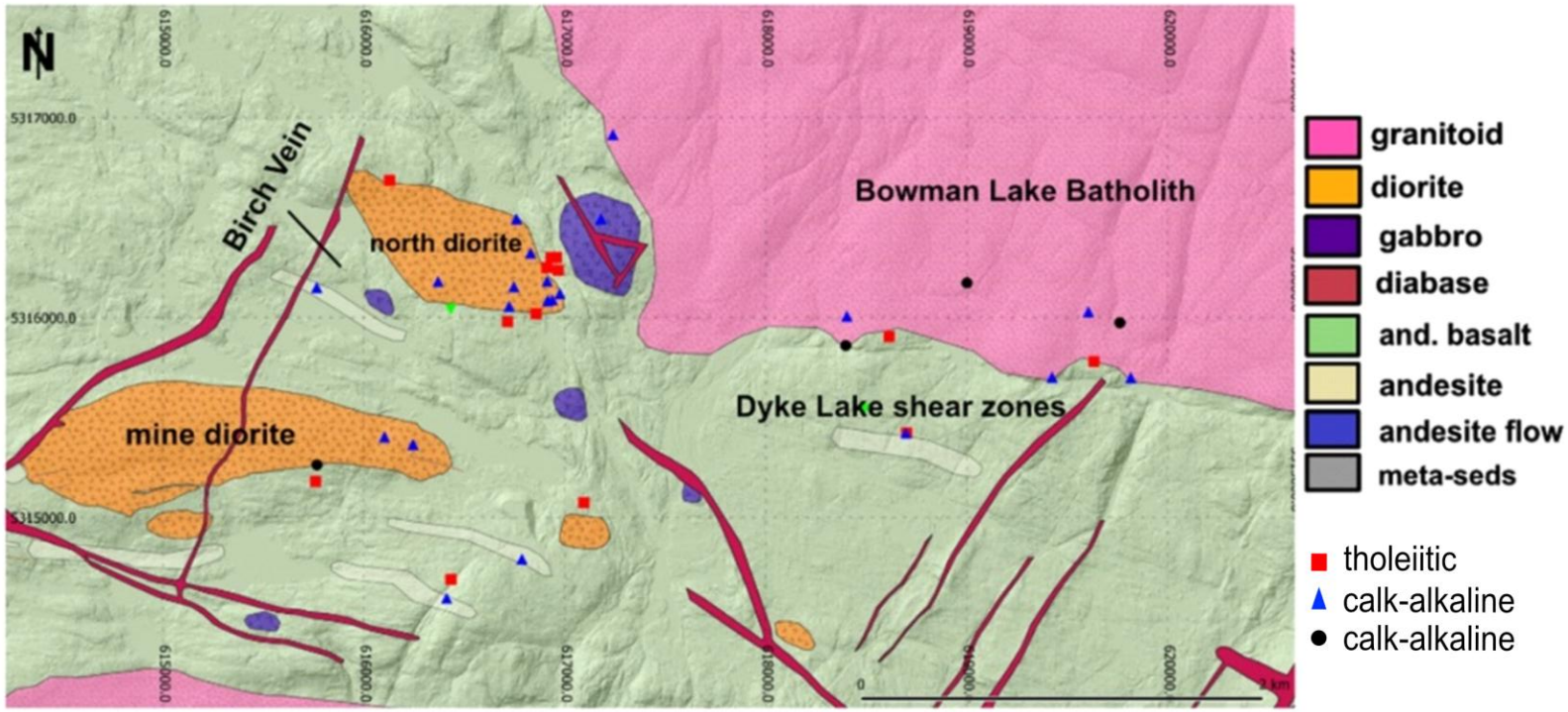

Fig. 4.27: Geological map of Eagle River area showing sample locations and the magma affinity of each sample.

The Eagle River mafic samples, including basalt, basaltic andesite, sub-alkali basalt, and gabbro, plot within the tholeiitic field of Figure 4.26 and are characterized by 47-53 wt.% SiO_2 and 4.01-10.05 wt.% MgO, 7.7-16.7 wt.% Fe_2O_3, 10.30-17.80 wt.% Al_2O_3, 0.6-2.9 wt.% TiO_2, and 7.5–11.6 wt.% CaO. Two groups with no spatial correlation have been identified in the mafic sample suite (Fig. 4.28); group A has a negative Nb anomaly (Nb/Nb* = 0.59-0.68), near flat to weakly enriched light rare earth content (LREE) with La/Sm_{pm} of 0.94-1.25 and HREE values that are flat to very weakly fractionated with a ratio of Gd/Yb_{pm} of 1.3 to 1.58. Group B has a negative Nb anomaly, Nb/Nb* 0.56-0.83, weakly enriched LREE with La/Sm_{pm} =0.90-1.48 and flat to weakly fractionated heavy rare earth elements (Gd/Yb_{pm} = 0.88 to 1.62; Fig. 4.28).

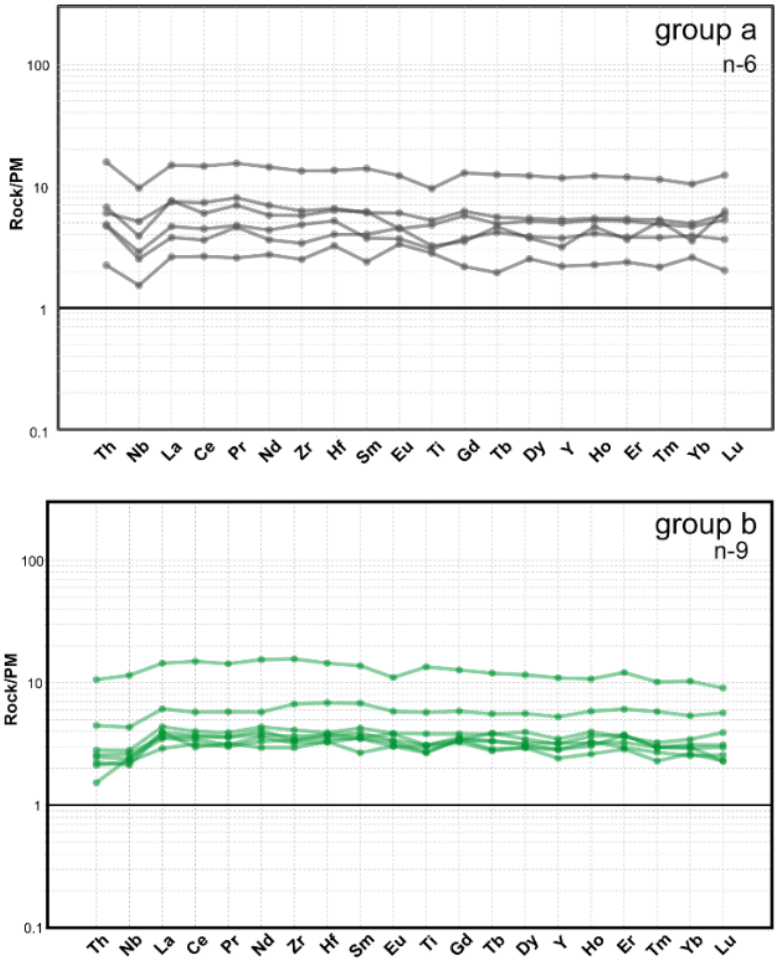

Fig. 4.28: Shows two groups within the mafic sample suite. Both groups have weak to no LREE enrichment and flat HREE signatures. Normalizing values from Sun & McDonough (1989).

Andesites, diorites and gabbroic diorites represent the Eagle River intermediate sample suite. The granitoid and three granodiorite samples in the intermediate suite are plotted with the granite samples. The granodiorites have higher amounts of plagioclase than potassium feldspar, so they are technically intermediate in composition. All intermediate samples plot in the calc-alkaline field of Figure 4.30 and are characterized by 50-69.4 wt.% SiO_2, 0.98-9.45 wt.% MgO and comprise two distinct groups observed in the sample suite. Type one has a positive Zr/Hf anomaly, and type two has a negative Zr/Hf anomaly (Fig. 4.8). Type one has negative niobium and negative titanium anomalies (Nb/Nb* = 0.02-0.37; Ti/Ti* = 0.43-0.85), negative to positive zirconium anomalies (Zr/Zr* = 0.88-1.71), and negative to positive hafnium anomalies (HF/Hf*= 0.78-1.59). Type 1 intermediate samples are flat to depleted in LREE (La/Sm_{pm} = 2.17-4.01) and have moderately fractionated HREE (Gd/Yb_{pm} = 0.91-3.74). The type two suite has negative niobium and negative titanium anomalies (Nb/Nb*=0.02-0.71), (Ti/Ti*=0.39- 0.81), and negative to positive zirconium anomalies (Zr/Zr*=0.86-1.27) and negative to positive hafnium anomalies (HF/Hf*=0.72- 1.03). Spider diagrams suggest the type two intermediates are flat to depleted in (LREE La/Sm_{pm}=1.29-5.82) and moderately fractionated HREE (Gd/Yb_{pm}=0.70-4.28; Fig.4.29).

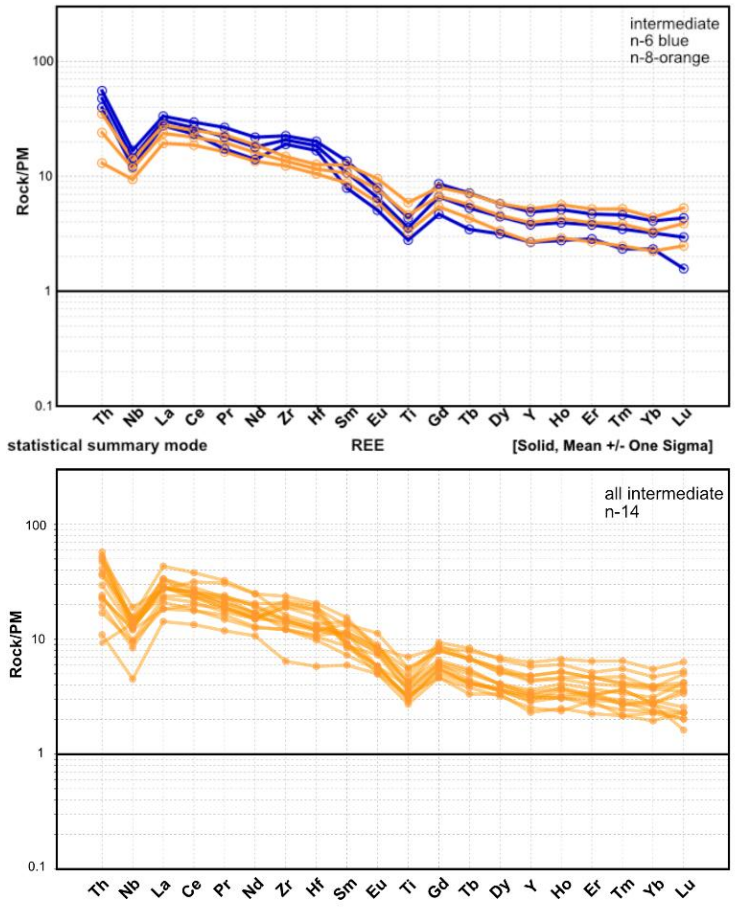

Fig.4.29: Intermediate rocks type one in blue and type two in orange. All intermediate samples are plotted below in orange, showing a strong negative niobium and titanium anomaly, a weak depletion in REE and moderately fractionated HREE. Normalizing values from Sun and McDonough (1989).

The felsic sample suite consists of granite (3) and intermediate granodiorite (5) samples that are at the boundary between intermediate and felsic from the Bowman Lake batholith and plotted as calc-alkaline magmatic affinity characterized by 67-74 wt.% SiO_2, 0.21-1.29 wt.% MgO. The suite has a negative Nb (Nb/Nb*=0.10-0.31) and Ti anomaly (Ti/Ti*=0.03-0.24). Enriched light rare earth element content (LREE) with La/Sm_{pm} ratios of 4.76-6.28 and strongly fractionated HREE ratio Gd/Yb_{pm}=2.71-5.33 (Fig. 4.30).

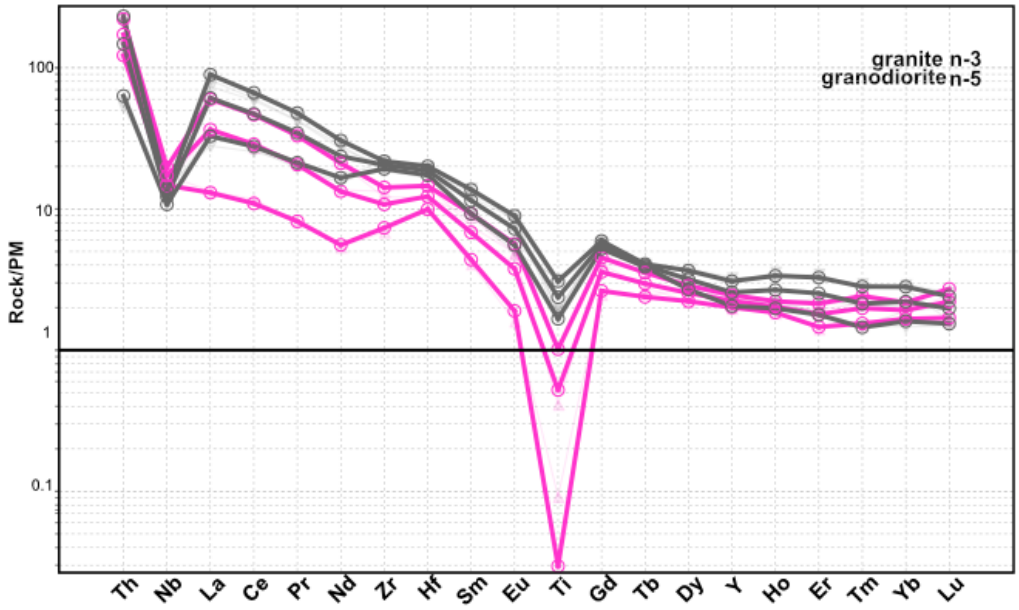

Fig.4.30: Granite (pink) and granodiorite (grey), showing a strong enrichment of LREE, negative Nb and Ti anomalies, and a fractionated HREE pattern. Normalizing values from Sun and McDonough (1989).

4.2.3 Eagle River Diorite

Analysis of the North diorite pluton field samples and Wawrzonkowski (2024) drill hole samples from the 8-Zone mine diorite drill core were analyzed for any potential correlation, given the importance of finding a brittle intrusive body nearby with similar lithology to the Eagle River mine host rock. The Mine Diorites and Northern Diorite samples have similar REE signatures, with similar Nb and Ti anomalies, moderate depletions in LREE, and moderately fractionated HREE (Fig. 4.31).

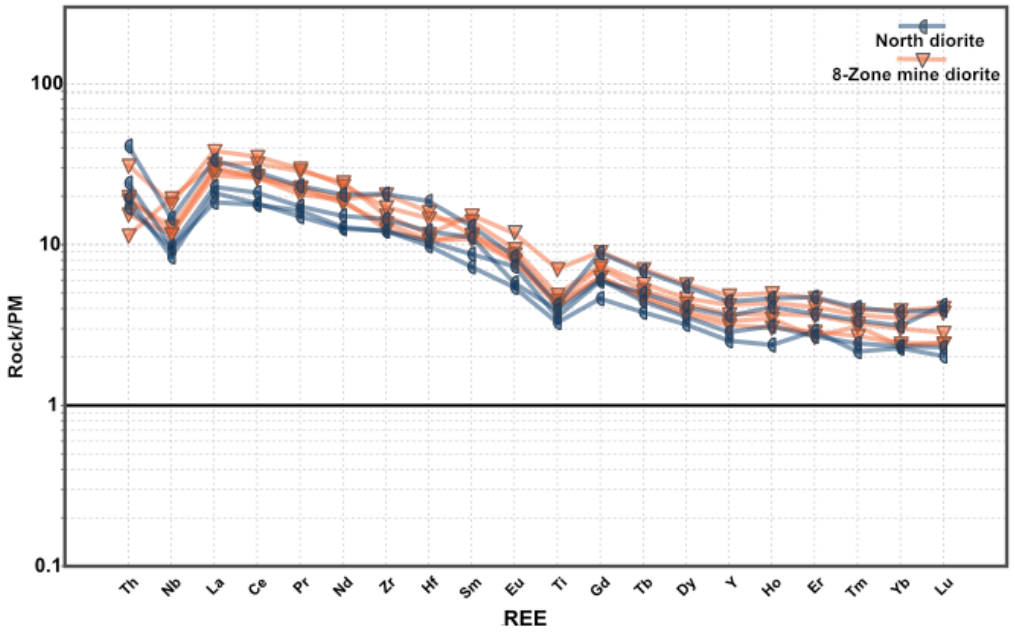

Fig. 4.31: Primitive mantle normalized diagrams for the North diorite and 8-zone mine diorite. Normalizing values from Sun and McDonough (1989)

4.2.4 Sm/Nd Isotope Analysis

For this study, we selected twelve field samples for Sm-Nd analysis to better understand the crustal evolution of the rocks at Eagle River mine and the nearby area. Ten samples were successful. Figure 4.32 shows sample locations. We assumed a Sm/Nd depleted mantle of $\varepsilon Nd_{T(2700)}$ of (+3), based on early Earth dynamics (Huston and Gutzmer, 2023).

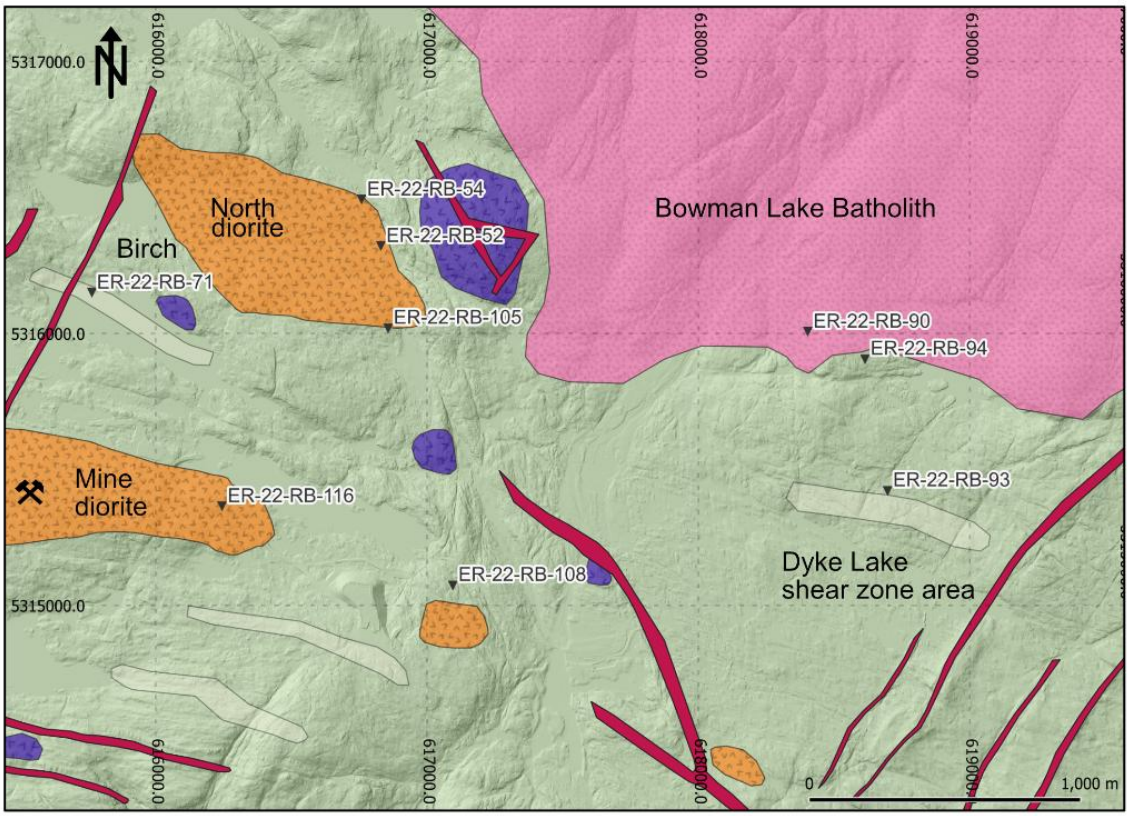

Figure 4.32: Geological map of Eagle River mine and area with Sm-Nd isotope sample locations

The εNd results yielded positive values for all samples, assuming an age of 2700 Ga (Neoarchean), and consequently showed little correlation within this representative sample suite (Fig. 4.33; Table 4.1). The overall range of $\varepsilon Nd_{T(2700)}$ values is (1.39 to 2.50). The mafic sample suite, comprising tholeiitic basaltic andesite (x2) and transitional sub-alkaline basalt, yielded a range of $\varepsilon Nd_{T(2700)}$ values from (1.93 to 2.50). The intermediate sample suite, comprising diorite, granodiorite, andesite flow, and gabbroic diorite, yielded a range of $\varepsilon Nd_{T(2700)}$ values of (2.10-2.42). The felsic suite, comprised of granite and granodiorite, yielded a range of $\varepsilon Nd_{T(2700)}$ values of (1.53-2.56).

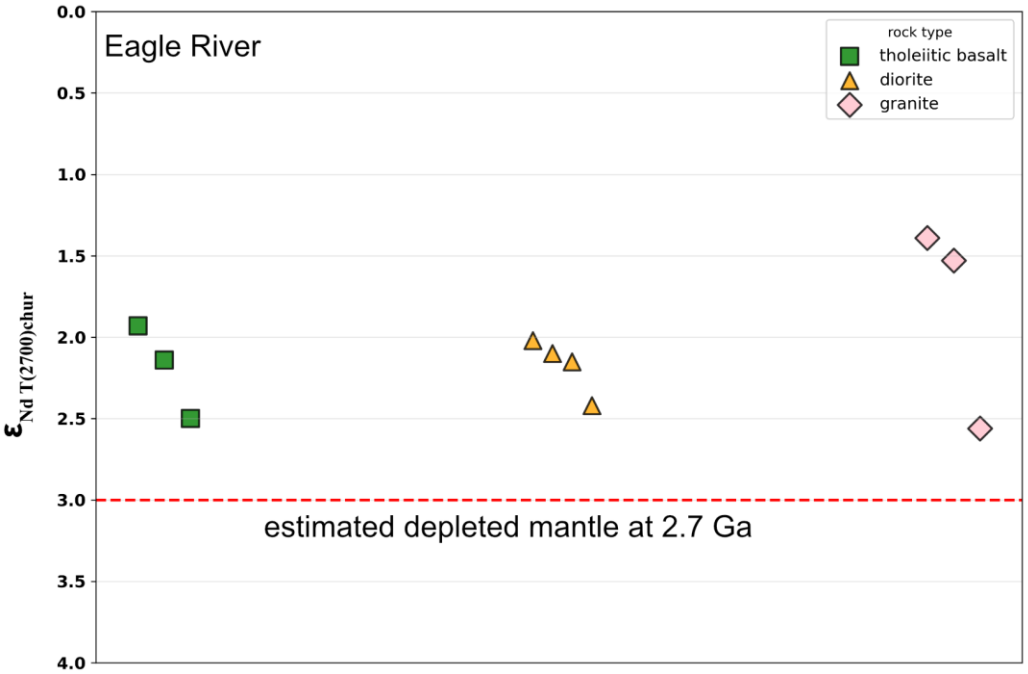

Fig. 4.33: Graphical representation of the Eagle River $\varepsilon Nd_{T(2700)}$ *values.*

Table 4.1: Eagle River Sm/Nd isotope data compilation

Sample	Nd (ppm)	Sm (ppm)	$^{147}Sm/^{144}Nd$	$^{143}Nd/^{144}Nd$	2σ	Epsilon(0)	^{144}Nd	(T) De Paolo	TDM2	$\varepsilon_{Nd\ T(2700)chur}$
ER-105	4.33	1.35	0.1877	0.512620	7	-0.4	12.200356	2514	3097	2.501912822
ER-94	8.55	2.62	0.1855	0.512544	5	-1.8	12.1985472	2766	3262	2.14144489
ER-108	3.61	1.13	0.1883	0.512604	5	-0.7	12.1999752	2699	3265	1.925295125
ER-52	20.48	3.88	0.1146	0.511252	7	-27.0	12.1677976	2778	2904	1.52920883
ER-90	22.69	3.29	0.0875	0.510766	7	-36.5	12.1562308	2769	2864	1.390602416
ER-99	35.59	4.97	0.0843	0.510768	7	-36.5	12.1562784	2697	2791	2.561792051
ER-116	23.07	4.67	0.1222	0.511421	7	-23.7	12.1718198	2725	2865	2.102450618
ER-54	16.49	3.26	0.1195	0.511366	6	-24.8	12.1705108	2736	2872	2.023676836
ER-71	29.85	5.54	0.1121	0.511242	8	-27.2	12.1675596	2722	2848	2.149061192
ER-93	13.90	2.87	0.1247	0.511481	10	-22.6	12.1732478	2696	2844	2.424127782

4.2.5 U-Pb Geochronology

Geochronology sample ER-RB-23-120 was the second attempt at U-Pb age dating from the Eagle River, Northern Diorite Pluton; the first sample yielded an insufficient number of required zircons for an accurate age date. The second attempt was successful and yielded a weighted mean age of $^{207}Pb/^{206}Pb$ age = 2720.60 ± 0.15 [2.33] Ma (2s), MSWD = 0.94 (n=6; Fig. 4.34, Table 4.2). The sample was retrieved from the relatively undeformed area of the Northeastern portion of the Northern Diorite pluton and consisted of a porphyritic texture, 3-4mm plagioclase grains, 2-3mm orthoclase grains, with lesser amounts of quartz, biotite and hornblende and very minor chlorite alteration staining.

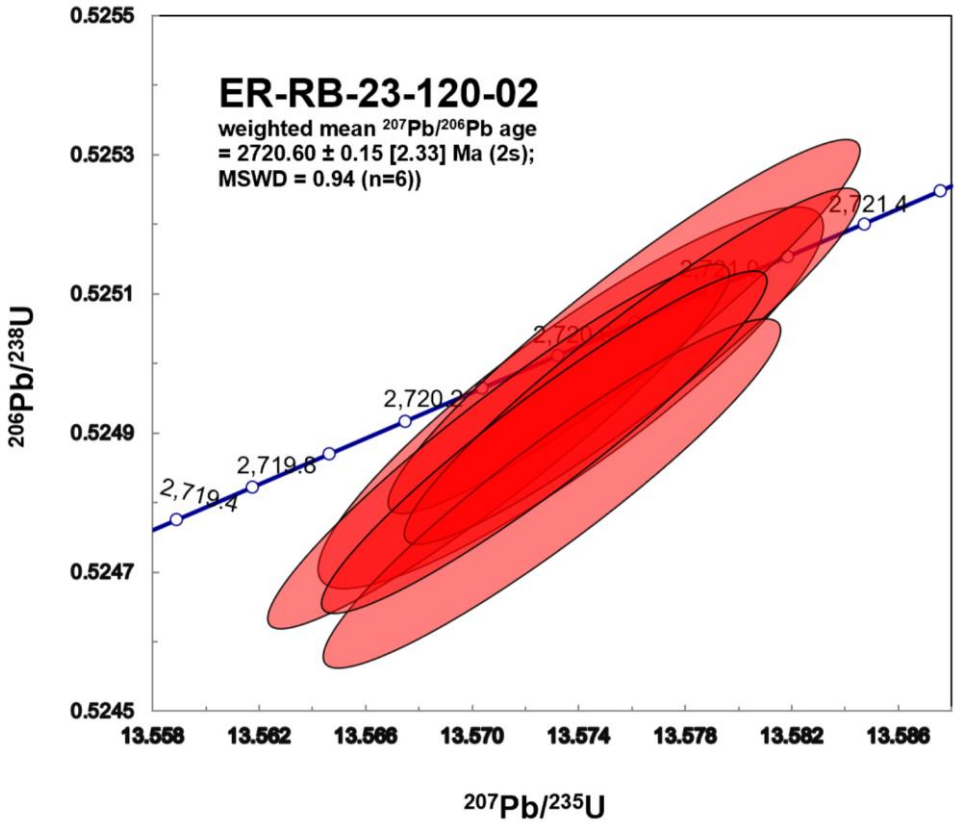

Fig. 4.34: Concordia plot highlighting dated zircon grains (n-6) for the Northern Diorite U-Pb age geochronology sample.

Table 4.2: U-Pb Isotope Data

CA-TIMS U-Pb isotopic data

			Compositional Parameters					Radiogenic Isotope Ratios									Isotopic Ages					
Sample	Detection mode	Th/U	$^{206}Pb^*$ x10^{-13} mo	mol % $^{206}Pb^*$	Pb^*/Pb_c	Pb_c (pg)	$^{206}Pb/^{204}Pb$	$^{208}Pb/^{206}Pb$	$^{207}Pb/^{206}Pb$	% err	$^{207}Pb/^{235}U$	% err	$^{206}Pb/^{238}U$	% err	corr. coef.	$^{207}Pb/^{206}Pb$	±	$^{207}Pb/^{235}U$	±	$^{206}Pb/^{238}U$	±
(a)	(b)	(b)	(c)	(c)	(c)	(c)	(d)	(e)	(e)	(f)	(e)	(f)	(e)	(f)		(g)	(f)	(g)	(f)	(g)	(f)
ER-RB-23-120-02																					
1-13	F (Pb) F (U)	0.767	5.9495	99.94%	595	0.29	30867	0.212	0.18759	0.020	13.570863	0.054	0.524914	0.041	0.944	**2720.4**	**0.34**	2720.24	0.51	2719.99	0.91
1-15	F (Pb) F (U)	1.180	2.6687	99.88%	310	0.27	14888	0.326	0.18764	0.022	13.572927	0.053	0.524845	0.040	0.935	**2720.9**	**0.36**	2720.38	0.51	2719.70	0.88
1-16	F (Pb) F (U)	0.674	4.1608	99.91%	392	0.30	20720	0.186	0.18760	0.021	13.575721	0.055	0.525089	0.042	0.942	**2720.5**	**0.34**	2720.57	0.52	2720.73	0.94
1-18	F (Pb) F (U)	0.600	1.1105	99.74%	130	0.24	6968	0.166	0.18760	0.028	13.573642	0.059	0.524985	0.043	0.898	**2720.5**	**0.46**	2720.43	0.56	2720.29	0.96
1-19	F (Pb) F (U)	0.657	16.6418	99.97%	1031	0.46	54670	0.182	0.18762	0.020	13.576032	0.053	0.525031	0.040	0.942	**2720.7**	**0.34**	2720.60	0.50	2720.48	0.89
2-19	F (Pb) F (U)	0.688	7.8552	99.95%	756	0.30	39846	0.190	0.18761	0.020	13.572625	0.052	0.524920	0.039	0.942	**2720.6**	**0.33**	2720.36	0.49	2720.01	0.86

weighted mean $^{207}Pb/^{206}Pb$ age = 2720.60 ± 0.15 [2.33] Ma (2s); MSWD = 0.94 (n=6)

4.3 Petrography

This section characterizes the petrography of each representative lithological group from the Eagle River Mine and area. An overview of mafic, intermediate and felsic lithologies will be summarized here. Rocks are of greenschist facies with localized occurrences of lower amphibolite facies. Primary minerals are only rarely preserved with secondary epidote, clinozoisite, zoisite, chlorite, actinolite, tremolite, calcite, and siderite being the dominant assemblage (Fig. 4.35). Appendix B documents all thin section descriptions.

4.3.1 Mafic Petrography

Mafic lithologies at Eagle River include tholeiitic basalt, basaltic andesite and gabbro. Tholeiitic basalt is characterized by an aphanitic texture with a very fine-grained groundmass with subhedral bytownite (45%) up to 0.30 mm; however, it is generally very fine-grained within the groundmass. Subhedral hornblende and actinolite (15%) up to 0.2 mm, and clinopyroxene (10%) are both euhedral to subhedral with a grain size of up to 0.2 mm; phyllosilicates, biotite and chlorite occur as subhedral laths up to 0.25 mm (18%). Trace minerals sphene, magnetite, and ilmenite are disseminated throughout the groundmass. Alteration minerology is typical of greenschist facies; chlorite pervasively alters biotite laths and hornblende and retrogresses to actinolite. Clinopyroxene replaces olivine grains, while relic olivine grains are commonly observed in tholeiitic basalt and gabbro. Epidote, clinozoisite and zoisite are relatively common throughout the groundmass (Fig. 4.35a).

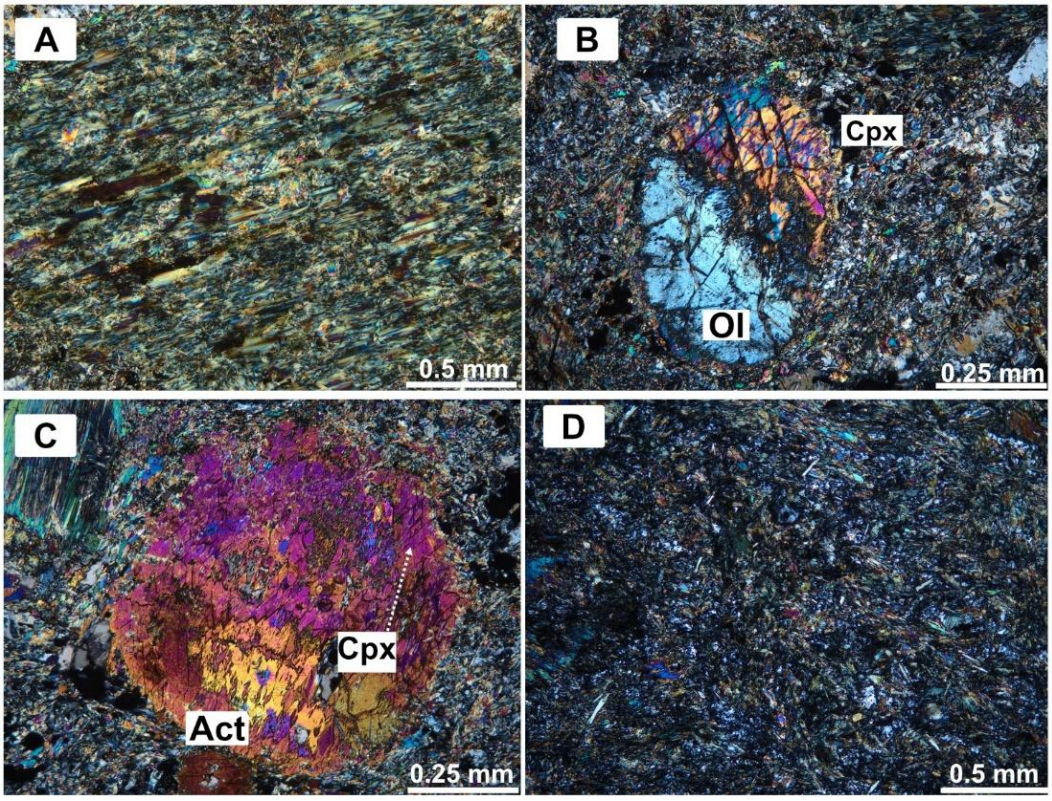

Fig. 4.35: XPL photomicrograph of tholeiitic basalt sample ER-22-39, A: Tholeiitic basalt, foliated with chlorite-biotite-amphibole-clinozoisite groundmass, with fine-grained CPX. B: Gabbro with a grain of olivine half replaced by CPX in a fine-grained matrix. C: A relic olivine grain, replaced with CPX, and overprinted by actinolite. D: Basaltic andesite with a fine-grained groundmass comprised of actinolite, hornblende, clinozoisite, epidote, biotite and plagioclase.

The dominant lithology at Eagle River is basaltic andesite, characterized by a very fine-grained groundmass comprised of plagioclase (anorthosite 40%), fine-grained quartz (3%), hornblende (10%), actinolite (5%), biotite/chlorite (20%), clinopyroxene and olivine (5%). Plagioclase (anorthosite) is the most common mineral, with occurrences ranging from <0 0.1mm to 1.5 mm. The gabbros share many attributes with the basaltic andesite (Fig. 4.35c).

4.3.2 Intermediate Petrography

Intermediate lithologies at the Eagle River mine include andesite, diorite and granodiorite. The dominant mineral is plagioclase feldspar occurring in the groundmass up to 0.1mm and as subhedral to euhedral andesine porphyroblasts up to 4mm that exhibit Carlsbad twinning. Orthoclase, with pervasive sericite overprinting, is present in porphyroblasts up to 3mm. Together, plagioclase feldspars make up 65% of the total sample. Quartz grains are subhedral, very fine-grained, and present mostly in groundmass (10-20%). Hornblende grains are subhedral and patchy, up to 1mm in size, constituting up to 15% of the modal percent. Very little biotite is present in the andesite thin section samples. Clinopyroxene is the dominant pyroxene (5%); grains are subhedral and up to 0.1mm. Less than 1% of orthopyroxene is observed with subhedral grains up to 0.1 mm in size. Alteration minerology is characterized by subhedral epidote with minor amounts of chlorite-altering hornblende and what little biotite is present. Trace magnetite, ilmenite and titanite are also present.

The Mine Diorite and Northern Diorite intrusions represent the Eagle River diorite suite of samples and share many similarities. Plagioclase feldspar is the dominant mineral (up to 45 % in thin section), comprised of albite and andesine. Polysynthetic twinning is commonly observed in albite porphyroblasts and carlsbad twinning in andesine; grain sizes are up to 2 mm, and plagioclase in the matrix is fine-grained up to 0.1mm (Fig. 4.40). Orthoclase is present (5%) with grains up to 2 mm and is pervasively overprinted with sericite (5%). Quartz varies from 5-20% and mostly occurs within the groundmass. Grains are generally subhedral and are characterized by small lobes. Hornblende is present with grain sizes up to 1mm (10-15%). Euhedral to subhedral biotite laths are present and up to 1.5 mm in some samples, with alteration halos

around inclusions of zircons. Clinopyroxene is observed in subhedral grains up to 0.2 mm (Fig. 4.36).

Alteration minerology is characterized by chlorite replacing biotite and overprinting hornblende grains. Trace metals, including sphene, ilmenite and magnetite, are seen sparsely disseminated throughout the rock fabric. Calcite and siderite are common carbonates observed within the intermediate intrusions.

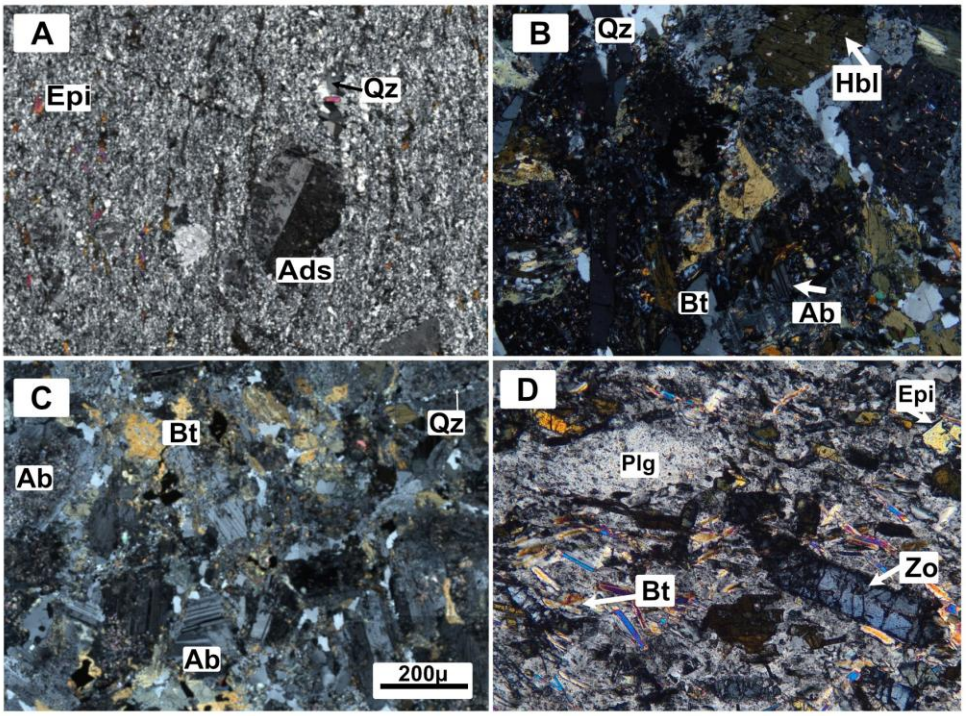

Fig. 4.36: Intermediate photomicrographs; A: Trachyandesite (XPL) with epidote (Epi), andesine (Ads) and very fine-grained quartz and plagioclase. B: North Diorite (XPL) with hornblende (Hbl), biotite (Bt) and albite overprinted with sericite. C: Mine Diorite (XPL) with biotite, hornblende and albite exhibiting polysynthetic twinning. D: North Diorite (XPL) with plagioclase (Plg), biotite (Bt) and zoisite (Zo).

4.3.3 Felsic Petrography

The felsic samples include granite from the tonalite-trondhjemite-granodiorite (TTG) suite, known as the Bowman Lake batholith; samples are porphyritic, relatively unaltered and crystals are randomly oriented (Fig. 4.37a). These samples are porphyritic, relatively unaltered, and massive. Quartz is the dominant mineral (30%), occurring as a groundmass up to 1 mm in size and observed in clusters with grains up to 200 μm in diameter. Larger grains exhibit undulose extinction. Feldspars are characterized by coarse-grained subhedral oligoclase up to 2.5 mm that exhibits polysynthetic twinning and coarse-grained subhedral, poikilitic orthoclase up to 3 mm. Feldspar grains are pervasively overprinted by sericite and fine-grained biotite; total feldspar content is 45%. Hornblende porphyroblasts up to 1.5 mm (10%) characterize amphiboles, with some very minor actinolite observed. Biotite (5%) and muscovite (2.5%) comprise the phyllosilicates; both are fine-grained, with a maximum grain size of 150 μm, and are euhedral to subhedral in shape. Alteration minerology is very sparse, with chlorite replacing hornblende and biotite (2%). Traces of subhedral epidote are present. Magnetite, ilmenite and pyrite occur sparsely disseminated throughout (Fig. 4.37)

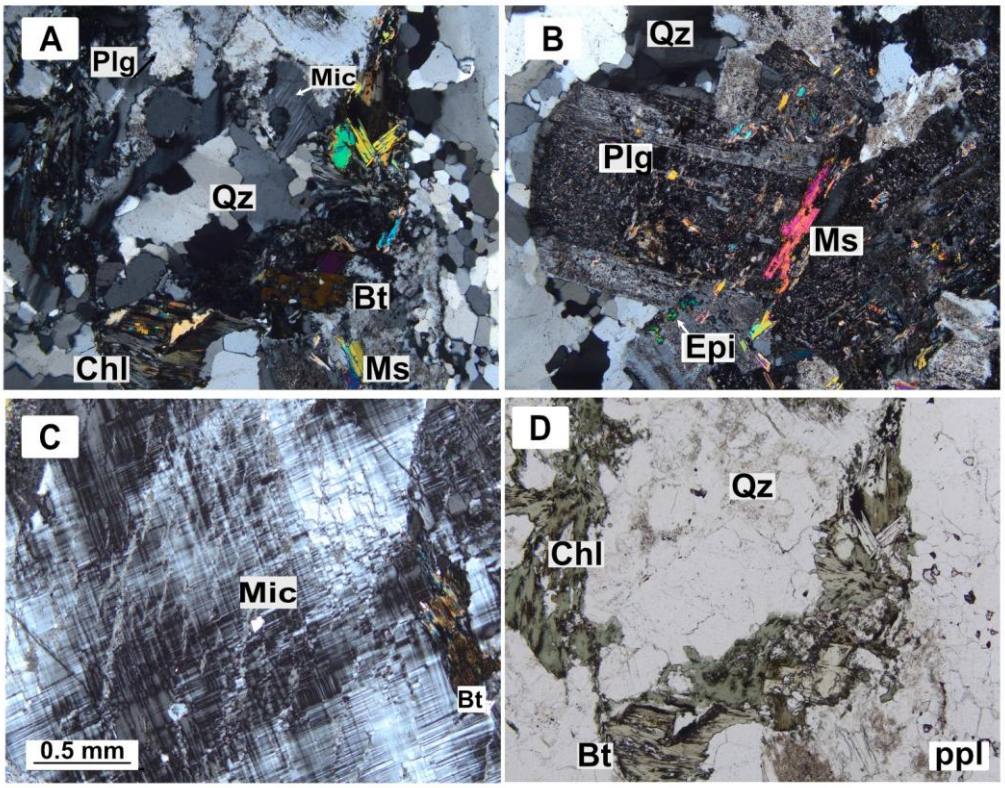

Fig. 4.37: Photomicrographs of the felsic sample suite; A: randomly orientated quartz (Qz), microcline (Mic), plagioclase from the Bowman batholith; B:(Pl (XPL), muscovite (Ms); C: large grain of microcline (4 mm) (XPL); D: image of chlorite (Chl) interacting with biotite (Bt) (PPL).

4.3.4 Mylonite Petrography

The Eagle River mine Au-bearing shear zones (2 & 8) are directly hosted in diorite that has been subjected to higher temperatures and strain and, therefore, texturally referred to as medium-grained mylonite (Trouw et al., 2009). The 2-Zone, due to the eastern extent of deformation hosted in tholeiitic basalt, has an increased sulphide content and has more mafic characteristics. The 8-Zone mylonite is classified as a medium-grained mylonite (diorite) and is characterized by plagioclase, quartz, amphiboles, biotite, muscovite and epidote, clinozoisite, zoisite, barite and trace amounts of apatite. Alteration minerals include clinozoisite, chlorite, albite, orthoclase, zeolite, siderite and calcite. The Eagle River shear zones microstructures

include winged δ porphyroclasts, φ and α porphyroclasts, multiple instances of strong S and C fabric orientations (C-type shear bands), mica fish and quartz aggregate sigmoids, asymmetrical micro folds, foliation deflections and asymmetrical sheared quartz boudins and are reviewed in the Au-bearing shear zone section.

Quartz is present in various domains, including aggregates of fine-grained quartz ribbons, shear bands and minor grains within the mylonite matrix. Quartz grains have been dynamically recrystallized, falling into the grain boundary migration regime category, with some bulging characteristics observed. Serrated grain boundaries, shape-preferred crystal orientation, island grains, and pinning microstructures were also observed (Fig. 4.38).

Plagioclase grains have not been recrystallized and are generally expressed as fractured porphyroclast networks, with larger grains dominantly showing antithetic shear fractures. Grains are overprinted by mica, and some orthoclase grains have been sericitized. Some relic twinning is observed in larger plagioclase grains (Fig. 4.38e). The plagioclase networks and the presence of porphyroclasts suggest that the 2-Zone and 8 Zone shear fabric should be classified as a medium-grade mylonite (Trouw et al., 2009).

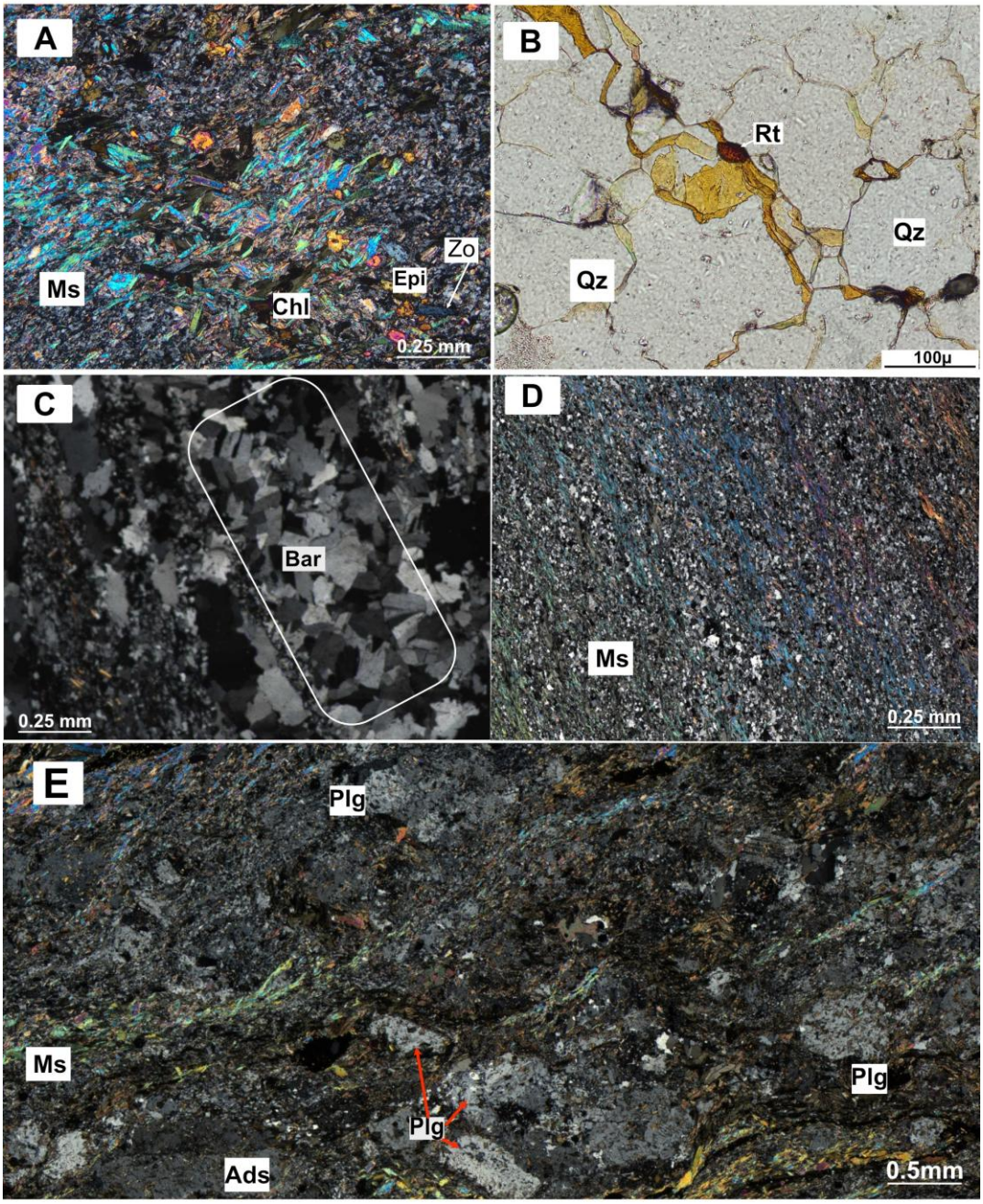

Fig. 4.38: Photomicrographs of mylonite in shear zones 2 & 8. A: Muscovite and biotite grains showing a strong preferred orientation with alteration minerals epidote (Epi), chlorite (Chl) and zoisite (Zo). B: photomicrograph of quartz grain boundaries infilled with rutile and hematite. C: 8-Zone sheared quartz vein with a barite (Bar) veinlet with a strongly pronounced crystal habit. D: muscovite (Ms) exhibiting preferred orientation. E: fractured plagioclase network with identifiable grain of andesine (Ads).

4.3.5 Mineralization

Gold was identified through reflected light petrography. Grains are up to 25 µm in size with no crystal habit recognized. They are preferentially located within quartz veinlets, at or close to vein selvage. Gold grains occurred with chlorite, biotite, muscovite, quartz, zoisite, calcite, siderite and, in one instance gold was observed to occur with galena, however, the occurrence was not common enough to infer paragenetic relationships . Barite and a large patch of midnight blue zoisite were identified within proximity to gold mineralization (100 µm), with a network of a translucent mineral that is comprised of titanite and hematite within grain boundaries of quartz (Fig. 4.39).

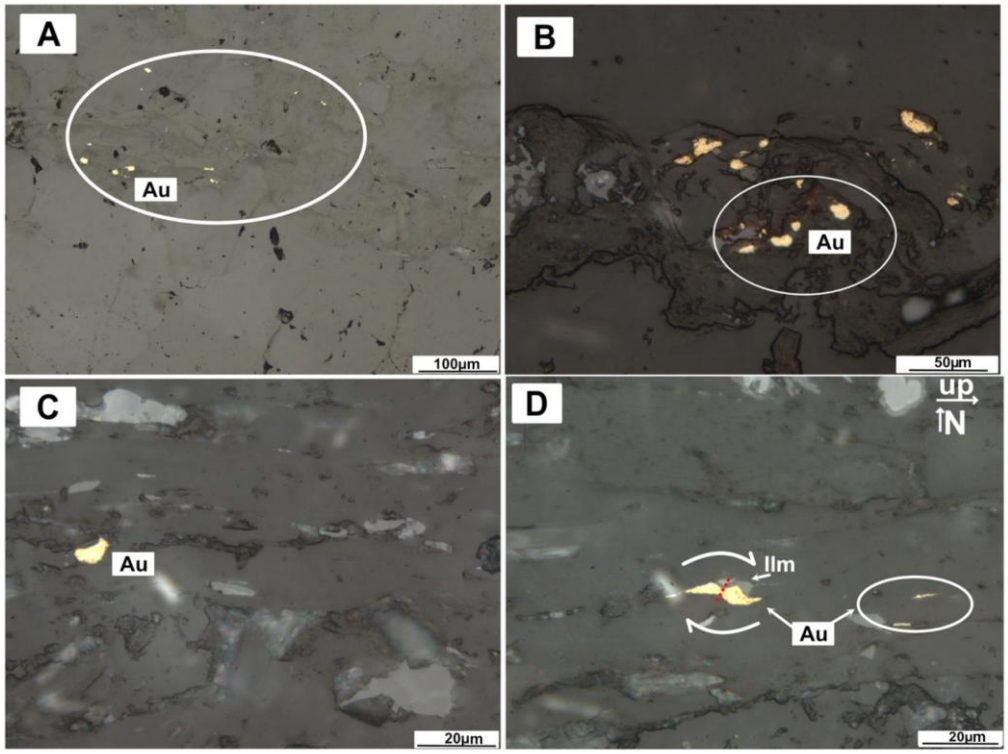

Fig. 4.39: Photomicrographs of 8-Zone sheared quartz veins. A: Several gold grains in a sheared quartz veinlet, associated with chlorite, muscovite, and siderite. B: Several gold grains within a shear band of preferentially orientated mica. C: Gold grain occurrence on veinlet selvedge. D: Gold grain with dextral shear sense kinematics.

4.4 SEM-EDS Analysis

The scanning electron microscope at Lakehead University was used to characterize the gold chemistry and to perform some minor mineral identification. In one instance, gold was observed to be directly associated with galena, and a pure platinum grain was noted in thin section ER-RB-8Z-C within a sheared quartz vein.

4.4.1 Gold & Platinum Characterization

Multiple occurrences of gold were observed in the 8-Zone sheared quartz vein polished thin section samples. Gold grains were observed up to 25 µm in size and generally independent of directly associated minerals; however, gold occurs with galena, the occurrence was not common enough to infer paragenetic relationships. The average chemistry of gold in the 8 Zone samples is 80% gold and 20% silver (Fig. 4.40). A platinum grain, 75 µm x 20 µm, was identified within a sheared quartz veinlet in the 8 Zone thin section samples. The grain is not associated with any minerals but was relatively close to multiple gold grain occurrences (about 1 mm away). The chemistry of the platinum grain was pure platinum (Fig. 4.40).

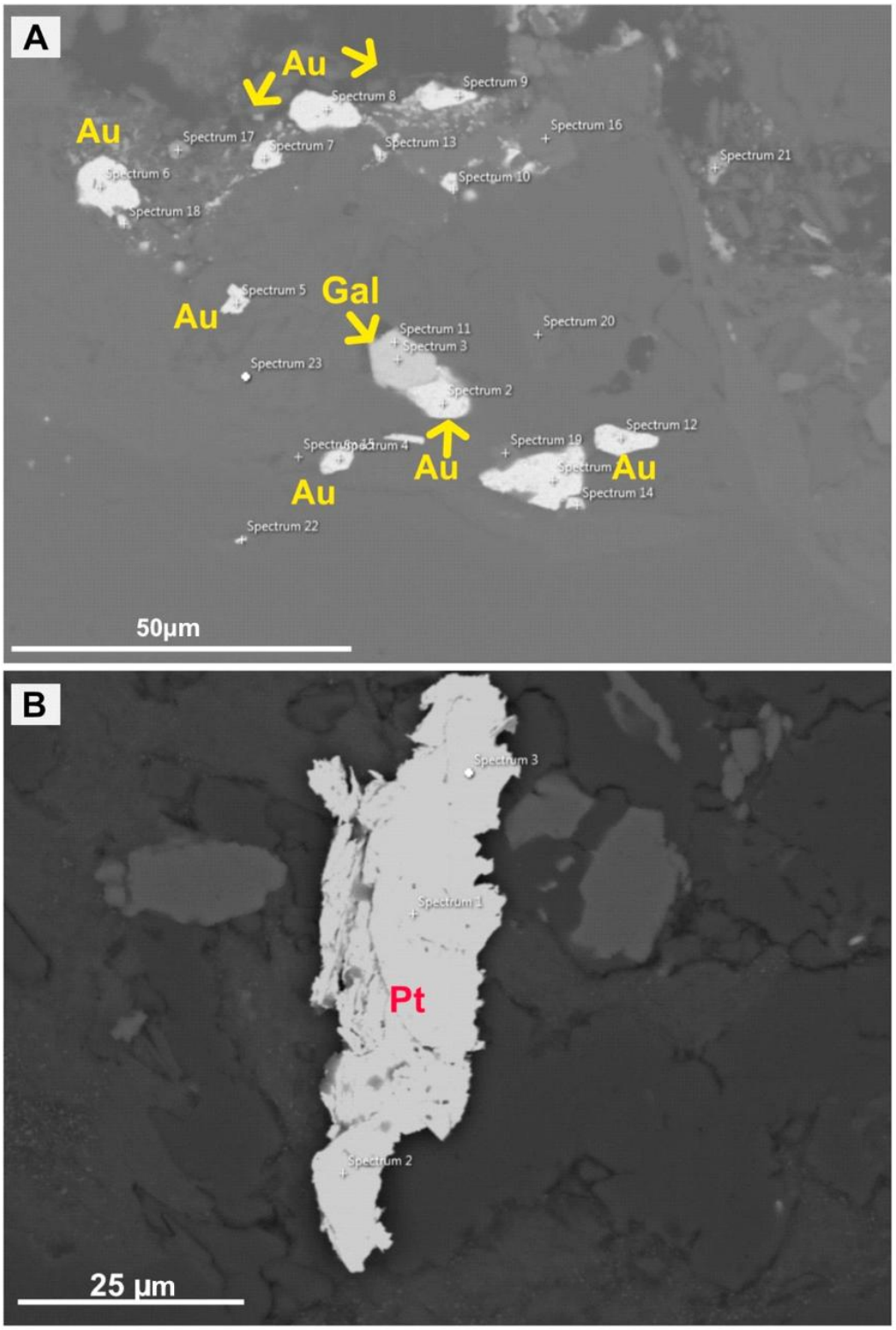

Fig. 4.40: SEM images A: multiple gold grains, one instance of gold directly associated with galena (Gal) in sample ER-RB-8Z-B. B: A pure platinum grain found in sample ER-RB-8Z-C.

4.5 Auriferous Shear Zones

The Eagle River gold-rich shear zones are primarily hosted in a calc-alkaline diorite pluton. Field observations suggest the mine shear zones are high-angle reverse shear zones with a right lateral component. For this section, petrography, Ti-in-quartz thermometry, electron backscatter diffraction (EBSD) mapping, and a new technique for determining vorticity axes from grain-scale dispersion of crystallographic orientations (CVA analysis) utilizing rotational statistics built from the work of Fletcher et al. (2004) are used to analyze microstructures induced by quartz deformation from the Eagle River mine shear zones (Michels et al., 2015).

4.5.1 Quartz Microstructure

Following the work of Stipp et al. (2002a, 2002b) and Knipe (1988) microstructural observations and interpretations of quartz veins and deformation mechanisms were interpreted through petrographic analysis of polished thin sections. Four 2-Zone samples (ER-RB-2Z-C, ER-RB-2Z-F, ER-RB-2Z-E and ER-RB-2Z-B) were selected for detailed analysis. Quartz microstructures observed in the 2-Zone sample suite have lobate grain boundaries, patchy and chessboard extinction, with relics of older parental grains exhibiting undulose extinction, evidence of previous deformation prior to shearing. Irregular grain boundaries are present, with fluid inclusion trails observed parallel with the shape-preferred orientation of grains. Quartz-quartz grain boundaries tend to have inequigranular inter-lobate grain boundary morphology; however, some samples bear polygonal, triple-point junctions at grain boundaries (Fig. 4.41). Higher strain shear bands occur throughout quartz veins.

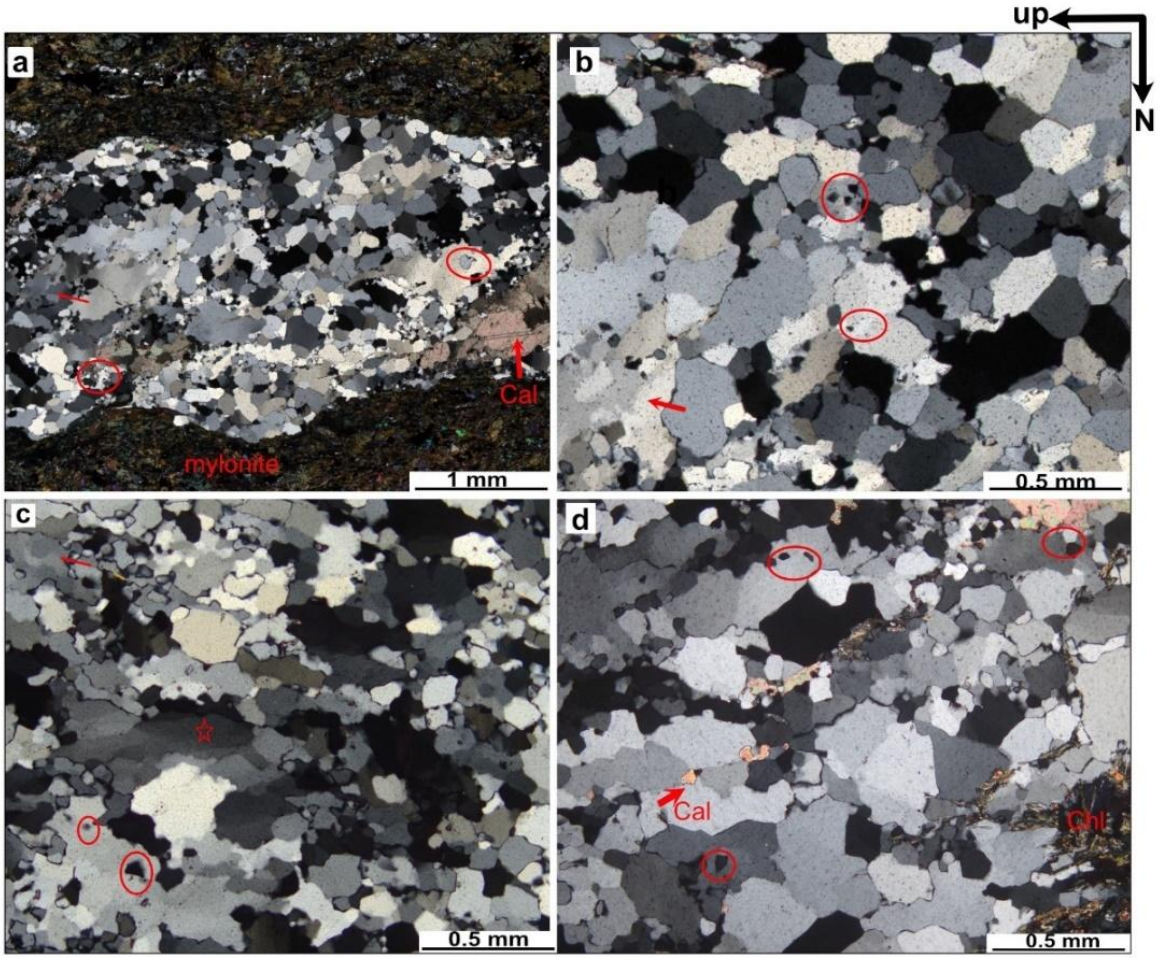

Fig. 4.41: 2-Zone sheared quartz vein samples; a. ER-RB-2Z-F, quartz veinlet hosted in mylonitic groundmass with an anastomosing selvage comprised of fine-grained amphiboles, epidote, chlorite and muscovite. Circled in red: bulging or grain boundary migration between two quartz grains, island grains and relict subgrains. b. Sample ER-RB-2Z-C shows island grains in red circles and relic grains indicated by red arrows. c. Sample ER-RB-2Z-H shows chessboard extinction indicated by a red star, numerous island grains shown in red circles and relic grains indicated by the red arrow. d. Sample ER-RB-2Z-B shows island grains circled in red and grain boundary instances indicative of grain boundary migration.

Four 8 Zone samples (ER-22-8Z-B, ER-22-8Z-H, ER-22-8Z-C, ER-22-8Z-K) were selected for detailed petrographic analyses. Samples of sheared quartz veins have a strongly pronounced stretching lineation, pressure solution seams, chessboard extinction, island grains, and multiple instances of grain boundary migration-related structures (Fig. 4.42).

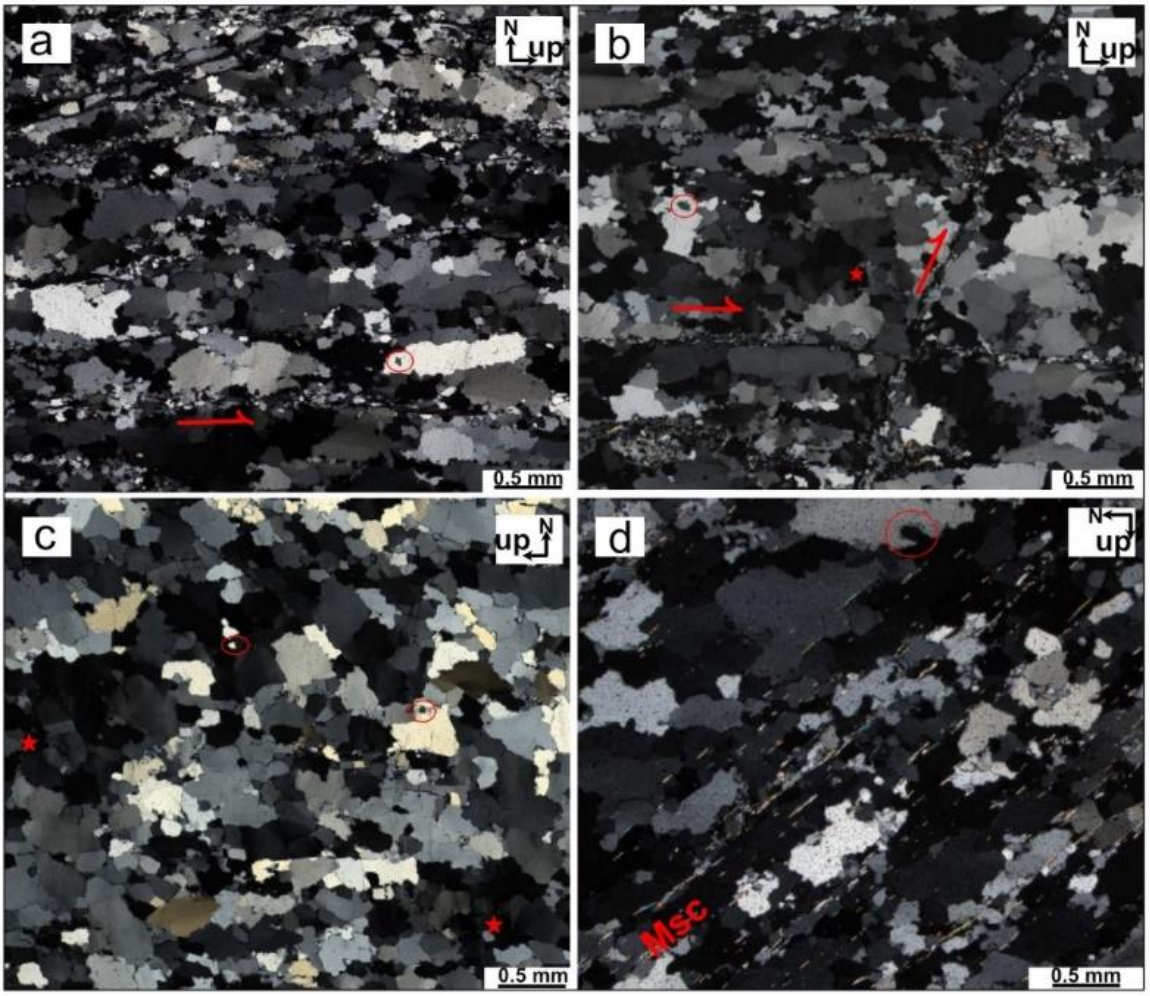

Fig. 4.42: Photomicrograph of 2-Zone sheared quartz vein GBM microstructures; samples: a) ER-2Z-B: elongated quartz grains, showing chessboard extinction with serrated and lobate grain boundaries (red arrows) and various island grains (red circles). b) ER-2Z-K: Polygonal quartz grains exhibit chessboard extinction, with many smaller grains surrounded by larger grains, and are in optical continuity with larger grains (island grains). Transitions exist between grains surrounded by high-angle boundaries and subgrains. A relic of a deformed old quartz grain occurs. c) ER-2Z-C has abundant lobate/inter-fingered to amoeboid grain boundaries that form chessboard patterns. d) ER-2Z-M: serrated grain boundaries with a lattice-preferred orientation and associated minerals calcite and chlorite.

4.5.3 Kinematic Microstructures

Shear zones 2 & 8 polished thin sections underwent detailed petrographic analysis to better understand kinematics and deformation mechanisms. Porphyroblasts and porphyroclasts, depending on the mineral type, act as less-deformed bodies in a ductile deformation system, and given the orientation characteristics of each tail, can be used to infer kinematic information (Passchier and Simpson, 1986). In mylonites, different fabrics can be inferred. S-C fabrics are kinematic/shear related micro to macro fabrics formed by two planar elements and interpreted to trace the XY-plane of the strain ellipsoid. S surfaces represent the shear plane, the shear direction related to the accumulation of finite strain, and C surfaces to the displacement due to high shear strain. There are two types of C-S fabrics: types 1 and 2. Type 1 involves narrow zones of intense shear strain, which cut mylonitic foliation. Type 2 is more common in zones of intense non-coaxial strain (Trouw et al., 2009; Lister et al. 1984). Asymmetrical micro-folds, quartz aggregate sigmoids, and asymmetrical quartz vein boudins were observed; all are hosted in very fine-grained mylonite (Fig. 4.43).

Porphyroclasts were observed in both sets of polished thin sections. Based on the classification system of Passchier & Simpson (1986), different types of porphyroclasts are shown in Figure 4.43.

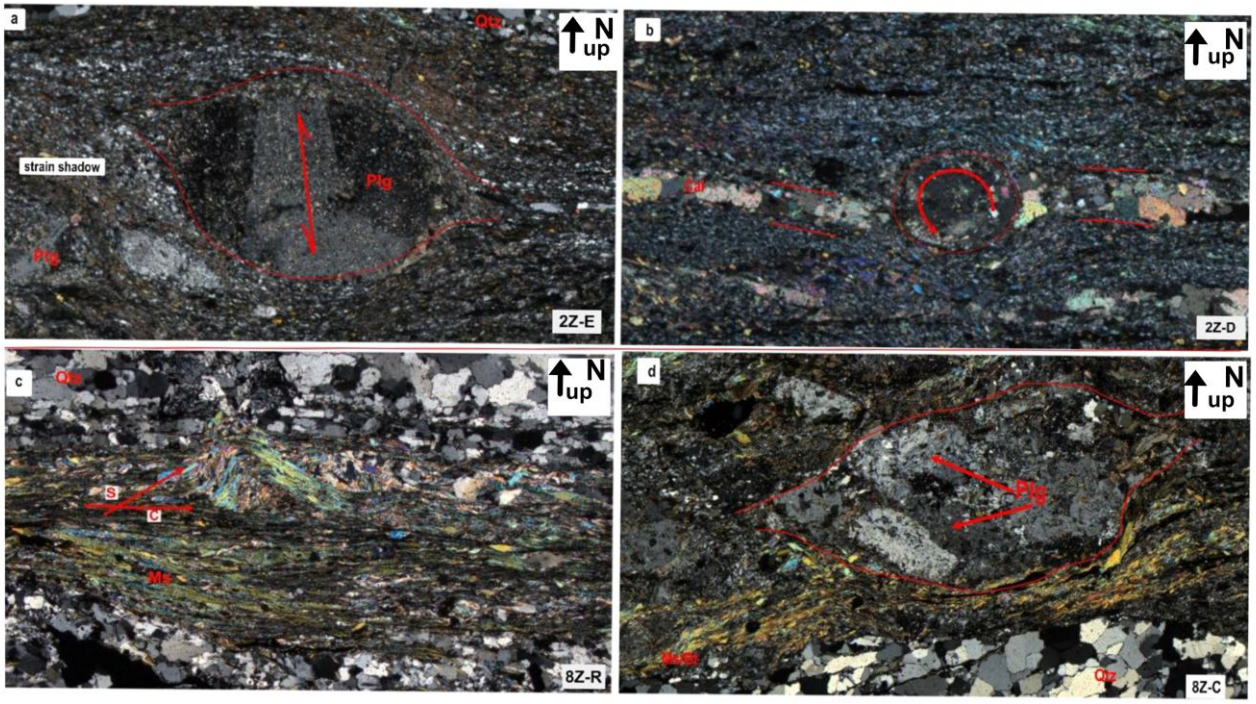

0.5mm

Fig. 4.43: shows a series of porphyroclasts in XPL; A: an equidimensional α type porphyroclast of plagioclase with fine-grained quartz representing a strain shadow on each side and cap on top and bottom. The red arrow indicates relic polysynthetic twinning. No shear sense can be interpreted due to symmetrical tails. b. a winged δ porphyroclast of plagioclase with a poikilitic texture, overprinted by calcite and white mica, hosted in a very fine-grained mylonite comprised of epidote, amphiboles, biotite, chlorite, muscovite, calcite, and fine-grained quartz. Shear sense is dextral, north side up. c. shear foliation deflection of the S fabric over a non-rotating rigid body, likely plagioclase, indicating syn-tectonic processes.

Kinematic microstructures observed were winged δ porphyroclasts, φ and α porphyroclasts, multiple instances of strong S and C fabric orientations (C-type shear bands), mica fish and quartz aggregate sigmoids. Asymmetrical micro folds, foliation deflections, and asymmetrical sheared quartz boudins. Plagioclase porphyroclasts are represented as rigid bodies and are the dominant porphyroclast, sometimes with numerous occurrences in single thin sections (up to 10 per thin section), creating networks. Microstructural analysis reveals that both 2 and 8 Zones exhibit a reverse sense of shear with the north side up (hanging wall) and the south side down (footwall) kinematics.

4.6 Titanium-in-Quartz

We analyzed Ti concentrations in sheared quartz veins from zones 8 and 2, and temperatures were calculated using the Titanium in quartz method or TitaniQ based on the work of Thomas et al. (2010). Nearly half of EPMA readings were below detection limit and the subset of samples within detection limit were used to calculate the peak crystallization. This is not ideal, but interesting, nonetheless. Figure 4.44 shows the distribution of titanium concentrations in each set of samples from the respective shear zones. The plot highlights the data's central tendency, variability, and potential outliers.

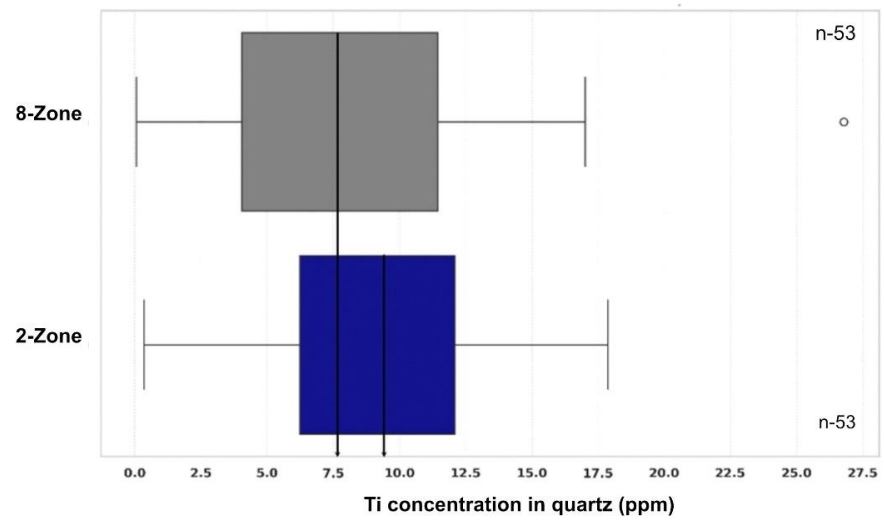

Fig. 4.44: Box plots representing EPMA data of Ti concentration in quartz of each respective shear zone. The 8 Zone is grey, and the 2-Zone is blue, n=53 for each plot.

8 Zone samples show a median Ti concentration of 7.66 ppm, represented by the line inside the box. The interquartile range (IQR) spans from the first quartile (Q1) at 4.04 ppm to the third quartile (Q3) at 11.44 ppm, encompassing the middle 50% of the data. The whiskers extend to the minimum and maximum values within 1.5 times the IQR, capturing most data points, minus some outliers. The mean Ti content for the 8 Zone samples is 8.29 ppm, with a range of 1.10-26.74 ppm.

The 2-Zone samples show a median Ti concentration of 9.42 ppm. The IQR ranges from 6.24 ppm (Q1) to 12.09 ppm (Q3). The whiskers extend to the minimum and maximum values, with fewer outliers than in the 8Z samples. The mean Ti content for the 2-Zone is 9.15 ppm, with a standard deviation of 17.52 ppm. Unfortunately, both sample suites are unreliable due to a high number of EPMA Ti readings below the 10-ppm detection limit; therefore, the error margins are too high in most cases to produce conclusive results.

Using the TitaniQ thermometry work of (Wark and Watson, 2006a) peak quartz recrystallization temperatures were calculated from the titanium content in quartz grains, assuming an activity of 1 due to the presence of rutile observed in petrographic analyses (Fig. 4.45).

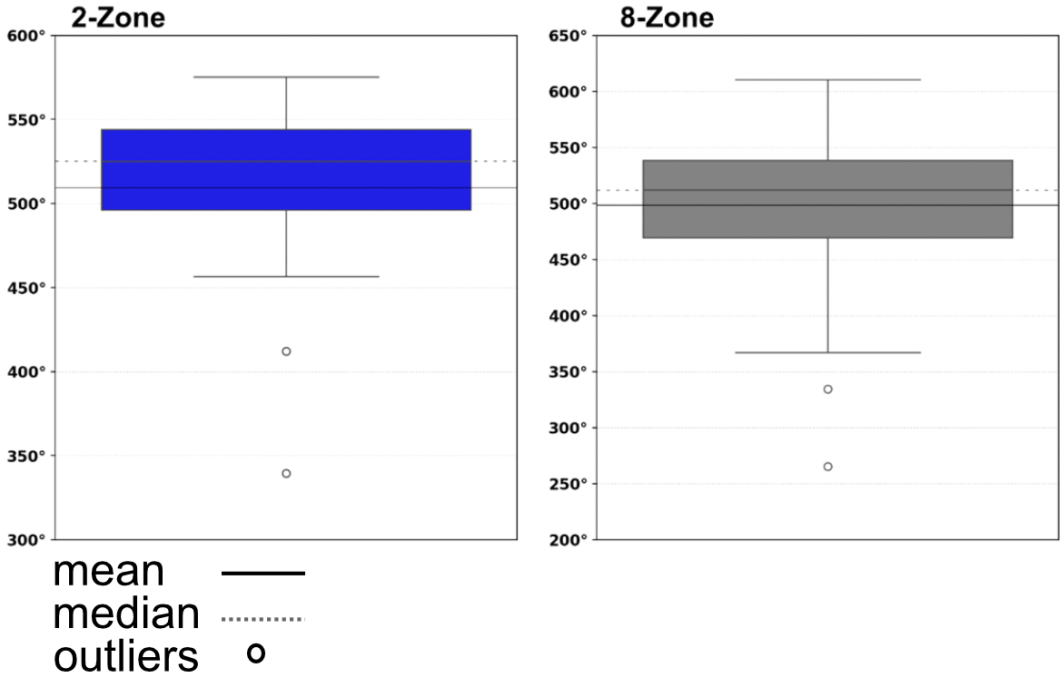

Fig. 4.45: Box plots of the TitaniQ thermometry technique based on the work of Wark and Watson (2006). The blue (2-Zone) and grey (8-Zone) boxes show the interquartile range (IQR) and contain the middle 50% of the data. The horizontal lines within the box represent the median (dashed) and mean (solid) of the temperature data. The whiskers extend to the smallest and largest values within 1.5 times the IQR of the lower and upper quartiles, respectively. Outliers in the data are shown in hollow dots. N = 53 for each plot.

Based on the work of Wark and Watson (2006), the 2-Zone's peak recrystallization temperature is slightly higher than the 8-Zone's. However, 50% of temperature calculations fall within the range of 496° to 544° for the 2-Zone and 470° to 539° for the 8-Zone. Unfortunately, many readings were below the microprobe's detection limit of 10 ppm or 0.001 wt. %.

4.7 EBSD & CVA analysis

EBSD mapping and crystallographic vorticity analysis provide valuable insights into the crystallographic fabric of the quartz grains, including texture development and preferred orientations. This data can be used to better understand kinematics and deformation mechanisms in quartz veins within zones 2 and 8.

The microstructures from the Eagle River sheared quartz vein samples show evidence of medium to high-temperature crystal-plastic deformation. The mylonitic fabric is defined by quartz, amphiboles, biotite, titanite, carbonates, and muscovite, and it has fractured networks of plagioclase throughout. Recrystallization microstructures are indicative of dynamic recrystallization at temperatures <550°C (e.g., Passchier and Trouw, 2005), and hornblende shows a strong shape preferred orientation. Quartz is dynamically recrystallized, showing distinctive grain boundary migration (GBM) microstructures (Barber and Wenk, 1991; Stipp et al., 2002). Plagioclase porphyroclasts show no obvious recrystallization microstructures, indicating formation temperatures were not high enough to induce feldspar plasticity. Misorientation to mean maps shows the angular difference in crystallographic orientation within individual grains. The 2-Zone samples have high internal misorientations (> 10°) to the mean orientation (Fig. 4.46).

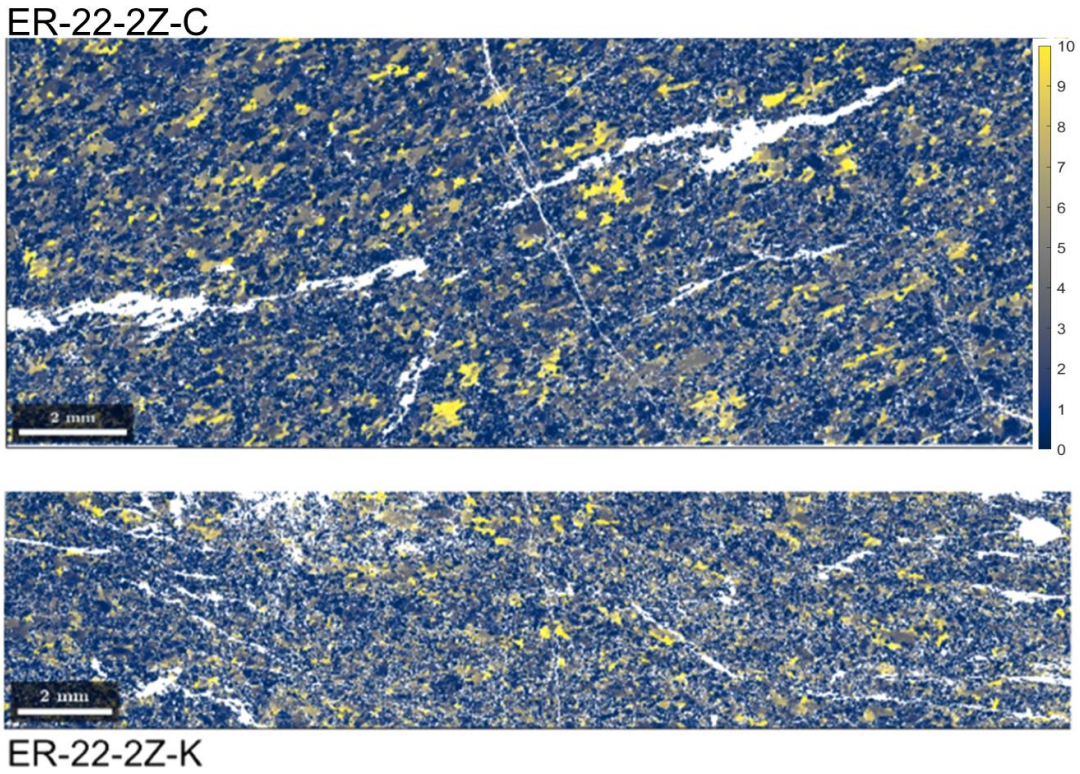

Fig. 4.46: Misorientation to mean orientation of quartz grain boundaries of sample ER-22-2Z-C & K quartz grain boundaries up to 10°.

The [0001] axes for both 2-Zone samples exhibit strong crystallographic preferred orientations, with high-intensity regions forming a girdle pattern. This suggests the c-plane (basal plane) is the glide plane, and the direction of the slip is parallel to the C axis. The [1120] and [1010] pole figures show complementary patterns of high intensity, sometimes offset by up to 30° (Fig. 4.47). Both 2-Zone samples show a strong crystallographic preferred orientation. 2 Zone K shows a cross-girdled pattern of c-axes indicative of basal <a> slip, and the 2 Zone C shows a more complex pattern due to the fact that the crystallographic vorticity axis is parallel to the lineation.

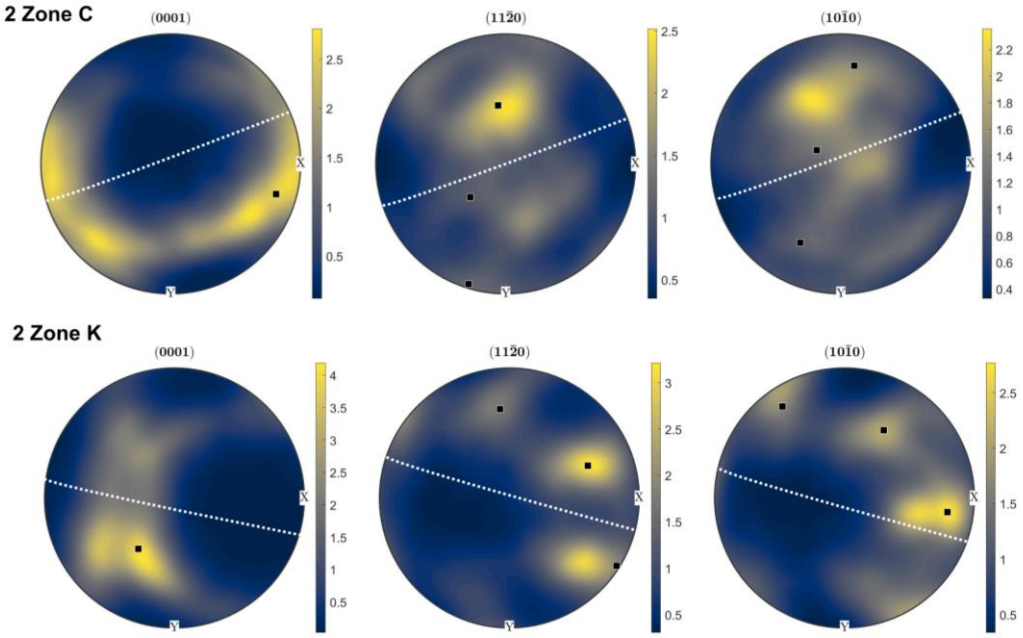

Fig.4.47: Equal area pole figures of crystallographic orientation density axes plotted on the [0001], [1120], and [1010] as points in space and time. Foliation is indicated with dotted white line.

The results from 2-Zone samples ER-22-2Z-K and ER-22-2Z-C that underwent CVA analysis are shown in Figure 4.48, plotted with lower hemisphere stereographic projections, and shown in the fabric reference frame relative to foliation and lineation. Point data for ER-22-2Z-C shows one independent direction parallel to the lineation that suggests a pure shear signature, and ER-22-2Z-K shows one independent direction parallel to the lineation in the center of the pole figure, indicating simple shear kinematics (Michels et al., 2015).

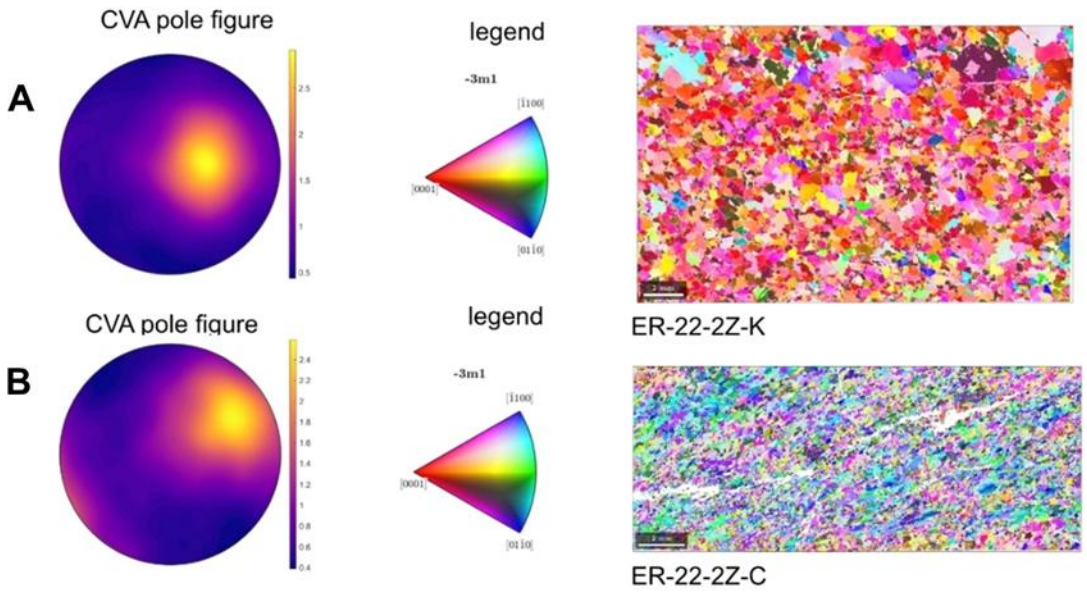

Fig. 4.48: CVA data plotted on two pole figures, legends, and inverted pole figure maps.

The 8 Zone sample's misorientation to mean maps show high internal misorientations (>10°) to the mean orientation (Fig. 4.49).

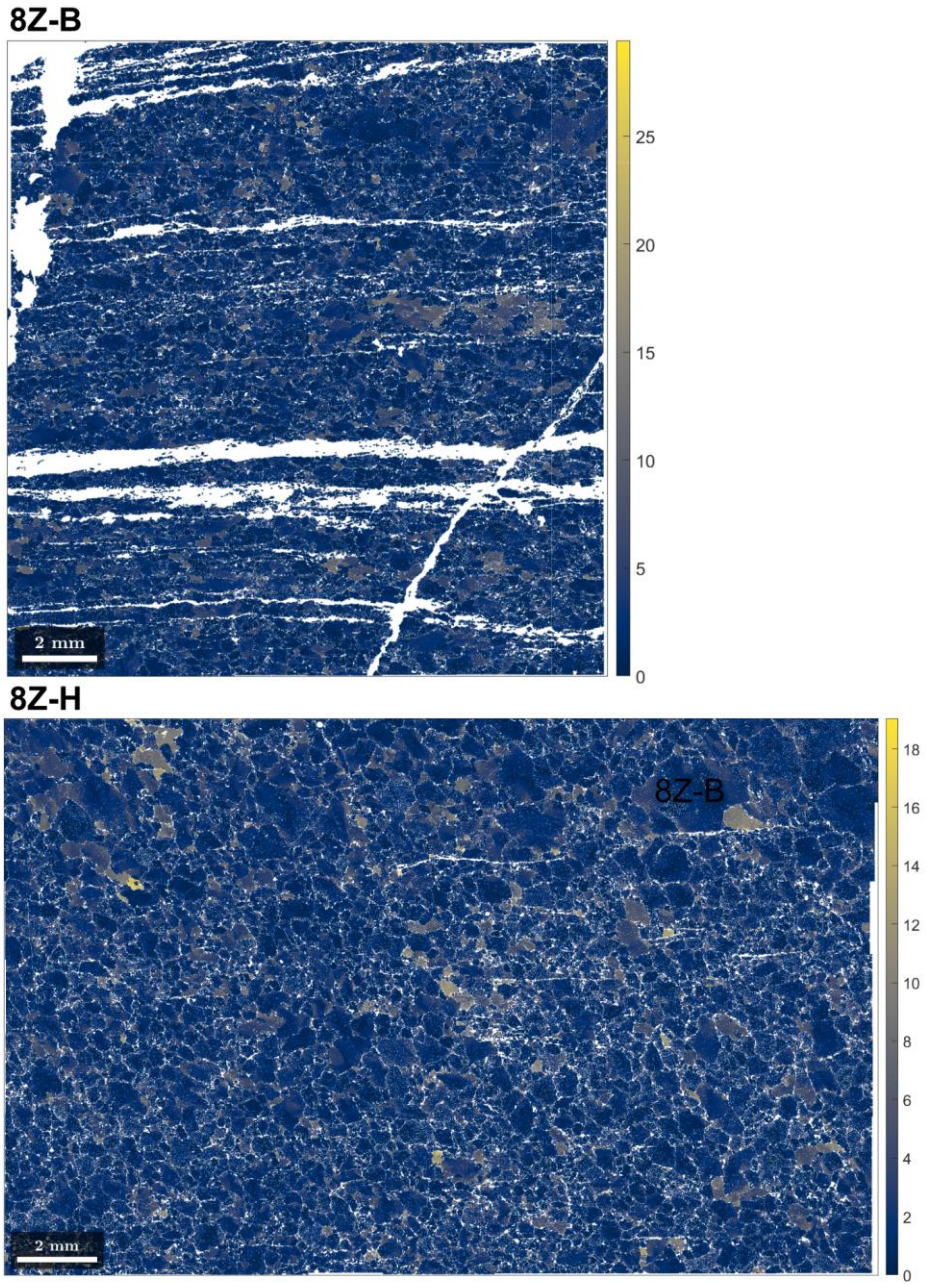

Fig. 4.49: Misorientation to the mean of grain orientation, up to 10°. Blue is the average grain boundary direction, and yellow is 10° different from the blue quartz grains.

The 8 Zone lower-hemisphere pole figures show two major intensity peaks, with a bimodal maximum on [0001]. Misorientation textures on the [1120] show a more asymmetric distribution and are more spread out, with a more elongated intensity pattern, with similarities observed on the [1010] lattice plane. ER-RB-22-H shows a dominant girdle pattern on the [1120] and [1010] due to multiple axes (3) for these two planes (Fig. 4.50).

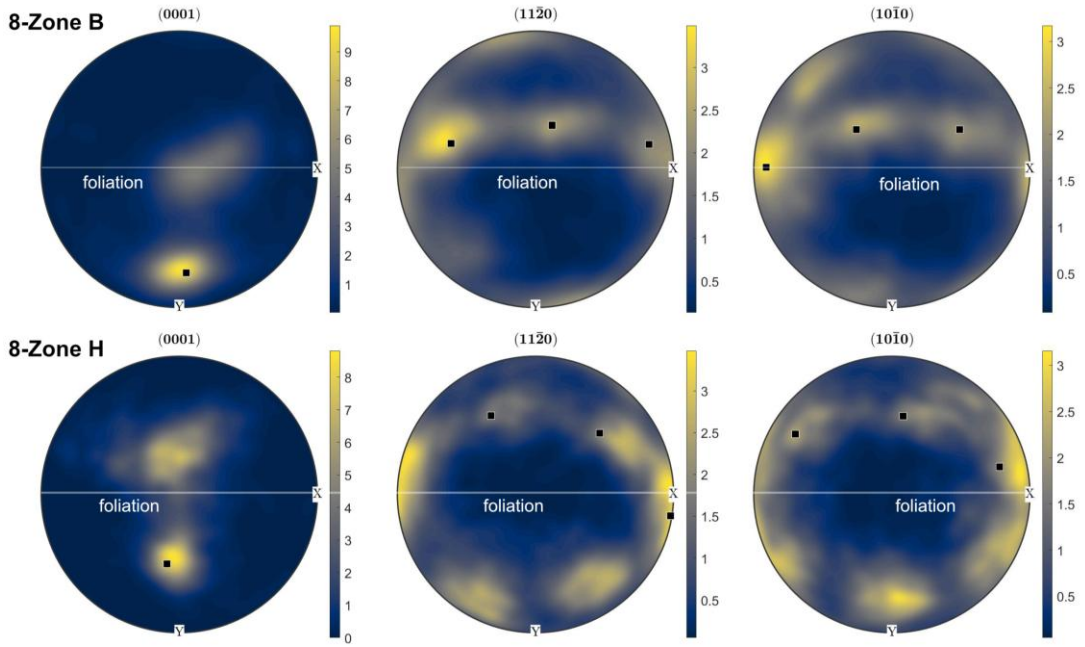

Fig. 4.50: Equal area pole figures of crystallographic orientation densities plotted on axes [0001], [1120], and [1010] as points in space and time.

The CVA results from gold-bearing 8-Zone samples are shown in Figure 4.51, plotted with lower hemisphere stereographic projections, and shown in the fabric reference frame relative to foliation and lineation. Point data for ER-22-8Z-B shows a simple shear signature

overprinting a pure shear signature, and ER-22-2Z-H shows an independent, simple shear pattern.

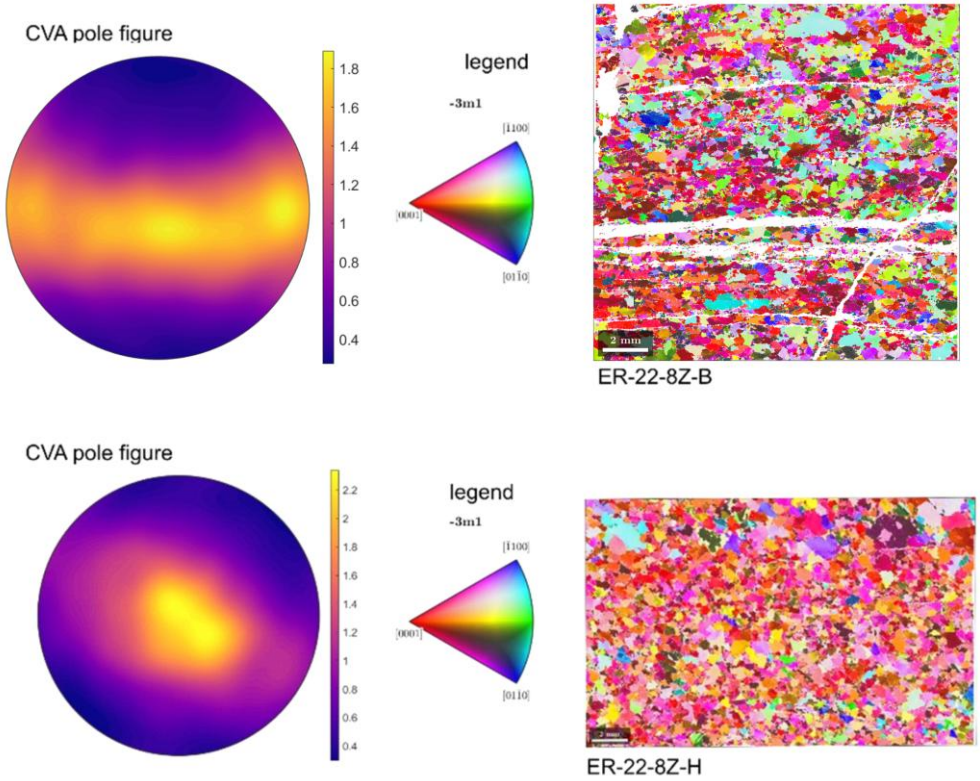

Fig. 4.51 CVA data plotted on two lower hemisphere pole figures, legends, and inverted pole figure maps. CVA maxima show two distinct high-strain events: simple shear overprinted with pure shear.

4.8 Eagle River Brittle Deformation

The Eagle River mine and nearby areas have undergone extensive deformation; for this study, a property-wide fault was selected for further research to assess its kinematics and conditions and to see if and how the fault interacts with the Au-bearing, ductile Eagle River deformation corridor. Drill hole ERS-2022-026 was used as it intersects the NW fault and exhibits brittle deformation structures such as a damage zone, extensive hydrothermal alteration, micro breccia and fault gouge. Two fault gouge samples from drill hole ERS-2022-026, one at a depth of 353.74 meters and the fault gouge sample that intersects the NW fault of interest at

420.05 meters, were selected for microprobe analysis of chlorite grains at the University of Toronto. These data were used to assess the temperature of chlorite formation using the geothermometer for diagenetic to low-grade metamorphic conditions based on the work of Bourdelle et al. (2013) and Bourdelle and Chathelineau (2015). This geothermometer process allows an estimation of the temperature of chlorite formation from the chlorite chemical composition.

4.8.1 Brittle Microstructure – Drill Hole ER-2022-026

This section will characterize the lithologies and microstructures from drill hole 2022-026, starting in the undeformed rock above the fault-related structure and alteration, then sequentially moving downhole. The fault gouge intervals are hosted in andesitic basalt, highlighted by high degrees of chlorite, epidote and carbonate alteration levels. Drill hole ERS-2022-026 was drilled at an azimuth and dip of 055°/-45°.

Sample ER-22-026-08 was taken at -394.00 m. This unit is characterized by an orthoclase-rich pegmatitic dyke; the intrusion extends from 393.1 to 403.45 m. There are two different domains of feldspar; one is the dominant mineral, orthoclase (70%), with grain sizes up to 10 mm, and the other is albite (25%), with grain sizes up to 4mm, fine-grained quartz occurs in veinlets and fractures, and, up to 5cm patches in drill core (>5%). Very fine-grained muscovite, biotite and chlorite occur in veinlets and fractures at grain boundaries (1%; Fig. 4.52b).

Fig. 4.52: A: Drill core photo of an anorthoclase-rich pegmatite dike. B: Photomicrograph of the pegmatite dyke (XPL, 5x) with a focus on a large 10 mm orthoclase grain. Carlsbad twinning in orthoclase (white square) and with cleavage planes intersecting at 90°.

Sample ER-22-026-10 was taken at -412.85m depth; the original lithology of this unit is andesite or intermediate volcanic rock. Very fine-grained quartz, plagioclase, calcite and epidote comprise the groundmass, with larger, porphyritic, 0.60 mm plagioclase grains and orthoclase grains overprinted with sericite. The unit is highly altered and is interpreted to be well inside the fault's damage zone with micro-cracks infilled with phyllosilicate. Biotite and hornblende occur as fine to medium grained minerals and are altered to chlorite. Trans-granular fractures are present and increasing in density towards the primary fault core, propagating at grain boundaries and infilled with a fine-grain matrix of quartz, plagioclase, and calcite. The sample is highly altered with domains of calcite in veinlets and groundmass (Fig. 4.53). Epidote and clinozoisite occur disseminated in fine-grained inclusions. Minor amounts of gouge material have accumulated in this section alongside anastomosing bands of quartz. Overall, the unit is highly

silicified with foliation parallel bands of up to 5 cm wide calcite bands and large 30 cm sections of orthoclase-rich pegmatite.

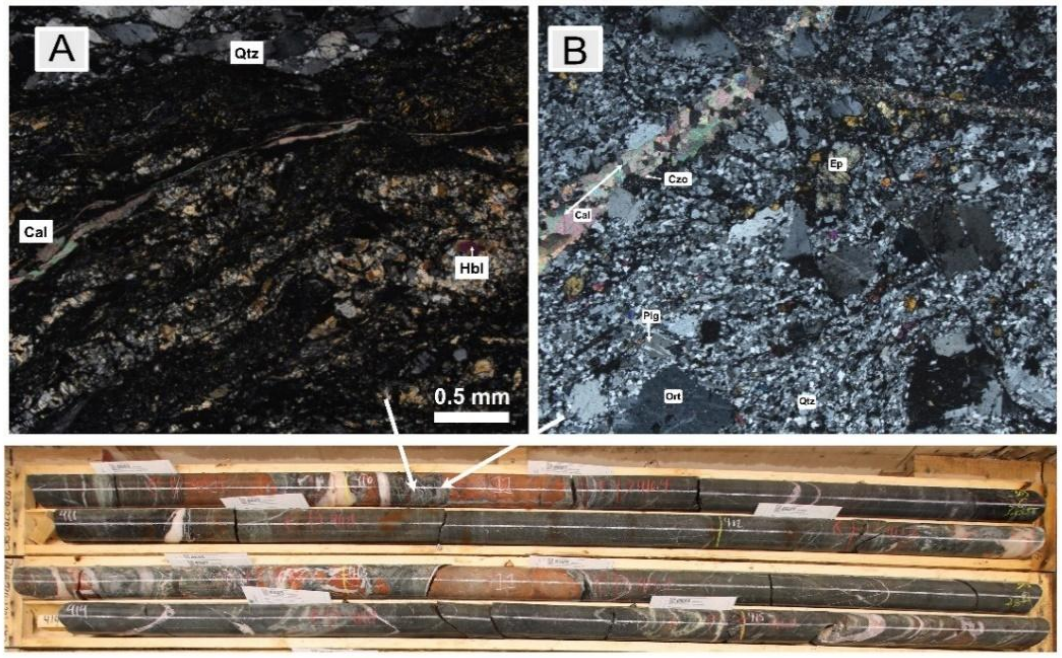

Fig. 4.53: Two photomicrographs of PTS ER-026-10 and drill core photo of hole ER-026. A: XPL 5x, fine- to medium-grain phyllosilicate matrix with an anastomosing boundary with quartz grains. B: XPL 5x of proto-lithology andesite with calcite veinlets and fine-grained microcracks of phyllosilicates, quartz and plagioclase.

Sample ER-22-026-11 was taken one meter above (-419 m) the fault core slip surface (gouge) section and considered to be in the primary fault's damage zone. This unit's protolith is basalt, characterized by intense hydrothermal fluid flow causing alteration and fault breccia. Iron-rich (hematite) fluids have migrated within the breccia clast network. Various angular clasts of altered basalt, orthoclase, and calcite occur, all silicified by silica-rich hydrothermal fluid flow (Fig. 4.54). The breccia is interpreted to be cohesive, and clasts range in size from micro breccia to fine crush to crush breccia. Based on the work of Sibson (1977), this would be classified as a cataclasite. Thin-section analysis is characterized by up to 4 cm of breccia with fracture networks of silica-rich pathways. The clasts have been overprinted by a fine-grained matrix of

phyllosilicates and amphiboles, with fine-grained biotite altering to chlorite and hornblende altering to actinolite and chlorite.

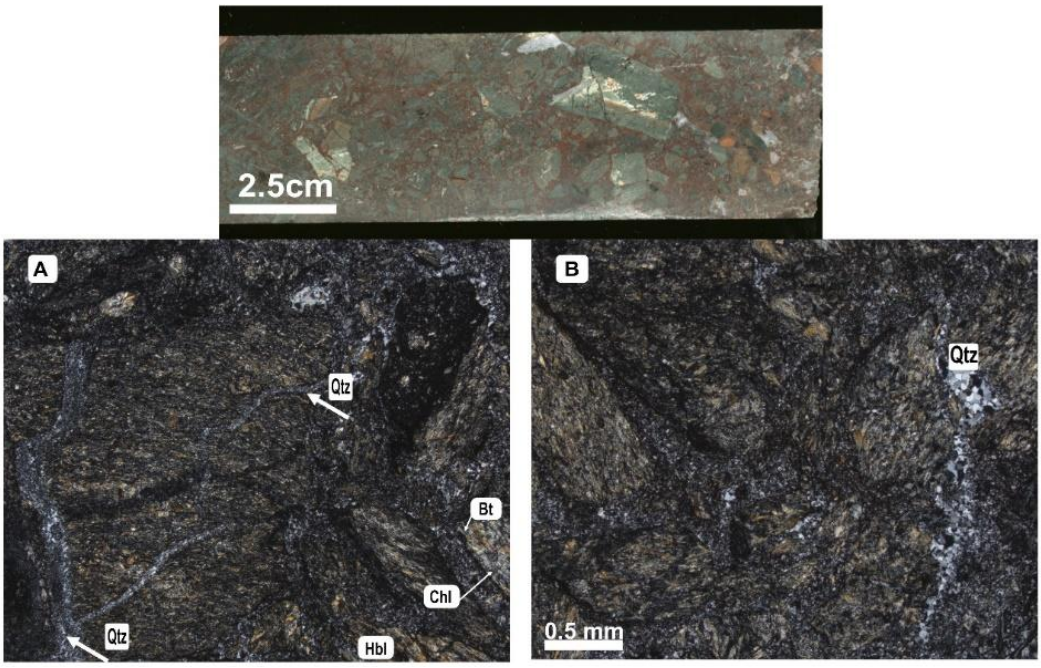

Fig. 4.54: Drill core from 1 meter above the gouge illustrates the consolidated cataclastic fault breccia network. A & B are photomicrographs of the same unit, showing up to 4cm breccia clasts with a network of fine-grained quartz-infilled fractures.

Fault Gouge A, representing the fault slip surface or the core of the fault and associated structures, begins at -419.70 m and extends to -421.80 m. Its protolith is basalt or mafic volcanic rock. It is characterized by ultra-fine-grained, magnesium-rich chlorite and clay with clasts of fractured plagioclase that are almost unrecognizable. It is interpreted to be unconsolidated with a size of less than 20% larger than 2 mm. Calcite fragments overprint the gouge matrix, representing the porous, unconsolidated fault core.

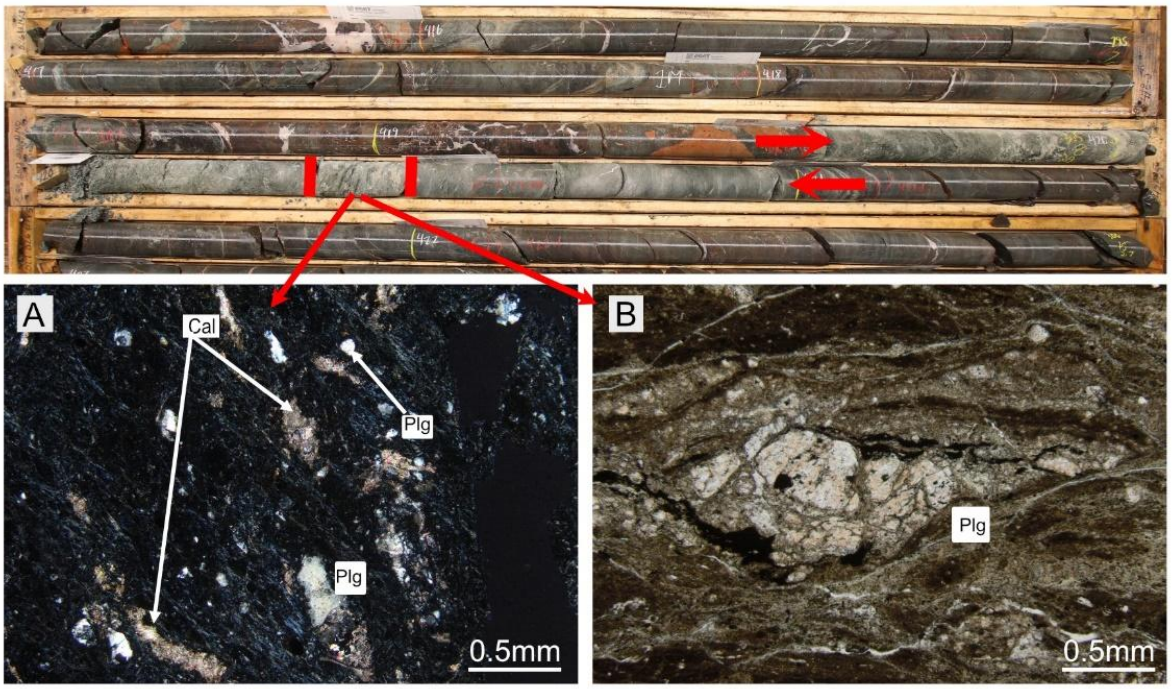

Fig. 4.55: Core photo of fault gouge interval and photomicrographs of the fault sample; the sample interval is indicated with red lines.

Fault gouge sample B was retrieved at -353.74 m depth and is characterized as an ultra-fine-grained incohesive gouge with chlorite, illite, quartz, calcite and dolomite (Fig. 4.56).

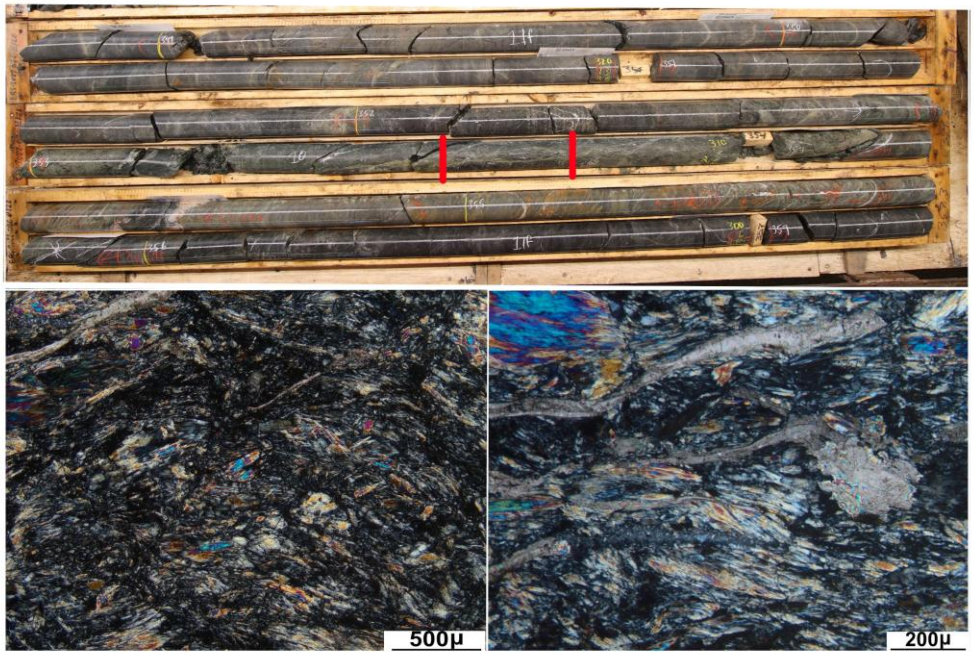

Fig. 4.56: Core photos and photomicrograph of Gouge Sample B taken at 353.74 m depth showing fine-grained chlorite, biotite, calcite and dolomite.

4.10 Chlorite Thermometry

EMPA data from chlorite grains analyzed in two fault gouge intervals from Eagle River were plotted on the Si-R^{2+} versus Si/O_{14} diagram. Figure 4.59 incorporates isotherm lines derived from the quadratic equation from Inoue et al. (2009) and the work of Bourdelle et al. (2013).

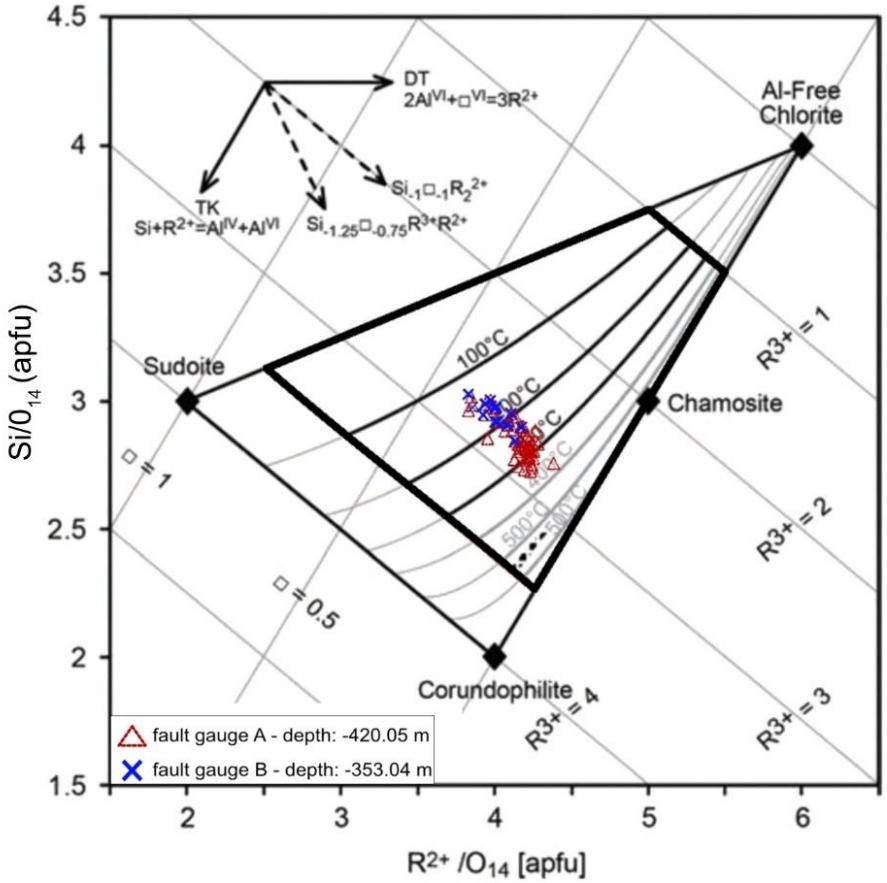

Fig. 4.57: Plot modified from Bourdelle et al. (2013b) representing isotherms and the respective calculations using the Bourdelle et al. (2013b) chlorite thermometer.

Gouge sample A plotted at slightly higher temperatures compared to B. Both are within the 125 – 325°C classification of low to medium-grade formation conditions (Fig. 4.59). Data sites analyzed with microprobe in fault gouges A and B were of the chlorite variety, pynochlorite, with a small amount classified as ripidolite (Bourdelle and Cathelineau, 2015).

Chapter 5: Discussion

The Eagle River gold deposit in the Mishibishu greenstone belt of northern Ontario, Canada, preserves a significant part of a Neoarchean accretionary orogenic system. This research examined both the geochemical signatures of the mine and nearby host rocks as well as the structural characteristics of the high-grade, gold-bearing shear zones within the Eagle River deformation zone. By employing an integrated approach that combines detailed field mapping, lithogeochemistry, Sm/Nd isotope analysis, EBSD mapping, CVA analysis, chlorite and TitaniQ geothermometry, this study provides an in-depth insight into the formation and evolution of a high-grade Neoarchean orogenic gold deposit.

5.1 Eagle River Geochemistry

Lithogeochemical and isotope data can provide insights into tectonic history. A useful way of classifying greenstone belt lithologies is to assess a rock unit's magmatic affinity. Traditional AFM – total alkali, iron and magnesium plots incorporate elements that are mobile during metamorphism and alteration, making them unreliable in Archean rocks. Given the potential for the mobility of some elements during alteration and metamorphism we plotted major elements against the general immobile TiO_2 (Fig. 4.26). The majority of the major elements show coherent trends with limited scatter with the exception of K_2O and Na_2O suggesting that only the LILE are mobile in the studies rocks. In order to further mitigate against possible secondary alteration effects and hence address primary compositional characteristics, this paper concentrates on elements demonstrated to be generally least mobile during alteration of Archean volcanic rocks, namely Al, Ti, Ni, Y, Sc, V, REE and HFSE (Jochum et al., 1991; Lafleche et al., 1992; Arndt, 1994).

Ross and Bedard (2014) proposed a magmatic affinity plot that uses incompatible REE ratios Th/Yb against Zr/Y to determine if a lithology is tholeiitic or calc-alkaline. Higher Th/Yb ratios typically indicate greater crustal contamination and a calc-alkaline magmatic affinity reflecting crustal input and/or subduction-driven influences. The Zr/Y ratio increases during fractional crystallization with lower degrees of partial melting and can reflect a rock sample's tectonic setting. The Eagle River mafic samples plot as tholeiitic, and the intermediate and felsic samples plot as calc-alkaline. This suggests the mafic samples were derived from a more primitive oceanic crustal setting, while the intermediate and felsic samples indicate subduction-related geochemical signatures (Ross and Bedard, 2009).

Spider diagrams compare light and heavy REE concentrations to a standardized REE content of significant, undifferentiated material from a known source, such as distinct basalt-forming environments, N-MORB, E-MORB or OIB, chondrites, and mantle sources such as the primitive mantle (Sun and McDonough, 1989). Two groups of tholeiitic basalt have been recognized at the Eagle River property. Both display primitive compositions with little evidence for crustal interaction. Group A has a negative Nb anomaly (Nb/Nb* = 0.59-0.68), near flat to weakly enriched light rare earth content (LREE) with (La/Sm_{pm} = 0.94-1.25) and HREE values that are flat to weakly fractionated HREE with (Gd/Yb_{pm} = 1.3 to 1.58). Group B has a negative Nb anomaly (Nb/Nb* 0.56-0.83), weakly enriched in LREE with (La/Sm_{pm} = 0.90-1.48) and plot to weakly fractionated HREE with a Gd/Yb_{pm} ratio of (0.88 to 1.62). Group B has slightly higher HREE and LREE values (Fig. 5.1).

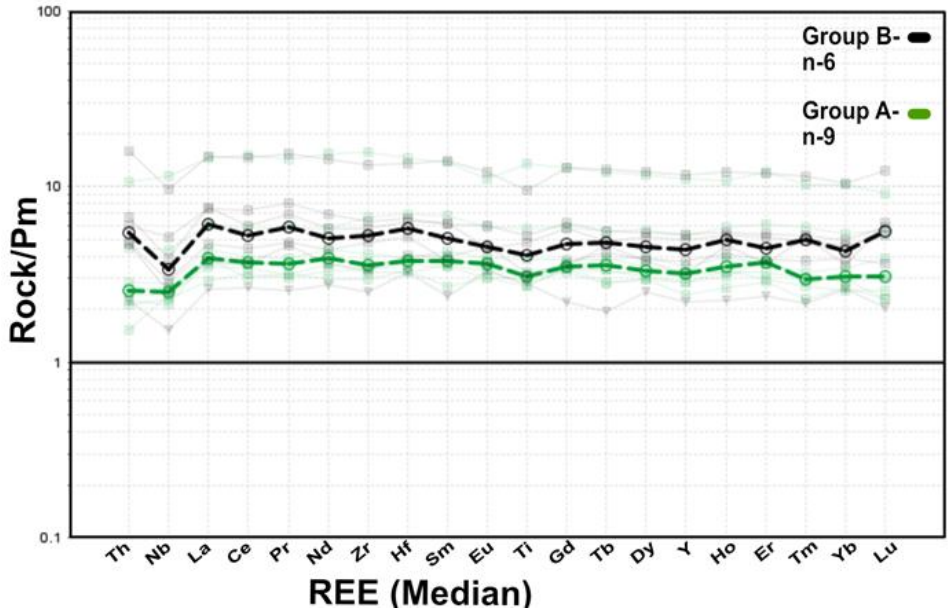

Fig. 5.1 – averages of mafic spider plots group B and group A (*Sun and McDonough, 1989)*

The Eagle River tholeiitic basalt Sm/Nd isotope values of $\varepsilon Nd_{T(2700)}$ range from+1.93 to +2.50. Positive εNd values in igneous rock are consistent with mantle-derived magmas that have experienced minimal interaction with the continental crust during ascent and emplacement, suggesting formation within an intra-oceanic environment (Huston and Gutzmer, 2023; Sun and McDonough, 1989). These values fall within the published range for mafic Archean mantle-derived samples in the Superior craton, and particularly align with the work of (Polat, 2009) for tholeiitic plateau basalts in the eastern region of the Wawa subprovince in the nearby Schreiber-Hemlo, Winston Lake greenstone belts and the Lumby greenstone belt near Red Lake, Ontario (Hollings and Wyman, 1999; Kerrich et al., 2008; Nymoen et al., 2025).

Comparing the Eagle River tholeiitic basalts to several known modern analogues, such as the Otong Java plateau basalts, typical mid-ocean ridge basalt and arc-related ocean island basalts, the Eagle River basalts most closely resemble the Ontong Java plateau (Mahoney et al., 1993; Fig. 5.2).

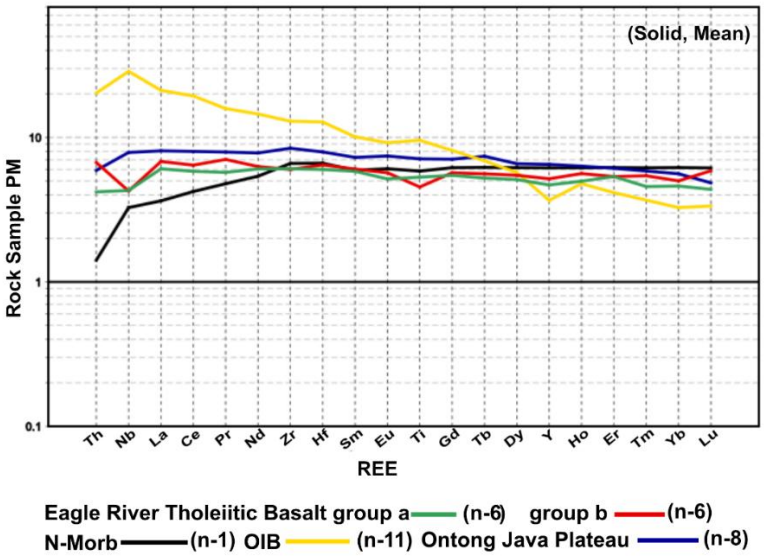

Fig. 5.2: Spider diagram of basalt from various modern tectonic environments compared to those of this study. Comparison data from Mahoney et al. (1983)

These findings align with Polat's (2009) characterization of plateau-related Mg to Fe-tholeiitic basalts (2750-2700 Ma) in the Wawa subprovince and suggest the Eagle River tholeiitic basalts were formed in an oceanic plateau environment. The REE patterns of the Wawa oceanic plateau basalts range from depleted, N-MORB-like signatures to flat, oceanic plateau-like signatures and extend to enriched E-MORB or OIB-like trends (Polat, 2009; Polat and Kerrich, 2001). Data on Phanerozoic plume-driven oceanic plateaus and ocean islands (e.g. Hards et al., 1995; Mahoney et al., 1995; Kerr et al., 1997; Hofman, 2004; Kerr, 2004) is consistent with the Eagle River basalt geochemical variations. Polat (2009) suggested that subtle amounts of geochemical diversity as observed in the two types of Eagle River tholeiitic basalts are best explained by mixing distinct melt types, enriched and depleted, within an ascending, heterogeneous mantle plume. The enriched and depleted characteristics likely reflect differences

in the degree of partial melting, with lower percentages generating melts and higher percentages producing depleted variations (Polat, 2009).

The Eagle River intermediate suite exhibits a diverse compositional range, comprising calc-alkaline andesites, diorites, and gabbroic diorites, with SiO_2 contents spanning 52 to 63 wt.%. The calc-alkaline affinity of these rocks, coupled with their broad compositional spectrum, suggests a complex magmatic evolution. A noteworthy feature is the distinction between two geochemically distinct types within the intermediate suite, differentiated by their Zr/Hf ratio systematics (Fig. 5.3). Zircon is the primary reservoir for Zr and Hf. The crystallization of zircon controls Zr/Hf, imprinting low Zr/Hf phases on coexisting melts. Thus, a low or negative Zr/Hf value is a unique fingerprint of effective magmatic fractionation in the crust (Claiborne et al., 2018). Figure 5.3 shows the intermediate sample suite comprised of diorites and andesites grouped based on either a negative or positive Zr/Hf anomaly.

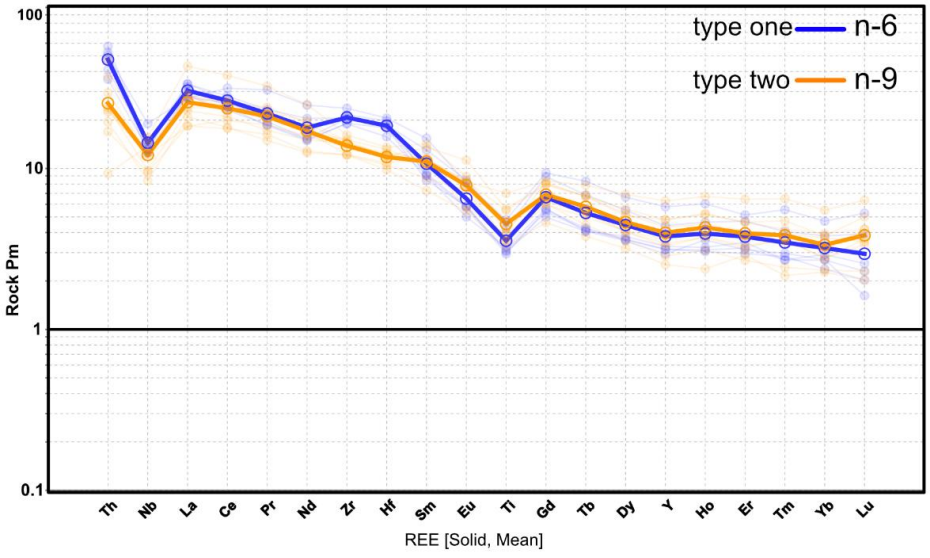

Fig. 5.3: Spider plots of the Eagle River intermediate suite. Normalizing values from Sun and McDonough (1989)

Group one samples display positive Zr/Hf anomalies in contrast to group two, with negative Zr/Hf anomalies. All intermediate samples are accompanied by negative Nb (Nb/Nb*=

0.02-0.71) and Ti anomalies (Ti/Ti* = 0.39-0.85) combined with moderate LREE enrichment (La/Sm_{pm} = 1.29-5.82) and fractionated HREE (Gd/Yb_{pm} = 0.70-4.28) suggesting a magmatic evolution dominated by fractional crystallization, driven by subduction related processes. The positive Zr/Hf anomalies likely indicate preferential retention of Hf in residual phases during partial melting and the differential behaviour of Zr and Hf during magmatic differentiation (Hollings & Wyman, 1999; Fig. 5.3).

The new age of 2720.60 ± 0.15 Ma for the Northern Diorite, and the recent Wawrzonkowski (2024) Mine Diorite age of 2716.22 ± 0.41 Ma indicates that the Northern Diorite is slightly older. Given that the intrusions are both geochemically heterogeneous, the North Diorite is a reasonable candidate for further exploration, due to the timing potential for gold-related, ductile deformation. The two diorites have very similar REE signatures, with similar Nb and Ti anomalies, moderate depletions in LREE, and moderately fractionated HREE, suggesting a similar petrogenesis (Fig. 4.36). Sm/Nd isotope values for the Mine Diorite are $\varepsilon_{Nd\ (2700\ Ma)}$ (+2.10) and the North Diorite $\varepsilon_{Nd\ (2700\ Ma)}$ (+2.02), supporting a similar source.

The intermediate to felsic suite from the Bowman Lake batholith and eastern portion of the northern diorite pluton represents an evolved magmatic system with high silica content (67-74 wt.% SiO_2) and calc-alkaline affinity. The suite, comprising three granite and five granodiorite samples, displays a restricted compositional range of evolved arc magmas. The relatively low concentrations of mafic components (MgO: 0.21-1.29 wt.%, Fe_2O_3: 1.18-3.71 wt.%, TiO_2: 0.04-0.42 wt.%) coupled with moderate Al_2O_3 (14.8-19.9 wt.%) and CaO (0.91-2.73 wt.%) contents reflect significant fractional crystallization of mafic minerals and plagioclase during magmatic evolution.

The rare earth element signatures of the felsic suite further constrain the arc magmatic processes. Significant LREE enrichment (La/Sm_{pm} = 4.76-6.28) suggests substantial crustal involvement during magma genesis, whereas the strongly fractionated HREE patterns (Gd/Yb_{pm}= 2.71-5.33) suggest garnet retention in the parental melt (Kendrick and Yakymchuk, 2020). These REE characteristics, particularly the HREE fractionation, indicate magma generation at depths sufficient for garnet stability (>40 km), implying deep crustal or upper mantle melting conditions (Roberts et al., 2024). The combination of enriched LREE and fractionated HREE patterns, together with the negative Nb and Ti anomalies, supports a model of magma generation through partial melting of subduction-modified mantle material as opposed to just crustal contamination (Hollings & Wyman, 1999; Pearce, 1987). The strong negative Ti anomalies (Ti/Ti* = 0.03-0.24) suggest extensive fractionation of Ti-bearing phases, consistent with the evolution of calc-alkaline magmas under oxidizing conditions, typical of island arc settings. The intermediate and felsic samples share subduction-influenced geochemical signatures that are directly comparable to those of Phanerozoic accreted terranes such as the Cordillera of North America or Japan (Polat & Kerrich, 2001).

The representative intermediate and felsic Sm/Nd isotope samples yielded $\varepsilon Nd_{(2700\ Ma)}$ values of +2.10 to +2.42 and +1.53 to +2.56 with an estimated depleted mantle value $\varepsilon Nd_{(2700\ Ma)}$ (+3). The positive values are common in intra-oceanic settings and suggest minimal crustal interaction. These findings align with published values of Archean subduction-related lithologies from Polat (2009) and Henry et al. (1998).

These geochemical and isotope signatures collectively suggest that the Eagle River intermediate and felsic suite samples evolved through deep-sourced melting with partial melting processes typical of island arc magmatism. This closely aligns with the second tectonic

environment interpretation of Polat (2009) of the eastern part of the Wawa subprovince, where they identified an intra-oceanic island arc that displays greater compositional diversity, consisting primarily of plateau basalts to calc-alkaline basalts, andesites, dacites, and rhyolites, with minor but significant occurrences of adakites, magnesian andesites, and Nb-enriched basalts (Polat, 2009).

5.21 Eagle River Deformation and Kinematics

Detailed field mapping, stereonet projections, oriented thin sections, and grain-scale analysis delineate a complex structural framework that governs the evolution of the Eagle River property and provides insight into the larger Mishibishu greenstone belt. Stereonet data indicate a chlorite-defined, pervasive axial planar foliation north of the mine of 298°/72°NE, crosscut by a late, property-wide, northwest-trending normal fault of interest for this study. To the west of the mine, a more E-W trend of 265°/70°NE dominates. Throughout the property, a strongly pronounced stretching lineation in quartz veining is consistently observed to plunge down dip to the northeast. Fault-associated, chlorite-defined slicklines are typically vertical to sub-vertical, with only one horizontal orientation observed.

Field observations indicate a minimum of two significant ductile deformation events, accompanied by multiple, later brittle deformation events, most notably, parallel, property-wide normal faults that crosscut all structures, trending to the northwest. Several ductile kinematic features dominate the area, with the most common being Z folds, boudinaged and pinch and swell quartz veins, asymmetrical, upright, transposed isoclinal folds, and S and C fabrics observed in mylonite zones, coupled with anastomosing strain partitioning phenomena, all providing clear evidence for well evidenced bulk shortening deformation.

The Eagle River mine localized high strain outcrops, the 2-Zone and 8-Zone are hosted in the Eagle River deformation zone, a curved high strain, deformation corridor that mimics the larger Mishibishi deformation zone to the north and, interestingly, shares the same curved orientation as the Midcontinent rift-related, 1,200 km long Great Lakes tectonic zone to the south, within Lake Superior (Sims et al., 1980). Given that the GLTZ is 1600 m.y. younger, the spreading plates likely accommodated the same pathway that previous N-S accretion followed. Low- to medium-grained mylonite forms the localized Eagle River mine shear zones with recrystallized quartz and porphyroclasts of muscovite, fine-grained biotite, amphibole and networks of plagioclase that have not been fully recrystallized. At the outcrop scale, field observations and stereonet data suggest the Eagle River mine shear zones primarily trend E-W and dip at 75° to the NE. A pervasive, oblique to foliation, stretching lineation plunges down dip at approximately 75° to the NE (Figs. 4.18, 4.19, 4.20, 4.23, 4.24). This indicates dip slip kinematics with outcrop scale Z folds, boudinaged quartz veins, upright, isoclinal folds in quartz veins and S and C fabrics, indicating a horizontal component bearing dextral kinematics. The 2-Zone is observed to have more of a horizontal (transpressional) component and extends east outside the diorite host rock into a sulphide-rich tholeiitic basalt; the brittle nature of the diorite and overall rheological differences between lithologies could be the cause of strain deflection, causing a more horizontal orientation for the portion of the 2-Zone, which does curve towards the SSE at the eastern portion of the 2-Zone (Fig. 5.5).

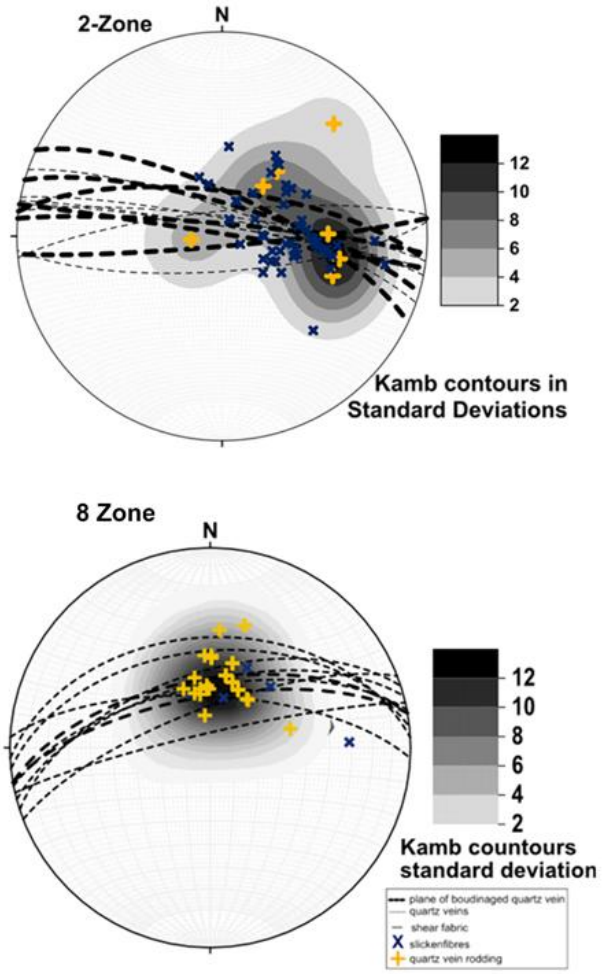

Fig. 5.5: Stereonets from the Eagle River mine's 2 and 8 shear zones.

Petrographic analysis of Zones 2 and 8 supports the field observations with a more detailed characterization. Oriented thin sections were used to infer shear sense kinematics by examining S and C fabric, porphyroclast tail direction, and way up direction. Numerous porphyroclast systems, predominantly plagioclase, display characteristic winged δ, α and θ morphologies. Some porphyroclasts have been flattened (θ), which suggests pure shear due to lack of volume change and principal stress of equal magnitude. Delta and sigma clasts with tails oriented north side up with dextral kinematics indicate transpressional deformation. Plagioclase

porphyroclast networks of up to ten per cluster serve as excellent strain markers and imply peak deformation temperatures were not high enough to fully recrystallize plagioclase. The consistent orientation of their asymmetric porphyroclast tails, combined with other shear sense indicators such as S-C fabrics, mica fish, quartz aggregate sigmoids, and asymmetrical micro-folds when corroborated with field-scale observations, implies the Eagle River deformation zone is of lower amphibolite metamorphic facies, characterized by north over south kinematics with a dextral reverse shear sense.

Lin and Jiang (2001) used an along-strike variation in strain and kinematics to define the movement in the direction of curved transpressional shear zones in the Superior craton. The review highlights how the angle of convergence dictates sinistral or dextral kinematics, which is highly relatable to the Eagle River's curved transpressional deformation zone. The kinematics of the Eagle River shear zones align with the work put forth by Sibson et al. (1988) on high-angle reverse faults and their association with Neoarchean, mesothermal gold deposits. The paper suggests that many Neoarchean gold-bearing shear zones are related to the reactivation of earlier normal faults during tectonic shortening.

SEM-supported petrographic analysis of the 8 Zone sheared quartz veins reveals gold chemistry is 80% Au and 20% silver and is preferentially located at or near the vein selvage, or in areas of higher strain, quartz shear bands. Galena was observed to be directly associated with Au. Other minerals such as zoisite, mica, biotite, chlorite, calcite, and siderite occur near Au mineralization (Figs. 4.40 & 4.41). Bands of tabular to acicular, subhedral barite were identified in the 8 Zone sheared quartz vein samples. Barite is a common byproduct of hydrothermal systems and can be useful for fingerprinting mineralization and timing. Work by Muir (2002) and Michibayashi (1995) on the characterization of the relatively nearby Hemlo gold deposit

found that Au ore contained 13% barite, and syngenetic banded barite was partially dissolved and transported during subsequent D_2 and D_3 shearing, making this a good opportunity for further research to better understand the nature of barite and how it relates to gold mineralization at Eagle River Mine (Fig. 4.42).

The deformation mechanism, dynamic recrystallization within quartz grains, occurs from the progressive rotation of subgrains and grain boundary migration, which is driven by stress and temperature gradients (Stipp et al., 2002). The dominant quartz microstructure observed in the Eagle River sheared quartz vein thin section suite is grain boundary migration (GBM) characterized by inequigranular, lobate grain boundaries, chessboard extinction, and many island grains (Figs. 4.44, 4.43). The conditions for crystal plasticity involve the accumulation of strain by intracrystalline processes, such as the movement of dislocations or linear lattice defects, and are driven by the motions of dislocations through the lattice controlled by the crystal structure and by the number of impurities and other lattice defects present (Stipp et al., 2002). Grain boundary migration and its relationship to diffusional mass transfer (DMT) are well documented by Knipe (1988). It suggests dislocation glide is the driver for GBM as grain boundaries migrate toward regions with higher dislocation density to reduce overall energy in the system, thus, creating strain energy gradients as dislocations accumulate in certain regions of quartz grains, they create areas of higher stored energy. This uneven distribution of dislocations leads to heterogeneous strain, which promotes selective grain boundary migration (Knipe, 1989). This produces various feedback mechanisms in shear zones, such as strain hardening when dislocations accumulate or softening when GBM-driven recrystallization occurs. Furthermore, dislocation glide becomes the dominant mechanism for common crustal minerals like quartz at around 400-500°C (Knipe, 1989; Stipp et al., 2002; Hirth & Tullis, 1991). Figure 5.6 shows

intragrain distortion in sheared quartz grains from the 2-Zone with dislocation creep interpreted as the driver.

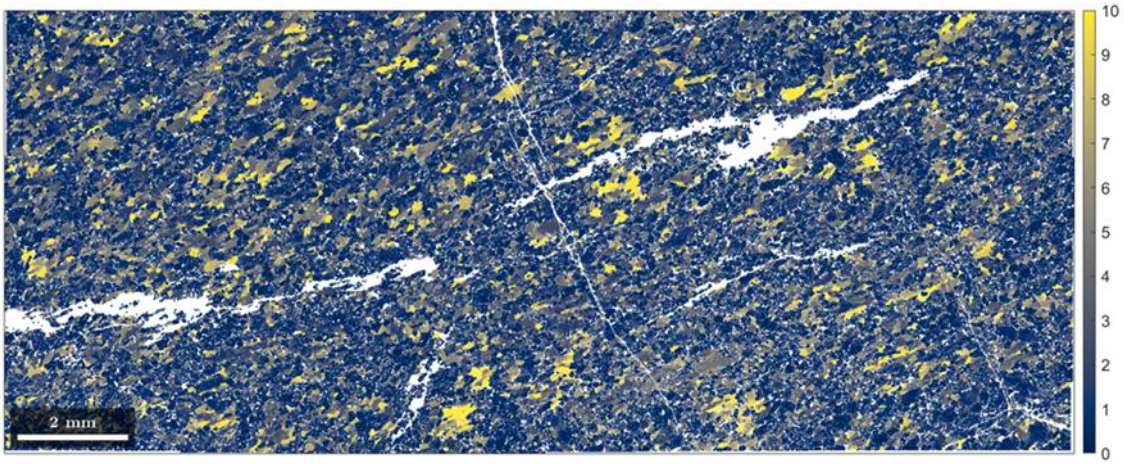

Fig. 5.6: Misorientation to mean maps showing (in yellow) quartz grain boundaries that are 10° different compared to grain boundaries in blue.

Zones 2 and 8 sheared quartz veins have been fully dynamically recrystallized. This suggests gold rich quartz veins were pre orogenic and emplaced within an earlier stress regime. This has two key consequences: first, the original veins were re-worked and rotated to form tabular, laminated quartz veins; and second, the classification and genetic interpretations that assume syn-kinematic vein emplacement risk misclassifying overprint geometry with primary ore-forming fluids. This suggests that localized shearing at the Eagle River deposit controlled the redistribution and exposure of pre-existing mineralization rather than syn-tectonic gold-endowed hydrothermal fluids. The work of (McDivitt et al., 2017) on the Renabie gold deposit, located in the northern tip of the Michipicoten greenstone belt within the Wawa subprovince, represents a similar shear-zone-hosted orogenic gold deposit, yet temporally distinct. The deposit shares the typical characteristics of Archean orogenic gold systems in the Superior craton, including gold-bearing laminated quartz veins localized within steep, brittle-ductile shear zones exhibiting oblique-reverse kinematics and well-defined ore plunges in greenschist- to amphibolite-grade

rocks, all features typically associated with orogenic systems (Goldfarb et al., 2005). However, multiple structural lines of evidence suggest that the principal mineralization event predates localized shear zone development with lenticular orebody geometry, shear-related fabrics, microstructures, and kinematic indicators that are overprinted during later transcurrent reactivation. Consequently, the Renabie gold deposit should be interpreted as a pre-orogenic vein system, mechanically reworked and concentrated by localized deformation.

The TitaniQ is a powerful tool for understanding deformation conditions, particularly the peak recrystallization temperature of quartz in crystal plastic shear zones, making it an excellent geothermometer. Based on the work of Wark and Watson (2006) and subsequent refinements by Thomas et al. (2010), the experiment utilizes the temperature-dependent substitution of titanium for silicon in quartz crystals. As temperature increases, quartz can accommodate more titanium in its crystal structure. Using EPMA data and the suggested calculations from Thomas et al. (2010) we found that 50% of temperature calculations fall within the range of 496-544° for the 2-Zone and 470-539° for the 8 Zone samples. Unfortunately, the margin of error of Ti wt. % for EMPA readings was high, and many were below the detection limit of 10 ppm. However, the results are reasonable and comparable to those of other greenschist- to lower amphibolite-facies rocks in Neoarchean orogenic gold deposits formed near the brittle-ductile transition. Groves (1993) suggested average mineralization temperatures for orogenic gold deposits within Archean cratons of 200 °C to 650 °C.

At the grain scale, EBSD mapping provided robust crystallographic orientation, grain size and morphology, deformation microstructures, and strain analysis data helped us better understand deformation history. The 2-Zone sheared quartz samples highlight a strong crystallographic preferred orientation showing basal and prism slip characteristics with distinct

outer ring asymmetrical girdle patterns [0001] along with oblique maxima concentrations and inclined girdles. However, patterns heavily lack symmetry, implying more than one ductile deformation event. The complementary [1120] and [1010] pole figures show high-intensity regions sometimes offset by about 30°, signifying two distinct patterns of misorientations indicative of non-coaxial strain (Fossen and Cavalcante, 2017). Previous work by Law (2014) suggests these characteristics are implicit in non-coaxial, triclinic flow geometry with peak deformation conditions at approximately 400-500°c. Furthermore, the misorientation-to-mean maps reveal high internal misorientations (>10°) and a non-uniform distribution of crystallographic axes that underscore the complex, non-coaxial deformation history (Aravadinou et al., 2022; Hunter et al., 2018; Savignano et al., 2016; Trouw et al., 2009; Tullis, 2014.; Ukar et al., 2016).

The 8-Zone sheared quartz vein EBSD mapping inverse pole figure data shows two distinct events. Bimodal, oblique maxima concentrations, inclined girdles, and asymmetric distributions suggest a non-coaxial deformation history. The activation of combined basal and prism slip systems suggests shear deformation with differing strain histories. Interestingly, Sample ER-22-8Z-H displays a more asymmetric [0001] pattern, indicating stronger non-coaxial deformation under different strain intensities or, potentially, different temperature conditions. The 8 Zone has higher g/pt gold values than the 2-Zone and a steeper stretching lineation, indicating higher pure shear compared to the 2-Zone.

Both 2-Zone and 8-Zone sheared quartz vein EBSD mapping results show evidence of non-coaxial deformation, with triclinic flow strain geometry. This refers to a complex flow regime where the strain axes and the rock rotate relative to each other, resulting in a non-symmetric deformation matrix (Passchier, 1988). This type of flow is characterized by the

instantaneous strain axes that do not align with the fabric lines throughout the deformation process, thus making it difficult to discern symmetrical patterns in misorientation concentrations as observed in EBSD pole figures (Fossen and Cavalcante, 2017; Lin et al., 2007; Passchier, 1988).

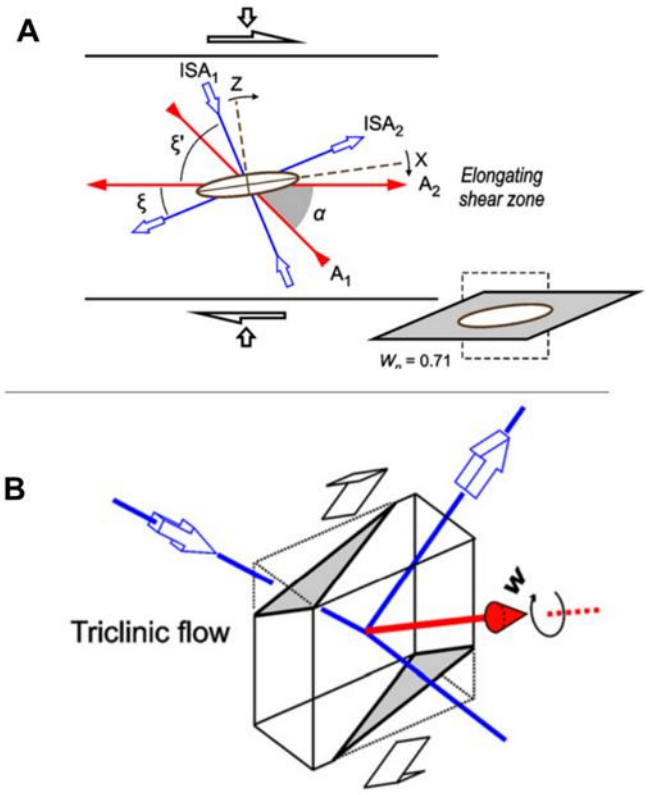

Fig. 5.8: A simplified sketch, modified from Xypolias (2010), shows the orientation of instantaneous flow elements and their angular relationships with a dextral, elongating shear zone. B: Simplified Triclinic flow model with vorticity vector oblique to all instantaneous stretching axes.

Using this point data technique, the CVA maxima from these samples captured evidence of two high-strain events. The 2-Zone maxima captured more of a synchronous pure shear-dominated transpressional signature. Interestingly, the 8 Zone, the highest Au grade bearing shear zone in the Eagle River deformation corridor, shows a composite signature where a simple shear component overprints a pure shear fabric, whereas the other sample, in proximity, presents a clear, independent, simple shear pattern (Fig. 5.9). This is interpreted as a pure shear-driven

event, characteristic of ductile, coaxial crustal thickening, followed by an independent direction parallel to the stretching lineation, indicative of both pure shear and simple shear elements, with one sample showing a pure shear signature and another exhibiting simple shear kinematics.

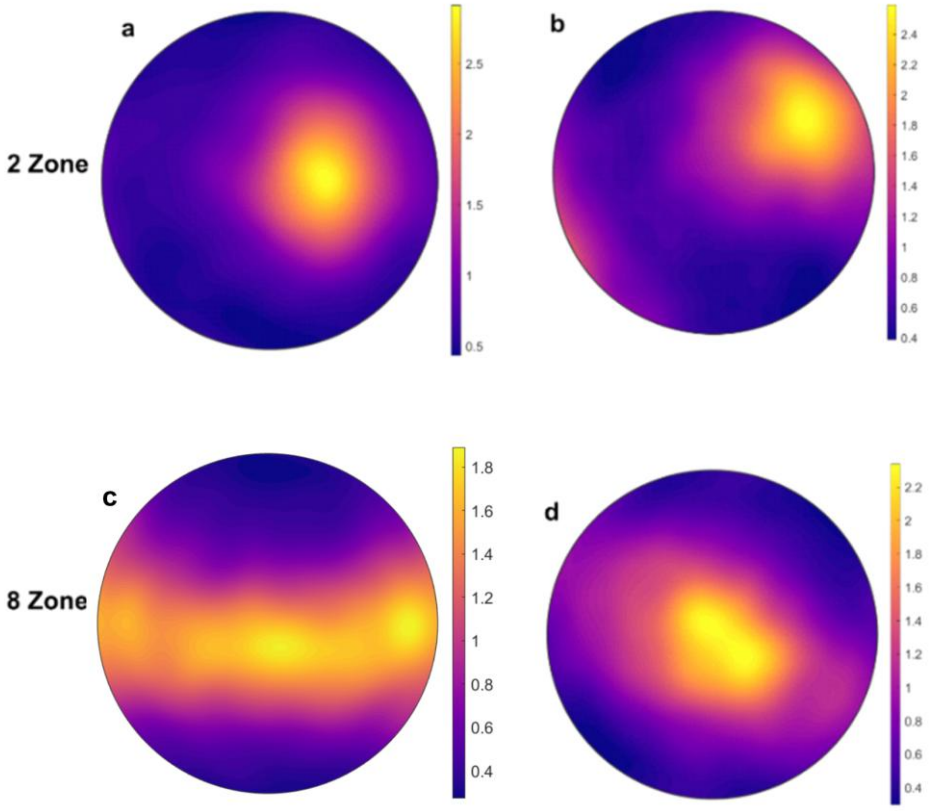

Fig. 5.9: CVA figures with 2-Zones showing a simple shear transpressional pattern and 8 Zones showing pure shear signature overprinting a simple shear pattern.

The complete structural data analysis of the Eagle River deformation zone suggests a crustal thickening event dominated by pure shear followed by a simple shear-related steady state, non-coaxial, triclinic flow deformation geometry with north side up, transpressional kinematics. The simple shear component has reverse, dextral kinematics. Quartz grains have been recrystallized through the deformation mechanism, grain boundary migration; this process is

driven by diffusion glide. Gold grains are remobilized through the crystal lattice of quartz as well as other impurities (sulphides) and swept to the selvage of quartz veins and veinlets. Other curved along-strike transpressional shear zones with triclinic symmetry are summarized by the work of Lin et al. (1998) and include the Roper Lake shear zone in the Canadian Appalachians, the currently active Alpine Fault in New Zealand and the Neoarchean Southern Knee Lake shear zone in the western Superior craton in Manitoba, Canada.

Non-coaxial deformation involves shearing where principal strain axes rotate relative to the material, creating complex strain arrays with multiple orientations, a heterogeneous stress field, variable permeability networks and dynamically orientated fluid pathways that open and close cyclically during progressive deformation (Fossen, 2010; Fossen and Cavalcante, 2017; Mole et al., 2022). In contrast, coaxial flow creates more uniform strain patterns, predictable fracture orientation and less complex fluid flow networks. Non-coaxial deformation helps create dynamic permeability through fractures, allowing fluid flow during extension, then sealing during compression. Mineral precipitation reduces fluid flow permeability and helps build pressure for the next failure cycle during the progressive deformation cycle, and areas of reduced stress become preferential fluid pathways (Fossen, 2010; Ma et al., 2023; Phillips and Powell, 2009; Sibson et al., 1988; Tavares Nassif et al., 2022). Triclinic deformation (three unequal axes), combined with non-coaxial flow, generates multiple intersecting fracture sets, structural irregularities that act as hydrothermal fluid traps, zones of dilation and compression that control fluid flow, and complex shortening-related fold geometry that create structural culminations (McDivitt et al., 2017; Tavares Nassif et al., 2022).

Neoarchean conditions likely provided a higher geothermal gradient, thus a more vigorous hydrothermal system (Sun et al., 2019). Komatiitic, TTG and sanukitoid magmatism

supplied both heat and sulphur-poor fluids, ideal for gold mobilization. Greenstone belt architecture helped create large-scale structural corridors for fluid flow, and a more primitive crustal composition helped create fewer competing metal phases (Groves et al., 2018). All these factors contributed to the "Goldilocks conditions" for gold mineralization in the Eagle River gold deposit.

Recent work on gold deposits in and around the nearby Michipicoten greenstone belt within the Wawa subprovince supports a discussion framework in which mineralization is best understood as the product of multiple overlapping magmatic, hydrothermal, and deformational events, as opposed to the typical orogenic gold deposit framework. This is indicated from the recent reinterpretation of the Magino deposit by Campos et al. (2024) and from the structural model developed for the Missanabie-Renabie district by McDivitt et al (2017), both of which show that early mineralizing processes were subsequently modified by later deformation events.

At Magino, Campos et al. (2024) provide strong evidence that the deposit is fundamentally an overprinted Archean intrusion-related gold deposit. Their work shows that the principal gold event was associated with emplacement of the ca. 2724 Ma Webb Lake stock intrusion, where pervasive biotite-phengite alteration and auriferous, recrystallized sugary quartz veins are host to the primary gold mineralization event. They further demonstrate that this early event predates the principal regional bulk ductile deformation with a relatively minor episode which introduced gold-bearing quartz-tourmaline-carbonate veins during deformation. This interpretation is important because it indicates that although gold deposits in the Wawa subprovince have many similarities, each has their unique fingerprint. Instead, the Magino deposit suggests evidence for an intrusion-related component, with later structural overprinting and remobilizing.

The Renabie district of the Wawa subprovince shares some similar characteristics, although McDivitt et al. (2017) argue that the auriferous laminated quartz veins of the Missanabie-Renabie gold mine and area were emplaced in brittle structures before regional ductile deformation, rather than forming as typical, syn-deformation fault-fill veins during active shearing. Early gold-bearing veins were subsequently stretched, reoriented, and remobilized into a later sinistral-reverse shearing event that defines the Renabie trend. The later shear zones then additional hydrothermal fluid flow, producing what the authors describe as hybrid deposits.

Together, these studies suggest that mineralization in the region is best interpreted through a poly phase, integrated model combining magmatism, early hydrothermal activity, deformation, and later hydrothermal fluid flow, as opposed to a single process or event

5.3 Eagle River Genesis

The genesis of the host rocks to the Eagle River gold deposit is supported by a new age for the Northern Diorite Pluton of 2720.60 ± 0.15 Ma, together with geochronological results reported by Wawrzonkowski (2024), who obtained ages for key intrusive units: Mine-host diorite at 2716.22 ± 0.41 Ma, Floating Heart Batholith at 2687.26 ± 0.42 Ma, Bowman Lake Batholith at 2658.35 ± 0.41 Ma, and the Central Pluton at 2656.38 ± 0.41 Ma. These intrusions were emplaced into 2.9–2.6 Ga mafic to felsic supracrustal rocks. Nymoen et al. (2025) proposed that magmatism in the Wawa Subprovince proceeded in three major volcanic cycles: (1) a spatially restricted mafic–ultramafic event at 2890–2880 Ma, (2) a 2750–2700 Ma bimodal cycle, and (3) a 2720–2650 Ma felsic-dominated event, followed by deposition of metasedimentary successions.

Calc alkaline rocks intruded mafic crust in an intra-oceanic terrane were later overprinted by shortening and fault inversion during regional convergence. Deformation became increasingly concentrated within the diorite host, where foliation, reverse shearing, mylonitic fabrics, and quartz veining developed together with structural pathways favourable for gold-bearing hydrothermal fluids. Continued deformation, folding and transposing earlier quartz veins into high-strain zones where gold was locally remobilized and concentrated along vein margins. The final overprint consists of late brittle north–south faulting, likely related to flexural stresses associated with curvature along the major regional deformation zones. Overall, the deposit records progressive structural reworking from extension to compression and transpression, with gold mineralization closely linked to strain localization, fluid flow, and quartz-vein redistribution.

Chapter 6: Conclusions

This study has investigated the Eagle River Neoarchean orogenic gold deposit through a multidisciplinary approach targeting its lithogeochemical footprint, kinematic history, and deformation mechanisms. By synthesizing field observations with analytical results from field mapping, lithogeochemistry, Sm/Nd isotope analysis, oriented petrography, EBSD mapping, CVA analysis and chlorite/titanite geothermometry, this research has enhanced our understanding of the formation processes and tectonic framework responsible for an Archean gold deposit.

The host rocks to the mine can be divided into two broad groups, tholeiitic and calc-alkaline. Eagle River mafic samples, basalts and gabbro are classified as tholeiitic with negative Nb and Ti anomalies, near flat to weakly fractionated LREE with (La/Sm_{pm} = 0.94-1.25), and HREE values that plot near flat to weakly fractionated with a Gd/Yb_{pm} ratio of (0.88 to 1.62). These REE signatures are similar to the modern-day Ontong Java plateau basalts. The Eagle River tholeiitic basalt Sm/Nd isotope values of $\varepsilon Nd_{T(2700)}$ range from +1.93 to +2.50, compared to a depleted mantle estimate of $\varepsilon Nd_{T(2700)}$ (+3). This data, coupled with field observations of near-mine pillow basalts, all suggest that the mafic samples likely formed in a primitive intra-oceanic, plateau setting.

The intermediate samples are calc-alkaline, comprised of diorite, andesites and granodiorites and have negative Nb and Ti anomalies with moderate LREE patterns (La/Sm_{pm} = 1.29-5.82) and fractionated HREE patterns of (Gd/Yb_{pm} = 0.70-4.28), suggesting a magmatic evolution dominated by fractional crystallization, driven by subduction-related processes with isotope values $\varepsilon Nd_{(2700\ Ma)}$ of +2.10 to +2.42. The felsic granite suite from the nearby post-

deformation TTG suites has negative Nb and Ti anomalies with significant LREE enrichment (La/Sm_{pm} = 4.76-6.28) and strongly fractionated HREE (Gd/Yb_{pm} = 2.71-5.33) and values of $\varepsilon Nd_{(2700\ Ma)}$ +1.53 - +2.56. This data supports a model of magma generation through partial melting of subduction-modified mantle material and correlates with Polat & Kerrich (2001), in the eastern Wawa subprovince, subduction-related, calc-alkaline rocks. Synthesized lithogeochemical data suggest an island arc interoceanic environment with calc-alkaline rocks intruding primitive, plume-related oceanic plateau rocks.3

The Eagle River deformation zone is a 4-kilometre, curved along-strike, brittle-ductile shear zone. The kinematics are characterized by anastomosing, north side up oblique slip and dextral, reverse transpression. The deformation corridor is associated with two ductile events: pure shear and a later simple shear event. The simple shear component has reverse, dextral kinematics. The Eagle River mine shear zones 2 and 8 are classified as non-coaxial deformation with triclinic flow geometry. Plagioclase occurs as fractured networks and provides a brittle contrast with increased space for hydrothermal endowment within the mine shear zones. Quartz has been dynamically recrystallized by the deformation mechanism, grain boundary migration and driven by diffuse mass transfer, within the dislocation creep regime. Gold grains, sulphides and other impurities are preferentially swept to and accumulate at the vein or veinlet salvage.

The results of this detailed study have several important implications regarding the structural framework, tectonic setting, and timing of the high-grade Eagle River gold deposit. The characteristics of the Eagle River orogenic gold deposit align with typical Archean orogenic gold models put forth by Groves et al. (1998) and Goldfarb and Groves (2015) on mesothermal, quartz vein hosted, orogenic gold deposits formed through subduction-related tectonic settings in

accretionary orogenic belts near the brittle ductile transition. However, it is unique that the Eagle River sheared quartz veins are fully recrystallized.

Lithogeochemistry and isotope results suggest genesis within an intra-oceanic environment. Plateau basalts have a relatively primitive arc REE signature, evolving to an arc-related signature. Pure shear followed by simple shear dominated right lateral transpression indicated within the Eagle River deformation zone aligns with accretionary tectonic models for the western Superior Province through the amalgamation and docking of various continental and oceanic terranes to form one solid craton, as suggested by Card (1990) and Percival et al. (2006). The transpressional component of the Eagle River deformation zone is interpreted to have helped create array networks and jogs that helped accommodate and trap gold-rich, hydrothermal fluids.

References

Arndt, N.T., 1994. Archean komatiites. In: Condie K.C. (Ed.), Archean Crustal Evolution. Elsevier, Amsterdam, pp. 11–44.

Bourdelle, F., Parra, T., Chopin, C., & Beyssac, O. (2013). A new chlorite geothermometer for diagenetic to low-grade metamorphic conditions. Contributions to Mineralogy and Petrology, 165(4), 723–735. https://doi.org/10.1007/s00410-012-0832-7

Card, K. D. (1990). A review of the Superior Province of the Canadian Shield, a product of Archean accretion. Precambrian Research, 48(1–2), 99–156. https://doi.org/10.1016/0301-9268(90)90059-Y

Callan, N. J., & Spooner, E. T. C. (1998a). Repetitive hydraulic fracturing and shear zone inflation in an Archean granitoid-hosted, ribbon-banded, Au-quartz vein system, Renabie area, Ontario, Canada. *Ore Geology Reviews*, *12*(4), 237–266. https://doi.org/10.1016/S0169-1368(98)00003-1

Campos, I. C., Lafrance, B., Sherlock, R., Dunbar, P., Mclaughlin, B., Kruse, S., Creaser, R., & Leung, D. D. V. (2024a). The Magino Gold Deposit, Ontario, Canada: An Overprinted Archean Intrusion-Related Gold Deposit. *Economic Geology*, *119*(7), 1563–1585. https://doi.org/10.5382/econgeo.5103

Champion, D. C., & Sheraton, J. W. (1997). Geochemistry and Nd isotope systematics of Archaean granites of the Eastern Goldfields, Yilgarn Craton, Australia: Implications for crustal growth processes. Precambrian Research, 83(1–3), 109–132. https://doi.org/10.1016/S0301-9268(97)00007-7

David, J. (1996a). Evolution of the Snow Lake portion of the Palaeoproterozoic Flin Flon and Kisseynew belts, Trans-Hudson Orogen, Manitoba, Canada. Precambrian Research, 80(1–2), 107–124. https://doi.org/10.1016/S0301-9268(96)00008-3

De Bresser, J., Ter Heege, J., & Spiers, C. (2001). Grain size reduction by dynamic recrystallization: Can it result in major rheological weakening? International Journal of Earth Sciences, 90(1), 28–45. https://doi.org/10.1007/s005310000149

Fossen, H. (2010). Structural Geology Textbook. *Cambridge University Press*. Chapters 2 & 3.

Fossen, H., & Cavalcante, G. C. G. (2017). Shear zones – A review. Earth-Science Reviews, 171, 434–455. https://doi.org/10.1016/j.earscirev.2017.05.002

Gagnon, É., Schneider, D. A., Kalbfleisch, T., Habler, G., & Biczok, J. (2016). Characterization of transpressive deformation in shear zones of the Archean North Caribou greenstone belt (NW Superior Province) and the relationship with regional metamorphism. Tectonophysics, 693, 261–276. https://doi.org/10.1016/j.tecto.2016.02.035

Goldfarb, R. J., Baker, T., Dubé, B., Groves, D. I., & Hart, C. J. R. (n.d.). Distribution, Character, and Genesis of Gold Deposits in Metamorphic Terranes.

Groves, D. I., & Phillips, G. N. (1987). The genesis and tectonic control on Archaean gold deposits of the Western Australian Shield—A metamorphic replacement model. Ore Geology Reviews, 2(4), 287–322. https://doi.org/10.1016/0169-1368(87)90009-6

Groves, D. I., Santosh, M., Goldfarb, R. J., & Zhang, L. (2018). Structural geometry of orogenic gold deposits: Implications for exploration of world-class and giant deposits. Geoscience Frontiers, 9(4), 1163–1177. https://doi.org/10.1016/j.gsf.2018.01.006

Hastie, E. C. G., Kontak, D. J., Lafrance, B., Petrus, J. A., Sharpe, R., & Fayek, M. (2023). Evaluating Geochemical Discriminants in Archean Gold Deposits: A Superior Province Perspective with an Emphasis on the Abitibi Greenstone Belt. Economic Geology, 118(1), 123–155. https://doi.org/10.5382/econgeo.4979

Hedenquist, J. W. (Ed.). (2005). Economic geology: One hundredth anniversary volume: 1905-2005. Society of Economic Geologists, Inc.

Henry, P., Stevenson, R. K., & Gariépy, C. (1998a). Late Archean Mantle Composition and Crustal Growth in the Western Superior Province of Canada: Neodymium and Lead Isotopic Evidence from the Wawa, Quetico, and Wabigoon Subprovinces. Geochimica et Cosmochimica Acta, 62(1), 143–157. https://doi.org/10.1016/S0016-7037(97)00324-4

Henry, P., Stevenson, R. K., & Gariépy, C. (1998b). Late Archean Mantle Composition and Crustal Growth in the Western Superior Province of Canada: Neodymium and Lead Isotopic Evidence from the Wawa, Quetico, and Wabigoon Subprovinces. Geochimica et Cosmochimica Acta, 62(1), 143–157. https://doi.org/10.1016/S0016-7037(97)00324-4

Hoare, L., Klaver, M., Saji, N. S., Gillies, J., Parkinson, I. J., Lissenberg, C. J., & Millet, M.-A. (2020). Melt chemistry and redox conditions control titanium isotope fractionation during magmatic differentiation. Geochimica et Cosmochimica Acta, 282, 38–54. https://doi.org/10.1016/j.gca.2020.05.015

Hollings, P. (1999). Trace element systematics of ultramafic and mafic volcanic rocks from the 3Ga North Caribou greenstone belt, northwestern Superior Province. Precambrian Research, 93(4), 257–279. https://doi.org/10.1016/S0301-9268(98)00088-6

Hollings, P. (2002). Archean Nb-enriched basalts in the northern Superior Province. Lithos, 64(1–2), 1–14. https://doi.org/10.1016/S0024-4937(02)00154-8

Hollings, P., & Kerrich, R. (2006). Light rare earth element-depleted to enriched basaltic flows from 2.8 to 2.7 Ga greenstone belts of the Uchi Subprovince, Ontario, Canada. Chemical Geology, 227(3–4), 133–153. https://doi.org/10.1016/j.chemgeo.2005.09.010

Hollings, P., & Wyman, D. (1999). Trace element and Sm–Nd systematics of volcanic and intrusive rocks from the 3 Ga Lumby Lake Greenstone belt, Superior Province: Evidence for Archean plume–arc interaction. Lithos, 46(2), 189–213. https://doi.org/10.1016/S0024-4937(98)00062-0

Hunter, N. J. R., Weinberg, R. F., Wilson, C. J. L., & Law, R. D. (2018). A new technique for quantifying symmetry and opening angles in quartz c-axis pole figures: Implications for interpreting the kinematic and thermal properties of rocks. Journal of Structural Geology, 112, 1–6. https://doi.org/10.1016/j.jsg.2018.04.006

Huston, D., & Gutzmer, J. (Eds.). (2023). Isotopes in Economic Geology, Metallogenesis and Exploration. Springer International Publishing. https://doi.org/10.1007/978-3-031-27897

Iacopini, D., Passchier, C. W., Koehn, D., & Carosi, R. (2007). Fabric attractors in general triclinic flow systems and their application to high-strain shear zones: A dynamical system approach. Journal of Structural Geology, 29(2), 298–317. https://doi.org/10.1016/j.jsg.2006.10.002

Jochum, K.P., Arndt, N.T., Hofman, A.W., 1991. Nb–Th–La in komatiites and basalts: constraints on komatiites petrogenesis and mantle evolution. Earth Planet. Sci. Lett. 107, 272–289.

Keller, R. J. (1989). The evolution of the Mishibishu greenstone belt, near Wawa, Ontario. University of Windsor Department of Geology.

Kerr, A. C. (2015). Oceanic Plateaus. In J. Harff, M. Meschede, S. Petersen, & J. Thiede (Eds.), Encyclopedia of Marine Geosciences (pp. 1–15). Springer Netherlands. https://doi.org/10.1007/978-94-007-6644-0

Kerrich, R., Polat, A., & Xie, Q. (2008). Geochemical systematics of 2.7 Ga Kinojevis Group (Abitibi), and Manitouwadge and Winston Lake (Wawa) Fe-rich basalt–rhyolite

associations: Back arc rift oceanic crust? Lithos, 101(1–2), 1–23. https://doi.org/10.1016/j.lithos.2007.07.009

Ketchum, J. W. F., Ayer, J. A., Van Breemen, O., Pearson, N. J., & Becker, J. K. (2008). Pericontinental Crustal Growth of the Southwestern Abitibi Subprovince, Canada—U-Pb, Hf, and Nd Isotope Evidence. Economic Geology, 103(6), 1151–1184. https://doi.org/10.2113/gsecongeo.103.6.1151

Kretz, R. (1983). Symbols for rock-forming minerals. American Mineralogist, Volume 68, pages 277–279.

Lafleche, M.R., Dupuy, C., Dostal, J., 1992. Tholeiitic volcanic rocks of the Late Archean Blake River Group, southern Abitibi greenstone belt: origin and geodynamic implications. Can. J. Earth Sci. 29, 1448–1458.

Lin, S., & Jiang, D. (2001). Using along-strike variation in strain and kinematics to define the movement direction of curved transpressional shear zones: An example from northwestern Superior Province, Manitoba. Geology, 29(9), 767. https://doi.org/10.1130/0091-7613(2001)

Lin, S., Jiang, D., & Williams, P. F. (2007). Importance of differentiating ductile slickenside striations from stretching lineations and variation of shear direction across a high-strain zone. Journal of Structural Geology, 29(5), 850–862. https://doi.org/10.1016/j.jsg.2006.12.006

Lloyd, G. E., & Freeman, B. (1994). Dynamic recrystallization of quartz under greenschist conditions. Journal of Structural Geology, 16(6), 867–881. https://doi.org/10.1016/0191-8141(94)90151-1

Ma, C., Marsh, J., Lodge, R. W. D., Tamosauskas, M., Sherlock, R., Lafrance, B., Thurston, P., & Ayer, J. (2023). Formation of Archean greenstone belts: Insights from an assemblage-scale study in the western Superior craton. Precambrian Research, 395, 107150. https://doi.org/10.1016/j.precamres.2023.107150

Martin, H., Smithies, R. H., Rapp, R., Moyen, J.-F., & Champion, D. (2005). An overview of adakite, tonalite–trondhjemite–granodiorite (TTG), and sanukitoid: Relationships and some implications for crustal evolution. Lithos, 79(1–2), 1–24. https://doi.org/10.1016/j.lithos.2004.04.048

McDivitt, J. A., Lafrance, B., Kontak, D. J., & Robichaud, L. (2017). The Structural Evolution of the Missanabie-Renabie Gold District: Pre-orogenic Veins in an Orogenic Gold Setting

and Their Influence on the Formation of Hybrid Deposits. Economic Geology, 112(8), 1959–1975. https://doi.org/10.5382/econgeo.2017.4536

Michels, Z. D., Kruckenberg, S. C., Davis, J. R., & Tikoff, B. (2015). Determining vorticity axes from grain-scale dispersion of crystallographic orientations. Geology, 43(9), 803–806. https://doi.org/10.1130/G36868.1

Mole, D. R., Thurston, P. C., Marsh, J. H., Stern, R. A., Ayer, J. A., Martin, L. A. J., & Lu, Y. J. (2021). The formation of Neoarchean continental crust in the south-east Superior Craton by two distinct geodynamic processes. Precambrian Research, 356, 106104. https://doi.org/10.1016/j.precamres.2021.106104

Muir, T. L. (2002). The Hemlo gold deposit, Ontario, Canada: Principal deposit characteristics and constraints on mineralization. Ore Geology Reviews, 21(1–2), 1–66. https://doi.org/10.1016/S0169-1368(02)00066-5

Nania, L., Montomoli, C., Iaccarino, S., & Carosi, R. (2024). Calcite fabric development in calc-mylonite during progressive shallowing of a shear zone: An example from the South Tibetan Detachment system (Kali Gandaki valley, Central Himalaya). Tectonophysics, 872, 230176. https://doi.org/10.1016/j.tecto.2023.230176

Nymoen, K. G., Mole, D. R., Thurston, P. C., Tinkham, D. K., Marsh, J. H., & Stern, R. A. (2025). Crustal evolution and architecture of the Wawa Subprovince, Superior Province: Insights from zircon U-Pb-Hf-O isotopes and geochemistry. Precambrian Research, 418, 107705. https://doi.org/10.1016/j.precamres.2025.107705

Passchier, C., & Coelho, S. (2006). An outline of shear-sense analysis in high-grade rocks. Gondwana Research, 10(1–2), 66–76. https://doi.org/10.1016/j.gr.2005.11.016

Passchier, C. W. (1983). The reliability of asymmetric c-axis fabrics of quartz to determine sense of vorticity. Tectonophysics, 99(1), T9–T18. https://doi.org/10.1016/0040-1951(83)90166

Passchier, C. W. (1988). Analysis of deformation paths in shear zones. Geologische Rundschau, 77(1), 309–318. https://doi.org/10.1007/BF01848692

Passchier, C. W., & Simpson, C. (1986). Porphyroclast systems as kinematic indicators. Journal of Structural Geology, 8(8), 831–843. https://doi.org/10.1016/0191-8141(86)90029-5

Passchier, C. W., & Williams, P. R. (1996a). Conflicting shear sense indicators in shear zones: the problem of non-ideal sections. Journal of Structural Geology, 18(10), 1281–1284. https://doi.org/10.1016/S0191-8141(96)00051

Pearce, J. A. (1987). An expert system for the tectonic characterization of ancient volcanic rocks. Journal of Volcanology and Geothermal Research, 32(1–3), 51–65. https://doi.org/10.1016/0377-0273(87)90036-9

Pearce, J. A. (2008). Geochemical fingerprinting of oceanic basalts with applications to ophiolite classification and the search for Archean oceanic crust. Lithos, 100(1–4), 14–48. https://doi.org/10.1016/j.lithos.2007.06.016

Pearce, J. A., Harris, N. B. W., & Tindle, A. G. (1984). Trace Element Discrimination Diagrams for the Tectonic Interpretation of Granitic Rocks. Journal of Petrology, 25(4), 956–983. https://doi.org/10.1093/petrology/25.4.956

Percival, J. A., & McGrath, P. H. (1986). Deep crustal structure and tectonic history of the Northern Kapuskasing Uplift of Ontario: An integrated petrological‐geophysical study. Tectonics, 5(4), 553–572. https://doi.org/10.1029/TC005i004p00553

Phillips, G. N., & Powell, R. (2009). Formation of gold deposits: Review and evaluation of the continuum model. Earth-Science Reviews, 94(1–4), 1–21. https://doi.org/10.1016/j.earscirev.2009.02.002

Phillips, N. J., & Ji, S. (2021). Constraining the ductile deformation mechanisms of garnet across pressure-temperature space. Journal of Structural Geology, 148, 104356. https://doi.org/10.1016/j.jsg.2021.104356

Polat, A. (2009). The geochemistry of Neoarchean (ca. 2700Ma) tholeiitic basalts, transitional to alkaline basalts, and gabbros, Wawa Subprovince, Canada: Implications for petrogenetic and geodynamic processes. Precambrian Research, 168(1–2), 83–105. https://doi.org/10.1016/j.precamres.2008.03.008

Polat, A., & Kerrich, R. (1999). Formation of an Archean tectonic mélange in the Schreiber‐Hemlo greenstone belt, Superior Province, Canada: Implications for Archean subduction‐accretion process. Tectonics, 18(5), 733–755. https://doi.org/10.1029/1999TC900032

Polat, A., & Kerrich, R. (2001). Geodynamic processes, continental growth, and mantle evolution recorded in late Archean greenstone belts of the southern Superior Province, Canada. Precambrian Research, 112(1–2), 5–25. https://doi.org/10.1016/S0301-9268(01)00168-1

Polat, A., Kerrich, R., & Wyman, D. A. (1998). The late Archean Schreiber–Hemlo and White River–Dayohessarah greenstone belts, Superior Province: Collages of oceanic plateaus,

oceanic arcs, and subduction–accretion complexes. Tectonophysics, 289(4), 295–326. https://doi.org/10.1016/S0040-1951(98)00002

Polat, A., Kerrich, R., & Wyman, D. A. (1999). Geochemical diversity in oceanic komatiites and basalts from the late Archean Wawa greenstone belts, Superior Province, Canada: Trace element and Nd isotope evidence for a heterogeneous mantle. Precambrian Research, 94(3–4), 139–173. https://doi.org/10.1016/S0301-9268(98)00110-7

Polat, A., Longstaffe, F., Weisener, C., Fryer, B., Frei, R., & Kerrich, R. (2012). Extreme element mobility during transformation of Neoarchean (ca. 2.7 Ga) pillow basalts to a Paleoproterozoic (ca. 1.9 Ga) paleosol, Schreiber Beach, Ontario, Canada. Chemical Geology, 326–327, 145–173. https://doi.org/10.1016/j.chemgeo.2012.07.018

Prior, D., Mariani, E., & Wheeler, J. (2010). EBSD in the Earth Sciences: Applications, Common Practice, and Challenges. In Electron Backscatter Diffraction in Materials Science (pp. 345–360). https://doi.org/10.1007/978-0-387-88136-226

Ross, P.-S., & Bédard, J. H. (2009). Magmatic affinity of modern and ancient subalkaline volcanic rocks determined from trace-element discriminant diagrams. Canadian Journal of Earth Sciences, 46(11), 823–839. https://doi.org/10.1139/E09-054

Sage, R. P., Lightfoot, P. C., & Doherty, W. (1996a). Bimodal cyclical Archean basalts and rhyolites from the Michipicoten (Wawa) greenstone belt, Ontario: Geochemical evidence for magma contributions from the asthenospheric mantle and ancient continental lithosphere near the southern margin of the Superior Province. Precambrian Research, 76(3–4), 119–153. https://doi.org/10.1016/0301-9268(95)00020-8

Sibson, R. H. (1977). Fault rocks and fault mechanisms. Journal of the Geological Society, 133(3), 191–213. https://doi.org/10.1144/gsjgs.133.3.0191

Sibson, R. H., Robert, F., & Poulsen, K. H. (1988). High-angle reverse faults, fluid-pressure cycling, and mesothermal gold-quartz deposits. Geology, 16(6), 551. https://doi.org/10.1130/0091-7613(1988)

Sims, P. K., Card, K. D., Morey, G. B., & Peterman, Z. E. (1980). The Great Lakes tectonic zone—A major crustal structure in central North America. Geological Society of America Bulletin, 91(12), 690. https://doi.org/10.1130/0016-7606(1980)

Stipp, M., Stünitz, H., Heilbronner, R., & Schmid, S. M. (2002). Dynamic recrystallization of quartz: Correlation between natural and experimental conditions. Geological Society, London, Special Publications, 200(1), 171–190.

StraboSpot Software (2023). (Version 2) [Mobile app]. https://www.strabospot.org

Street, Y. (2022). Eagle River Mine Report. SRK Consulting (Canada) Inc.

Sun, S., & McDonough, W. F. (1989). Chemical and isotopic systematics of oceanic basalts: Implications for mantle composition and processes. Geological Society, London, Special Publications, 42(1), 313–345. https://doi.org/10.1144/GSL.SP.1989.042.01.19

Sylvester, P. J., Attoh, K., & Schulz, K. J. (1987). Tectonic setting of late Archean bimodal volcanism in the Michipicoten (Wawa) greenstone belt, Ontario. Canadian Journal of Earth Sciences, 24(6), 1120–1134. https://doi.org/10.1139/e87-109

Thomas, J. B., Bruce Watson, E., Spear, F. S., Shemella, P. T., Nayak, S. K., & Lanzirotti, A. (2010). TitaniQ under pressure: The effect of pressure and temperature on the solubility of Ti in quartz. Contributions to Mineralogy and Petrology, 160(5), 743–759. https://doi.org/10.1007/s00410-010-0505-3

Thomas, J. B., Watson, E. B., Spear, F. S., & Wark, D. A. (2015). TitaniQ recrystallized: Experimental confirmation of the original Ti-in-quartz calibrations. Contributions to Mineralogy and Petrology, 169(3), 27. https://doi.org/10.1007/s00410-015-1120-0

Thurston, P. C. (2002). Autochthonous development of Superior Province greenstone belts? Precambrian Research, 115(1–4), 11–36. https://doi.org/10.1016/S0301-9268(02)00004

Tikoff, B., & Greene, D. (1997). Stretching lineations in transpressional shear zones: An example from the Sierra Nevada Batholith, California. Journal of Structural Geology, 19(1), 29–39. https://doi.org/10.1016/S0191-8141(96)00056-9

Tullis, J. (1992). Dislocation creep regimes in quartz aggregates. Journal of Structural Geology, Vol. 14, No. 2, pp. 145 to 159, 1992.

Turek, A., Sage, R. P., & Schmus, W. R. V. (1992). Advances in the U–Pb zircon geochronology of the Michipicoten greenstone belt, Superior Province, Ontario. Canadian Journal of Earth Sciences, 29(6), 1154–1165. https://doi.org/10.1139/e92-093

Turek, A., Sage, R. P., & Schmus, W. R. V. (1992b). Advances in the U–Pb zircon geochronology of the Michipicoten greenstone belt, Superior Province, Ontario. Canadian Journal of Earth Sciences, 29(6), 1154–1165. https://doi.org/10.1139/e92-093

Turek, A., Smith, P. E., & Schmus, W. R. V. (1982). Rb–Sr and U–Pb ages of volcanism and granite emplacement in the Michipicoten belt—Wawa, Ontario. Canadian Journal of Earth Sciences, 19(8), 1608–1626. https://doi.org/10.1139/e82-138

Ukar, E., Laubach, S. E., & Marrett, R. (2016). Quartz c-axis orientation patterns in fracture cement as a measure of fracture opening rate and a validation tool for fracture pattern models. Geosphere, 12(2), 400–438. https://doi.org/10.1130/GES01213.1

Wang, Q., Okudaira, T., & Shigematsu, N. (2024). Dominant slip systems of quartz under lower amphibolite-facies conditions identified from microstructures and CPOs in quartz phenocrysts. Journal of Structural Geology, 182, 105106. https://doi.org/10.1016/j.jsg.2024.105106

Wark, D. A., & Watson, E. B. (2006). TitaniQ: A titanium-in-quartz geothermometer. Contributions to Mineralogy and Petrology, 152(6), 743–754. https://doi.org/10.1007/s00410-006-0132-1

Wawrzonkowski, P. (2024). Geology, geochemistry and alteration of the Eagle River Au-deposit near Wawa, Ontario. Department of Geology, Lakehead University.

Winchester, J. A., & Floyd, P. A. (1977). Geochemical discrimination of different magma series and their differentiation products using immobile elements. Chemical Geology, 20, 325–343. https://doi.org/10.1016/0009-2541(77)90057-2

Wyman, D. A., Cassidy, K. F., & Hollings, P. (2016). Orogenic gold and the mineral systems approach: Resolving fact, fiction and fantasy. Ore Geology Reviews, 78, 322–335. https://doi.org/10.1016/j.oregeorev.2016.04.006

Wyman, D., Hollings, P., Hinz, S., & Boucher, C. (2024). Archean high-Mg magmas: Their significance for continental growth at Archean cratonic margins. Precambrian Research, 409, 107445. https://doi.org/10.1016/j.precamres.2024.107445

Zane, A., & Weiss, Z. (1998). A procedure for classifying rock-forming chlorites based on microprobe data. Rendiconti Lincei, 9(1), 51–56. https://doi.org/10.1007/BF02904455

Appendix A:

Litho-Geochemistry Data

Appendix B:

Eagle River Petrography

Appendix A: Lithogeochemistry

Sample	ER-22-30	ER-22-40	ER-22-88	ER-22-91	ER-22-92	ER-22-94	ER-22-97	ER-22-103	ER-22-104	ER-22-105	ER-22-112	ER-22-115
SiO_2	48.7	47.3	48.2	48.3	49	50.5	50.2	49.9	47.2	48.9	50.5	50.4
TiO_2	0.67	0.67	1.24	0.65	2.92	1.13	0.67	1	0.58	0.7	0.66	2.07
Al_2O_3	15.9	15.9	15.45	13.6	13.85	13.8	15.35	15.15	15.5	14.9	14.3	12.45
Fe_2O_3	10.75	10.4	14.5	11.6	16.55	14.2	10.15	12.45	10.55	11.3	10.7	16.7
MnO	0.18	0.16	0.2	0.19	0.24	0.23	0.17	0.2	0.17	0.19	0.17	0.36
MgO	7.43	8.81	7.34	10.6	5.05	6.84	8.27	6.86	10.05	8.8	8.72	4.01
CaO	11.75	12.35	10.55	11.5	8.81	9.27	11.25	9.78	9.77	10.25	10.5	6.09
Na_2O	2.34	1.68	1.87	1.38	2.23	1.82	1.7	2.33	2.62	2.62	1.75	2.87
K_2O	0.27	0.19	0.22	0.29	0.19	0.51	1.34	0.22	0.17	0.35	0.47	0.46
P_2O_5	0.04	0.04	0.07	0.03	0.37	0.1	0.05	0.09	0.03	0.04	0.04	0.35
LOI	2.43	3.83	2.19	2.14	0.54	1.28	1.83	2.21	2.44	1.84	1.7	2.82
Sum	100.49	101.44	101.88	100.39	99.78	99.72	101.06	100.23	99.19	99.97	99.59	98.61
Cr	183	687	240	732	52	107	338	165	724	498	414	23
Co	44	47	51	56	38	50	44	45	53	47	44	41
Ni	92	175	105	198	40	70	109	81	206	138	101	18
Rb	12.6	6.4	13.8	20.7	2	24.5	73.6	16.4	4.1	10.3	23.1	15
Sr	167	199	180.5	119	120.5	142	227	193	84.1	128.5	125.5	154.5
Cs	0.6	0.44	1.26	1.14	0.16	1.15	1.43	0.77	0.73	0.69	1.3	1.25
Ba	37.3	36.5	81.3	127	19.8	80.4	263	124.5	36.9	52.5	91.2	151.5
Sc	38	30	47	34	35	39	38	37	23	27	41	37
V	260	232	416	274	423	342	254	301	222	251	271	188
Ta	0.1	0.1	0.2	0.1	0.5	0.2	0.2	0.3	0.1	0.2	0.1	0.5
Nb	1.7	1.87	3.09	2.12	8.19	3.65	3.09	3.76	1.52	1.8	2.05	6.86
Zr	38	41	75	39	175	70	66	82	33	38	54	149
Hf	1.16	1.16	2.12	1.13	4.46	2.02	1.77	2.31	1.02	1.24	1.6	4.16
Th	0.21	0.22	0.38	1.32	0.9	0.51	2.39	1.54	0.19	0.4	0.41	1.34
U	0.05	0.1	0.11	0.23	0.24	0.17	0.33	0.28	0.06	0.2	0.13	0.35
Y	14.4	13	24	15.1	49.8	24.1	14.6	23.3	11	14.4	17	53.1
La	2.7	2.5	4.2	4.3	9.9	5.1	9.6	6.2	2.7	2.6	3.2	10.2
Ce	2	2.3	2	1.8	1.8	1.9	1.8	1.8	1.3	1.8	2	2.3
Pr	1	0.99	1.6	1.44	3.94	2.21	2.49	2.21	0.88	1.27	1.31	4.24
Nd	5.5	5.1	7.8	5.2	20.9	9.4	10.1	10.2	4	4.9	5.9	19.4
Sm	1.72	1.6	3.02	1.92	6.11	2.68	1.8	2.7	1.19	1.78	1.66	6.18
Eu	0.57	0.64	0.98	0.59	1.85	1.01	0.71	0.86	0.51	0.76	0.62	2.04
Gd	2.03	2.12	3.49	2.15	7.57	3.7	2.65	3.58	2.05	2.09	2.21	7.64
Tb	0.42	0.36	0.6	0.36	1.29	0.6	0.41	0.57	0.31	0.5	0.45	1.34
Dy	2.55	2.28	4.13	2.76	8.54	3.99	2.58	3.77	2.17	2.76	2.84	8.95
Ho	0.6	0.5	0.96	0.56	1.76	0.89	0.61	0.87	0.43	0.76	0.67	1.98
Er	1.8	1.79	2.92	1.67	5.81	2.57	1.53	2.5	1.38	1.75	1.83	5.68
Tm	0.22	0.22	0.43	0.21	0.75	0.39	0.22	0.36	0.17	0.38	0.28	0.84
Yb	1.47	1.44	2.65	1.54	5.07	2.43	1.42	2.45	1.3	1.75	1.93	5.12
Lu	0.17	0.22	0.42	0.25	0.67	0.43	0.25	0.4	0.17	0.46	0.27	0.91
Cu	448	48	200	153	50	126	94	156	31	122	35	92
Zn	84	78	106	82	133	109	67	102	90	90	59	215
Mo	0.5	0.5	0.5	0.5	0.5	0.5	0.5	0.5	0.5	0.5	0.5	1
Ag	0.25	0.25	0.25	0.25	0.25	0.25	0.25	0.5	0.25	0.25	0.25	0.25
Tl	0.05	0.01	0.03	0.02	0.01	0.02	0.04	0.01	0.01	0.01	0.05	0.01
Pb	2	14	2	2	2	3	3	2	1	1	3	3
Sn	0.25	0.25	0.5	0.5	1.4	0.7	0.5	1	0.25	0.5	0.5	2.5
Sb	0.06	0.05	0.025	0.025	0.025	0.025	0.025	0.025	0.025	0.025	0.025	0.07
Ga	18.6	17.1	21.4	13.9	22.9	18.2	15.9	18.3	14.1	14.8	16	22.6
Ge	1.6	1.6	1.8	1.8	1.8	1.8	1.8	1.8	1.9	1.9	2	2
As	1	1.3	1.5	0.4	0.2	0.5	0.05	1	0.4	1.3	0.4	2.3
W	3.4	4.2	0.6	0.7	1.3	0.5	0.25	0.7	1.3	0.7	0.9	1.6
Bi	0.12	0.06	0.01	0.03	0.03	0.01	0.01	0.04	0.02	0.005	0.02	0.05

Sample	ER-22-42	ER-22-98	ER-22-114	ER-22-108	ER-22-71	ER-22-93	ER-22-113	ER-22-90	ER-22-100	ER-22-101	ER-22-111	ER-22-95	ER-22-96
SiO_2	48.3	46.3	49.6	48.2	63.00	53.00	54.70	74.2	77.8	72.3	73.4	67.5	68.5
TiO_2	0.83	1.04	1.52	0.61	0.86	0.59	1.19	0.09	0.02	0.23	0.22	0.41	0.38
Al_2O_3	16.35	16	13.45	17.8	14.25	10.30	15.75	14.8	13.65	14.95	15.25	16.3	16.5
Fe_2O_3	11.45	13.7	13.75	9.18	6.33	7.68	8.33	2.26	1.02	2.17	1.72	3.59	3.54
MnO	0.19	0.24	0.28	0.13	0.08	0.16	0.11	0.06	0.04	0.05	0.02	0.07	0.07
MgO	6.05	9.13	5.65	7.49	4.40	9.45	4.33	0.21	0.07	0.57	0.57	1.29	0.98
CaO	10.75	8.56	8.18	11.8	5.34	12.40	8.46	1.06	0.52	1.61	2.01	2.01	2.61
Na_2O	3.19	2.45	2.67	1.58	5.29	2.51	3.33	4.21	5.12	4.19	5.89	4.55	4.35
K_2O	0.37	0.43	1.47	0.03	0.66	0.07	0.18	4.07	1.72	3.86	0.84	3.01	3.28
P_2O_5	0.05	0.07	0.17	0.05	0.21	0.12	0.31	0.04	0.01	0.1	0.06	0.18	0.17
LOI	3.29	2.3	1.78	3.92	0.75	2.41	2.34	0.53	0.8	1.03	0.73	1.69	1.01
Sum	100.86	100.29	98.61	100.87	101.23	98.86	99.11	101.74	100.81	101.21	100.78	100.79	101.63
Cr	81.0	279.0	124.0	406.0	236.0	1040.0	107.0	11.0	8.0	13.0	22.0	27.0	16.0
Co	40.0	56.0	55.0	41.0	18.0	43.0	27.0	0.5	0.5	2.0	3.0	6.0	5.0
Ni	69.0	153.0	60.0	136.0	102.0	272.0	81.0	0.5	1.0	2.0	2.0	3.0	4.0
Rb	15.6	26.7	60.2	0.8	19.2	0.9	5.8	123.5	109.0	107.5	21.5	76.3	90.9
Sr	162.0	182.5	234.0	168.5	215.0	163.0	488.0	310.0	163.0	325.0	386.0	470.0	600.0
Cs	0.7	0.7	2.2	0.3	0.7	0.0	0.4	3.4	4.7	2.1	1.5	1.6	2.6
Ba	65.5	79.6	525.0	6.0	112.0	26.0	56.0	1730.0	348.0	1045.0	289.0	1250.0	1655.0
Sc	34.0	29.0	40.0	19.0	16.0	24.0	20.0	2.0	2.0	3.0	2.0	3.0	3.0
V	259.0	320.0	355.0	214.0	136.0	159.0	217.0	2.5	9.0	21.0	33.0	63.0	39.0
Ta	0.1	0.2	0.7	0.1	0.5	0.2	0.5	1.8	1.5	1.2	0.3	0.5	0.5
Nb	2.0	2.8	10.8	1.1	11.2	3.2	8.9	14.0	12.4	10.5	3.2	8.0	8.4
Zr	46.0	64.0	137.0	28.0	181.0	72.0	160.0	136.0	77.0	149.0	119.0	228.0	242.0
Hf	1.2	2.0	3.3	1.0	4.2	1.8	3.8	3.7	3.1	4.5	3.2	5.9	6.2
Th	0.2	0.6	4.0	0.2	3.2	0.9	1.9	19.2	10.9	13.8	1.5	17.6	18.1
U	0.1	0.1	0.5	0.1	1.6	0.2	0.5	1.9	3.0	2.0	0.6	1.9	1.8
Y	15.8	22.7	28.6	10.0	19.6	10.5	21.9	9.0	10.9	10.6	4.8	10.6	9.7
La	3.0	5.2	19.7	1.8	29.7	9.8	18.8	41.4	9.2	24.6	6.9	50.5	60.9
Ce	1.9	1.6	1.8	1.4	1.3	1.2	1.6	83.8	20.8	48.4	15.0	104.0	114.5
Pr	1.1	1.9	5.7	0.7	9.0	3.3	6.6	9.1	2.3	5.7	1.8	11.6	13.2
Nd	5.9	7.8	22.9	3.7	33.8	14.5	25.9	28.3	7.3	18.5	6.3	36.1	41.6
Sm	1.9	2.7	5.1	1.1	6.3	2.6	5.1	3.9	1.8	3.3	1.1	5.7	6.3
Eu	0.7	0.8	1.4	0.6	1.5	0.8	1.4	0.8	0.3	0.8	0.5	1.5	1.4
Gd	2.3	3.4	5.0	1.3	4.9	2.8	4.7	2.4	1.5	2.5	1.1	3.5	3.5
Tb	0.4	0.5	0.9	0.2	0.7	0.4	0.7	0.3	0.3	0.4	0.1	0.4	0.4
Dy	2.9	3.8	5.1	1.9	3.9	2.5	3.7	1.6	1.9	2.1	0.8	2.2	1.9
Ho	0.7	0.9	1.1	0.4	0.7	0.4	0.9	0.3	0.3	0.4	0.2	0.4	0.4
Er	1.7	2.5	3.1	1.1	2.0	1.1	2.2	0.7	0.9	1.0	0.6	1.1	0.9
Tm	0.2	0.4	0.5	0.2	0.3	0.2	0.4	0.1	0.2	0.2	0.1	0.2	0.1
Yb	1.7	2.3	2.7	1.3	1.8	1.0	1.9	0.8	0.9	1.1	0.5	1.0	0.7
Lu	0.3	0.4	0.5	0.2	0.3	0.2	0.4	0.1	0.2	0.2	0.1	0.2	0.1
Cu	55.0	80.0	116.0	77.0	22.0	5.0	84.0	1.0	1.0	2.0	3.0	4.0	7.0
Zn	115.0	120.0	93.0	57.0	40.0	75.0	84.0	70.0	16.0	51.0	23.0	59.0	83.0
Mo	0.5	0.5	1.0	0.5	1.0	0.5	1.0	2.0	0.5	0.5	0.5	0.5	0.5
Ag	0.3	0.3	0.3	0.3	0.3	0.3	0.3	0.3	0.3	0.3	0.3	0.3	0.3
Tl	0.0	0.0	0.0	0.0	0.1	0.0	0.0	0.2	0.1	0.1	0.0	0.0	0.2
Pb	5.0	2.0	3.0	2.0	1.0	3.0	3.0	26.0	12.0	28.0	2.0	11.0	21.0
Sn	0.3	0.6	1.1	0.3	1.0	0.5	0.9	2.3	2.9	1.8	0.6	1.3	1.4
Sb	0.1	0.0	0.0	0.0	0.1	0.1	0.0	0.0	0.0	0.0	0.0	0.0	0.0
Ga	18.8	17.2	18.6	16.2	15.8	10.3	20.0	18.2	18.6	19.3	21.1	20.5	20.1
Ge	2.0	2.3	2.3	2.3	1.2	1.3	1.3	1.2	1.7	1.3	0.9	1.2	1.1
As	1.2	0.1	1.0	0.4	0.3	0.4	1.3	0.1	0.1	0.2	0.3	0.1	0.1
W	4.1	0.7	1.1	0.7	0.7	1.0	0.7	0.7	1.0	0.5	2.3	0.7	0.3
Bi	0.1	0.0	0.0	0.0	0.0	0.0	0.0	0.1	0.2	0.0	0.0	0.0	0.0

Sample	ER-22-99	ER-22-109	ER-22-25	ER-22-29	ER-22-54	ER-22-107	ER-22-50	ER-22-52	ER-22-58	ER-22-59	ER-22-110	ER-22-116
SiO_2	68	56.6	60	57.5	62	57.3	69.4	67.8	67.3	65.4	62.60	56.30
TiO_2	0.42	0.93	0.92	0.88	0.71	0.77	0.66	0.64	0.67	0.7	0.78	1.22
Al_2O_3	16.45	14.55	15.3	14.75	14.6	15.65	15.05	14.8	15.25	16.2	15.85	17.15
Fe_2O_3	3.71	5.44	8.07	8.12	6.1	7.59	3.73	4.05	4.27	4.2	5.61	7.97
MnO	0.07	0.06	0.05	0.06	0.08	0.14	0.05	0.06	0.06	0.05	0.08	0.11
MgO	1.02	7.46	4.15	0.54	4.61	5.83	2.27	2.27	2.36	2.17	3.17	3.93
CaO	2.73	7	4.61	15.75	4.43	7.08	1.65	2.17	5.14	3.68	6.34	6.88
Na_2O	4.38	5.75	3.9	0.38	4.61	3.45	5.49	5.04	4.74	5.68	3.73	3.76
K_2O	3.34	0.26	1.16	0.03	0.63	0.51	1.1	1.4	0.44	0.56	0.42	0.83
P_2O_5	0.2	0.3	0.24	0.25	0.19	0.16	0.16	0.15	0.17	0.15	0.25	0.36
LOI	0.75	1.12	2.15	2.76	2.69	1.94	2.2	2.29	1.04	1.42	1.38	1.89
Sum	101.29	99.57	100.63	101.2	100.73	100.5	101.82	100.74	101.51	100.29	100.27	100.49
Cr	38.0	413.0	128.0	68.0	172.0	206.0	59.0	47.0	61.0	48.0	116.0	82.0
Co	6.0	20.0	36.0	3.0	16.0	30.0	10.0	11.0	11.0	12.0	18.0	25.0
Ni	4.0	222.0	82.0	22.0	105.0	145.0	40.0	39.0	42.0	35.0	61.0	79.0
Rb	104.5	6.6	38.0	0.9	17.9	14.4	28.1	31.1	9.3	12.3	9.6	23.2
Sr	573.0	284.0	286.0	1460.0	296.0	373.0	155.0	172.5	338.0	345.0	367.0	475.0
Cs	3.5	0.4	1.2	0.1	0.4	0.7	0.8	1.1	0.6	0.6	1.2	8.6
Ba	1400.0	66.6	249.0	16.0	132.0	121.5	251.0	369.0	166.5	253.0	115.0	311.0
Sc	4.0	16.0	13.0	13.0	12.0	17.0	9.0	8.0	9.0	8.0	11.0	15.0
V	65.0	155.0	125.0	183.0	109.0	175.0	85.0	84.0	91.0	89.0	121.0	187.0
Ta	0.5	0.5	0.7	0.5	0.4	0.4	0.6	0.6	0.6	0.8	0.6	0.6
Nb	7.7	8.6	10.4	9.9	6.0	6.8	9.3	8.9	9.4	10.2	8.9	9.8
Zr	207.0	151.0	231.0	145.0	136.0	136.0	229.0	212.0	214.0	242.0	169.0	166.0
Hf	5.2	3.7	5.8	3.5	3.0	3.2	5.6	4.9	5.5	6.1	4.1	3.7
Th	17.6	2.0	3.5	2.1	1.7	1.4	4.5	4.0	3.1	4.9	2.5	0.8
U	1.6	0.6	0.9	0.7	0.4	0.3	0.5	1.0	0.4	0.9	0.5	0.2
Y	9.8	14.9	20.1	21.1	11.5	16.4	13.4	14.3	14.3	14.9	15.6	21.8
La	56.2	12.6	23.0	79.6	14.4	12.6	23.0	19.4	22.1	19.2	19.6	16.4
Ce	107.5	35.3	50.0	147.0	32.0	31.4	47.1	40.7	42.5	45.1	45.6	42.2
Pr	11.8	5.2	6.4	15.8	4.1	4.5	5.4	5.2	5.1	5.8	6.3	6.2
Nd	38.3	21.5	27.7	60.4	17.0	17.4	20.8	20.6	20.2	22.9	22.8	26.8
Sm	5.4	4.7	5.8	8.7	3.2	3.9	4.1	4.0	3.8	4.0	4.8	6.0
Eu	1.4	1.3	1.4	1.6	0.9	1.2	1.0	1.0	1.0	0.8	1.3	1.9
Gd	3.3	3.9	5.3	6.2	2.8	3.5	3.0	3.3	3.2	3.4	3.7	4.8
Tb	0.4	0.6	0.7	0.8	0.4	0.5	0.4	0.5	0.5	0.4	0.6	0.7
Dy	2.2	3.0	4.1	4.3	2.4	3.0	2.6	2.7	2.7	2.8	3.0	4.1
Ho	0.4	0.6	0.8	0.9	0.4	0.7	0.6	0.5	0.5	0.5	0.6	0.9
Er	0.9	1.6	2.3	2.4	1.4	1.8	1.5	1.4	1.5	1.7	1.5	2.2
Tm	0.1	0.3	0.3	0.3	0.2	0.3	0.2	0.2	0.2	0.2	0.3	0.3
Yb	0.9	1.4	1.9	1.7	1.1	1.5	1.3	1.2	1.3	1.4	1.4	1.9
Lu	0.2	0.3	0.3	0.2	0.2	0.3	0.1	0.2	0.2	0.2	0.3	0.3
Cu	6.0	2.0	5.0	2.0	1.0	25.0	3.0	5.0	2.0	2.0	4.0	69.0
Zn	86.0	24.0	43.0	12.0	37.0	64.0	40.0	61.0	25.0	30.0	51.0	81.0
Mo	0.5	0.5	0.5	1.0	0.5	2.0	0.5	1.0	0.5	0.5	1.0	1.0
Ag	0.3	0.3	0.3	0.3	0.3	0.3	0.3	0.3	0.3	0.3	0.3	0.3
Tl	0.5	0.0	0.0	0.0	0.0	0.0	0.0	0.0	0.0	0.0	0.0	0.1
Pb	20.0	1.0	3.0	6.0	2.0	3.0	3.0	11.0	3.0	3.0	3.0	3.0
Sn	1.5	0.9	1.0	1.6	2.4	0.8	0.6	1.0	0.8	1.2	0.9	0.9
Sb	0.0	0.3	0.1	0.2	0.1	0.0	0.0	0.1	0.1	0.0	0.0	0.0
Ga	20.6	16.4	20.7	32.4	18.7	18.6	18.6	17.8	21.0	22.2	19.0	21.1
Ge	1.3	1.5	1.2	2.4	1.2	1.2	0.9	1.1	1.1	1.3	1.1	1.3
As	0.2	0.8	1.2	4.0	0.3	0.5	0.5	1.1	0.5	0.7	0.2	0.1
W	0.5	1.0	1.0	0.9	1.2	0.7	2.0	2.8	0.5	0.7	0.7	0.7
Bi	0.0	0.0	0.0	0.0	0.0	0.0	0.0	0.1	0.0	0.0	0.0	0.0

Appendix B

Petrography

Name: Eagle River Petrography

Start Date: 2022-09-01

End Date: 2025-09-0

Purpose of Study: Economic Research

Polish Description: Standard polish thin section

Instrument Type: Optical Microscopy

Instrument Brand: Zeiss

Instrument Model: Axioscope

University: Lakehead University

Laboratory: Archean Deformation

Area of Interest: microstructure and lithological characterization

GPS Datum: NAD83/UTM Zone 14N

Magnetic Declination: -13.86

Percentage Calculation Method: Qualitative Estimate

Mineralogy Method: Optical

Sample: ER-22-RB-120
Location: Northern Diorite (616202.9E 5316432.3N)

Full thin-section scan of ER-22-RB-116 (Mine Diorite) XPL 5x.

Lithology: Quartz Diorite

Minerals:

Mineral	(%)	Grain_size_mm	Occurrence	Habit_Texture	Alteration
Plagioclase	50	up to 2	Matrix + porphyroblasts	Subhedral, polysynthetic twinning	Sericite; zoisite/clinozoisite
Quartz	20	mostly fine; minor >0.5	Matrix + ribbons	Subhedral, undulose extinction	Blue quartz present
Hornblende	10	up to 1.5	Patchy grains	Subhedral	Partly replaced by chlorite
Orthoclase	10	up to 1.5	Porphyroblasts	Pervasively sericitized	Sericite pervasive
Biotite	5	up to 1 x 2	Matrix flakes	Tabular, subhedral blades	Replaced by chlorite
Chlorite	1	fine	Replacing biotite/amphibole	Anhedral masses	Secondary
Epidote	2.5	fine	Veins + patches	Anhedral aggregates	Secondary
Calcite	0.5	fine	Veins	Anhedral	Secondary
Zoisite/Clinozoisite	0.5	fine	Patches/veins; Plag replacement	Anhedral aggregates	Secondary

Sample: ER-22-RB-116
Location: Mine Diorite (616060.5E, 5315413.9N)

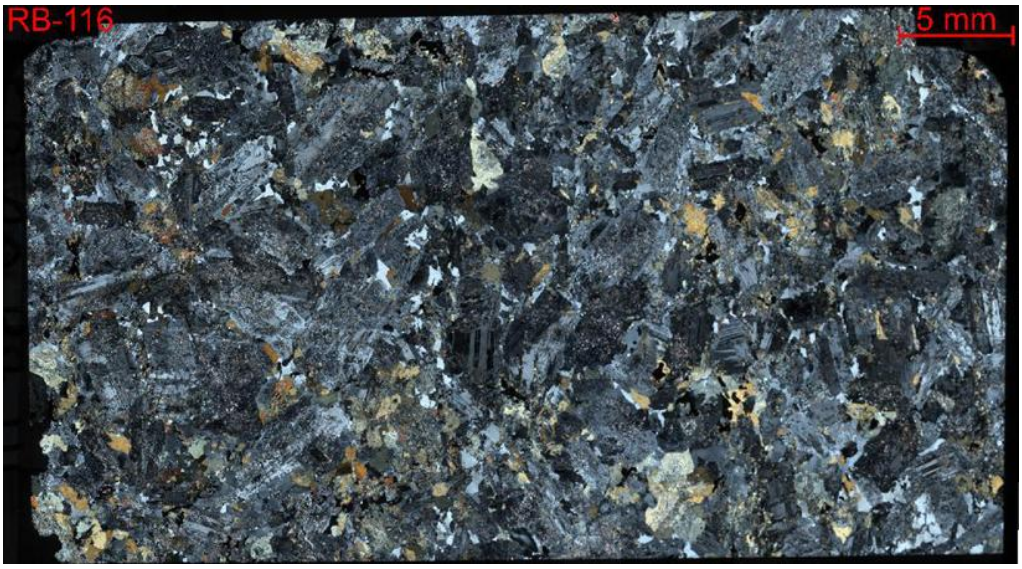

Full thin-section scan of ER-22-RB-116 (Mine Diorite) XPL 5x.

Lithology: Diorite/Gabbroic Diorite

Minerals:

Mineral	%	Grain Size (mm)	Occurrence	Habit	Alteration	Notes
Plagioclase	55	up to 2	Matrix + porphyroblasts	Subhedral, polysynthetic twinning	Sericite; zoisite/clinozoisite	Porphyroblasts of andesine
Quartz	5	mostly fine; minor >0.5	Matrix + ribbons	Subhedral, undulose extinction	Blue quartz grains present	Instances of blue quartz
Hornblende	10	up to 1.5	Patchy grains	Subhedral	Partly replaced by chlorite	Uralitic overprint local
Orthoclase	5	up to 1.5	Porphyroblasts	Pervasively sericitized	Sericite pervasive	K-feldspar
Biotite	5	up to 1	Matrix flakes	Tabular, subhedral blades	Replaced by chlorite	Pleochroic
Chlorite	6	fine	Replacing biotite/amphibole	Anhedral, tabular	Secondary	Widespread replacement
Sericite	3	very fine	Replacing feldspars	Micaceous aggregates	Secondary	Pervasive in Kfs/Plag
Zoisite/Clinozoisite	2	fine	Patches/veins; Plag replacement	Anhedral aggregates	Secondary	Saussurite assemblage
Epidote	2	fine	Veins + patches	Anhedral aggregates	Secondary	-
Calcite	1	fine	Veins	Anhedral	Secondary	Carbonate

Sample: ER-22-RB-98
Location: Dyke Lake area (618389.6E, 5314588.4N)

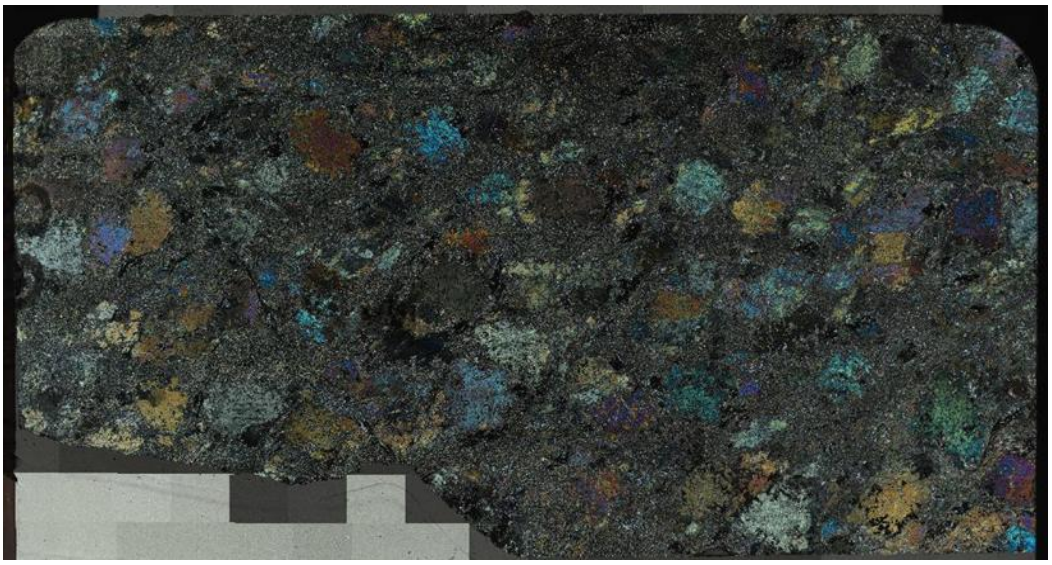

Full thin-section scan of ER-22-RB-116 XPL 5x.

Lithology: Gabbro

Texture: Phaneritic, porphyritic

Minerals:

Mineral	(%)	Grain Size (mm)	Occurrence	Habit_Texture	Alteration	Notes
Plagioclase	55	up to 2	Matrix + porphyroblasts	Subhedral, polysynthetic twinning	Zoisite/Clinozoisite	Porphyroblasts of andesine
Hornblende	10	up to 2	Patchy porphyroblasts	Anhedral grains	Partly replaced by chlorite	Porphyroblasts patchy
Clinopyroxene	15	up to 2	Replacing olivine	Coarse-grained	-	CPX replacing olivine
Actinolite	5	up to 1	Matrix + replacement	Tabular, anhedral	Replaced by chlorite	Medium to coarse
Olivine	5	up to 2	Relict grains	Anhedral	Partly to fully replaced by CPX	CPX pseudomorphs common
Chlorite	10	0.2mm	Replacing mafic phases	Anhedral masses	Secondary	Replaces hornblende/actinolite
Epidote	3	0.2mm	Alteration patches/veins	Anhedral aggregates	Secondary	Includes zoisite/clinozoisite
Calcite	2	0.2mm	Veins + patches	Anhedral	Secondary	Carbonate alteration

Sample: ER-22-RB-95
Location: Bowman Lake Batholith (619029.5E, 5316601.8N)

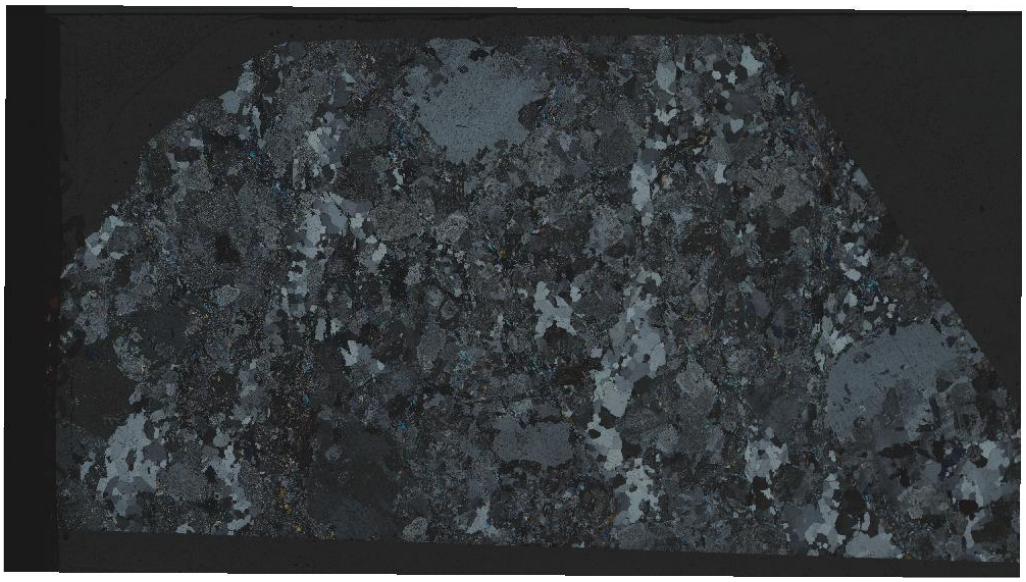

Full thin-section scan of sample ER-22-RB-95. XPL; 5x

Lithology: Granite (TTG)

Minerals:

Mineral	(%)	Grain Size (mm)	Occurrence	Habit	Alteration	Notes
Plagioclase	40	1.00	Matrix + phenocrysts	Subhedral, zoned	Saussuritized locally	Oligoclase-Andesine
Quartz	30	0.5-3	Interstitial + ribbons	Anhedral to subhedral	-	Undulose extinction common
K-feldspar	20	1-5	Phenocrysts + interstitial	Subhedral, perthitic	Sericitized rims	Microcline > orthoclase
Biotite	5	0.5-2	Matrix flakes	Subhedral laths	Chloritized locally	Pleochroic brown-green
Hornblende	2	0.5-2	Matrix	Subhedral	Partly chloritized	Calcic amphibole
Epidote	1	fine	Accessory + veins	Anhedral aggregates	Late	From plagioclase alteration
Titanite	1	0.1-0.5	Accessory	Subhedral wedges	-	On Fe-Ti oxides
Magnetite	0.5	0.1-0.5	Accessory	Anhedral	-	With titanite
Ilmenite	0.5	0.1-0.5	Accessory	Anhedral	-	Minor

Sample: ER-22-RB-89
Location: Dyke Lake area (E617209.0E, N5315107.1N)

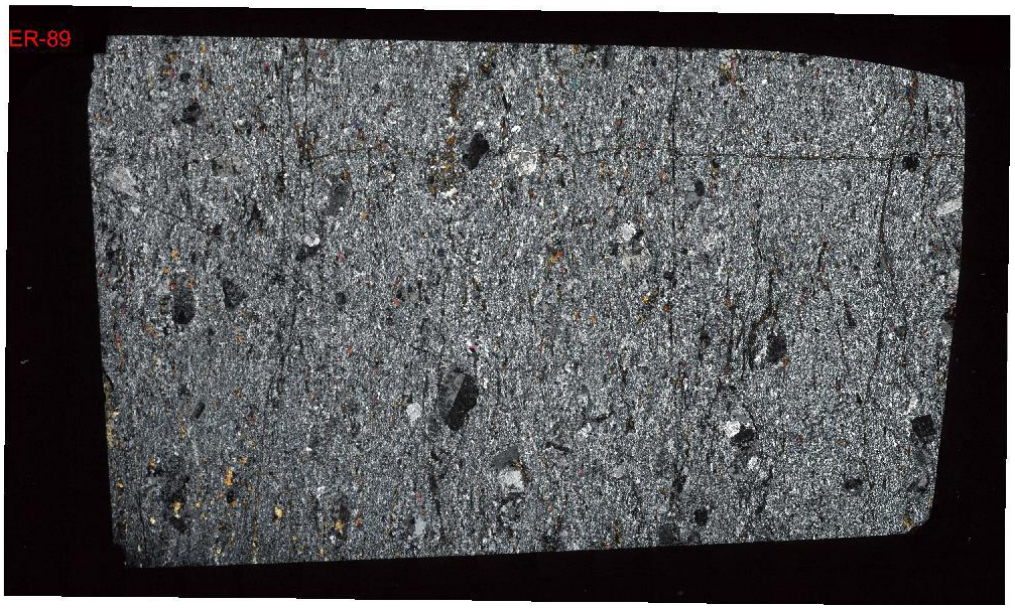

Full thin-section scan of sample ER-22-RB-89. XPL; 5x

Lithology: Andesite (porphyritic)

Minerals:

Mineral	%	Grain Size (mm)	Occurrence	Habit	Alteration	Notes
Groundmass	40	very fine	Matrix	Microlitic plagioclase + minor quartz	-	Intergranular
Quartz	15	fine to 0.5	Matrix + sparse grains	Subhedral	-	
Sanidine	10	up to 3	Phenocryst	Subhedral, Carlsbad twins	-	K-feldspar
Orthoclase	10	up to 2	Phenocryst	Subhedral porphyroblasts	Sericitized	K-feldspar
Hornblende	5	up to 1	Phenocryst	Euhedral to subhedral	Chloritized	
Clinopyroxene	5	fine	Matrix	Subhedral	Chlorite + amphibole replacement	Augitic
Biotite	2.5	up to 0.5	Matrix	Subhedral laths	-	
Epidote	5	very fine	Disseminated + fractures	Anhedral aggregates	Late	
Calcite	2.5	-	Disseminated + fractures	Anhedral	Late	

Sample: ER-22-RB-52
Location: Northern diorite (47.990357E, -85.437116N)

Full thin-section scan of sample ER-22-RB-52. XPL; 5x

Lithology: Diorite

Minerals:

Mineral	%	Grain Size (mm)	Occurrence	Habit_Texture	Alteration	Notes
Plagioclase	50	03-Jan	Matrix + phenocrysts	Subhedral, zoned	Saussuritized cores	An35-55 typical
Hornblende	20	1-3	Matrix + phenocrysts	Subhedral to euhedral	Chlorite along cleavages	Magnesiohornblende common
Biotite	8	0.5-2	Matrix	Subhedral laths	Chloritization rims	Pleochroic brown-green
K-feldspar	8	0.5-3	Interstitial + phenocrysts	Subhedral, perthitic locally	Sericite	Orthoclase to microcline
Quartz	6	0.2-1	Interstitial	Anhedral	-	Accessory to minor
Clinopyroxene	3	0.5-2	Relict	Subhedral	Hornblende + chlorite	Diopsidic to augitic
Epidote	3	fine	Veins + patches	Anhedral aggregates	Late	From plagioclase saussuritization
Titanite	1	0.1-0.5	Accessory	Subhedral wedges	-	On ilmenite/magnetite
Magnetite	1	0.1-0.5	Accessory	Anhedral	-	With titanite

Sample: ER-22-RB-117 (oriented)

Location: Birch Vein Area (616202.9E 5316432.3N)

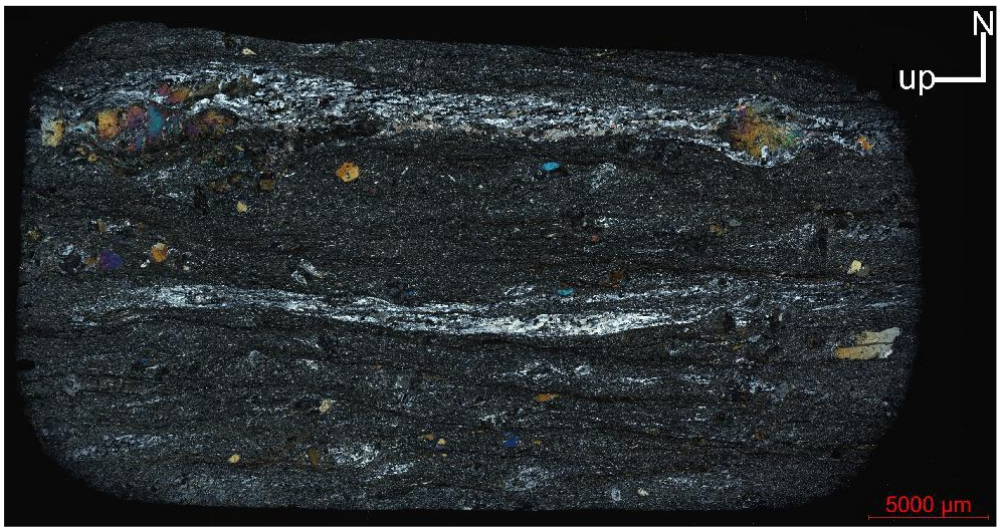

Fill thin section scan of ER-22-RB-117; 5x XPL

Lithology: Andesite (flow)

Very fine-grained microlitic to cryptocrystalline groundmass dominated by plagioclase and biotite, and larger-grained hornblende up to 1 mm, and accessory oxides; sparse plagioclase porphyroblasts are variably replaced by epidote. Primary magmatic flow banding—expressed by compositional layering and microlite shape-preferred orientation—served as the principal rheological contrast later exploited by narrow quartz veinlets. Within veins, quartz exhibits undulose extinction and dynamic recrystallization dominated by bulging and subgrain rotation, forming fine polygonal grains; grain boundary migration is subordinate. Subtle dextral asymmetry in quartz sigmoids occurs locally. Epidote is pervasive along plagioclase rims, fractures, and twins, locally forming quartz–epidote selvages adjacent to veins; biotite remains largely stable with minor chloritization.

2 Zone

Sample: ER-22-2Z-C

Location: Zone 2 – Sheared quartz vein

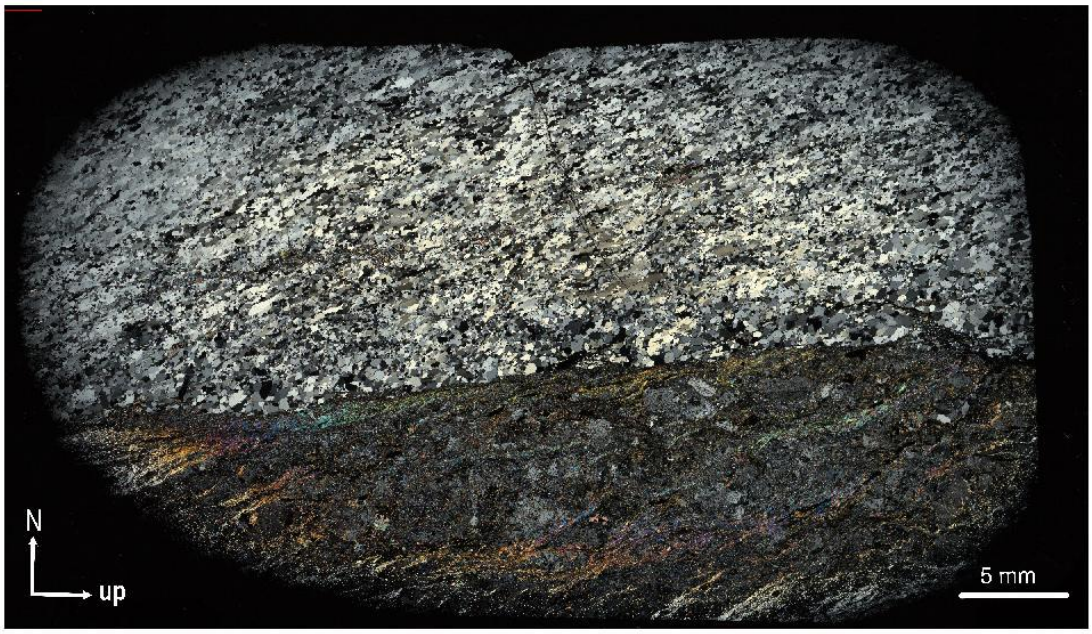

Fill thin section scan of ER-22-RB-C; 5x XPL

Sample ER-22-2Z-C is a medium-grained mylonite derived from diorite. The rock exhibits a well-developed mylonitic foliation with C'-type shear bands. Dynamically recrystallized quartz forms elongate ribbon grains and finer-grained arrays arranged in a sheared network pattern, with grain size increasing toward the mylonitic fabric. Plagioclase occurs as a fractured grain network. The mineral assemblage comprises quartz, plagioclase, biotite, and hornblende as primary phases, with epidote, zoisite, titanite (sphene), zircon, apatite, and opaques as accessory minerals. Alteration is characterized by the presence of muscovite and chlorite, with localized chloritization occurring along shear bands. Microstructural features

include quartz ribbons with undulose extinction, mica fish, and evidence of dynamic recrystallization via grain-boundary migration. Array patterns are prominent in the finer quartz domains. Brittle north-south fractures crosscut the mylonitic fabric. Kinematic indicators record the north-side-up and south-side-down shear senses.

Sample: ER-22-2Z-E

Location: Zone 2 channel sample, sheared quartz veins and mylonite

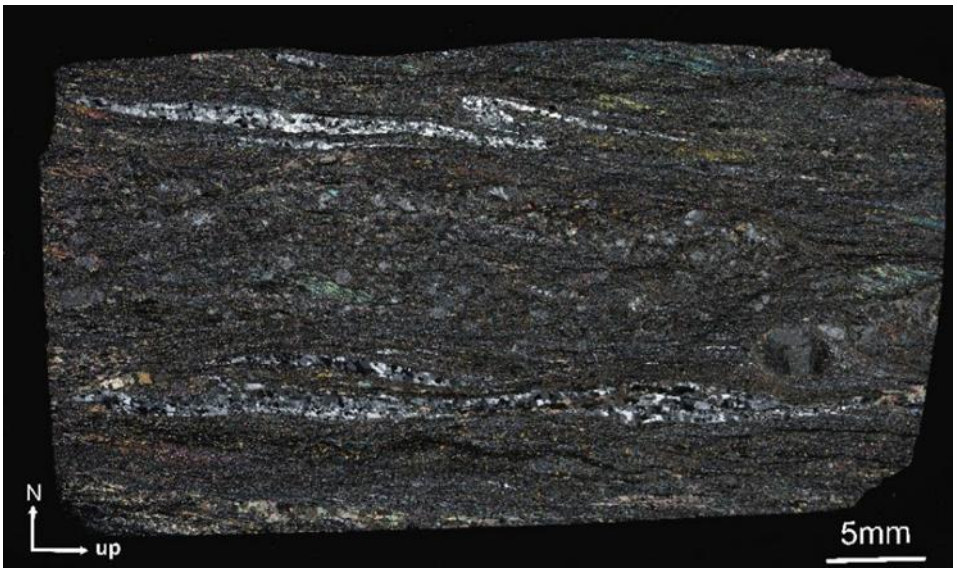

ER-22-2Z-E comprises medium-grade mylonite with abundant quartz veins and veinlets expressed as Z-folds, boudinage segments, sigmoids, and arrays. Plagioclase porphyroblasts up to 2.5 mm display strain-shadow tails oriented consistently with a dextral shear sense. The primary mineral assemblage comprises quartz, plagioclase, biotite, and hornblende, with epidote, zoisite, titanite (sphene), zircon, apatite, and opaque minerals present as accessory minerals. Alteration is marked by muscovite and chlorite, with localized chloritization concentrated along shear bands. Microstructures include quartz ribbons exhibiting undulose extinction, mica fish,

and evidence for dynamic recrystallization via grain-boundary migration; array patterns are prominent in the finer-grained quartz. North side up, south side up kinematics with dextral shear sense.

Sample: ER-22-2Z-M

Location: Zone 2 channel sample, sheared quartz veins and mylonite

Sample ER-22-2Z-M consists of medium-grained mylonite (basalt) and a sheared quartz-carbonate veinlet. The primary mineral assemblage includes quartz, plagioclase, biotite, and hornblende, with epidote, zoisite, titanite (sphene), zircon, apatite, calcite and opaque minerals present as accessories. Alteration is marked by muscovite and chlorite, with localized chloritization and sulphides concentrated along shear bands. Microstructures include quartz ribbons exhibiting undulose extinction, mica fish, and evidence for dynamic recrystallization via grain-boundary migration.

8-Zone

Sample: ER-22-8Z-B

Location: Zone 8 channel sample, sheared quartz veins and mylonite

ER-22-RB 8Z exhibits higher-temperature quartz veins that have been reworked into E-W continuous to lensiform quartz ribbons within a medium-grained mylonite that exhibits a well-developed S‑C/C’ fabric, mica fish, and feldspar porphyroclasts with sigma/delta geometries, while sheared quartz veins exhibit undulose extinction, and recrystallization is dominated by subgrain rotation with localized grain boundary migration along ribbon interiors. Barite mineralization occurs as fine veinlets and selvage that transect and locally anastomose with quartz ribbons; under reflected/transmitted light, barite is spatially associated with sulphide and gold mineralization.

Sample: ER-22-8Z-H

Location: Zone 8 channel sample, sheared quartz veins and mylonite

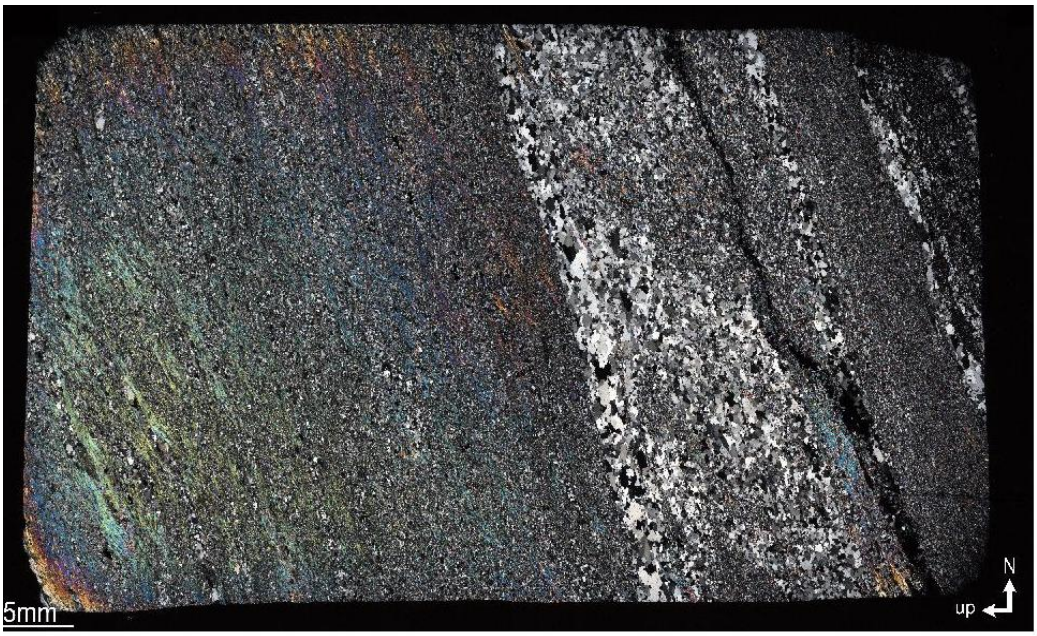

Full thin section scan of ER-RB-8Z-H, 5x, XPL

ER-22-8Z-H preserves a sharp contrast between a half-mylonitic matrix and crosscutting quartz veins, with sulphides systematically concentrated along vein‑mylonite contacts. Quartz within the veins has been dynamically recrystallized, showing grain boundary migration that produces sweeping, sutured boundaries and larger, strain-free grains toward vein interiors, while vein margins and adjacent mylonite retain mixed regimes with subordinate subgrain rotation and bulging. The mylonitic fabric is organized into S‑C/C′ domains with mica fish and quartz ribbons inherited and reworked earlier vein quartz into elongate bands, GBM-dominated quartz recrystallization in higher strain occurrence, and sulphide minerology trapped along mechanically and chemically reactive vein‑mylonite interfaces.